Award Number: DAMD17-99-1-9555

TITLE: Evaluation of Early and Prolonged Effects of Acute
Neurotoxicity and Neuroprotection Using Novel Functional
Imaging Techniques

PRINCIPAL INVESTIGATOR: Anna-Liisa Brownell, Ph.D.

CONTRACTING ORGANIZATION: Massachusetts General Hospital
Boston, Massachusetts 02114

REPORT DATE: August 2004

TYPE OF REPORT: Final

PREPARED FOR: U.S. Army Medical Research and Materiel Command
Fort Detrick, Maryland 21702-5012

DISTRIBUTION STATEMENT: Approved for Public Release;
Distribution Unlimited

20050715 102

Table of Contents

FINAL REPORT "Evaluation of Early and Prolonged Effects of Acute Neurotoxicity and Neuroprotection Using Novel Functional Imaging Techniques"

INTRODUCTION

The wide use of herbicides and pesticides has increased the risk for environmental toxicity (Reiter et al 1998, Gorrell et al 1996). In addition, airborne environmental toxicity has continuously increased (Zayed et al 1996). In addition, recent findings suggest that environmental proteasome inhibitors, like naturally occurring epoximicin, are candidates for Parkinson's disease causing toxins (McNaught, 2004). Exogenous and endogenous neurotoxicity present a major challenge in developing specific and sensitive in vivo methods to determine pathophysiological mechanisms of toxins. This information is essential in order to design new methods for neuroprotection and therapy. Our overall research goal proposed to develop and improve in vivo imaging techniques to examine neurofunction of dopaminergic and glutamatergic receptors as well as oxidative glucose metabolism and neurochemicals. High resolution imaging techniques were developed and used to explore the excitotoxicity induced regional neuronal dysfunction in functional and metabolic pathway. The neuronal toxicity models included two animal models: rats with 3-nitropropionic acid induced striatal lesions and transgenic mice with gene expression of human Huntington's disease (HD). In the final phase of this project we tested neuroprotection with novel newly developed ligands effecting on metabotropic glutamate receptor function as well as a ligand, which is a transglutaminase inhibitor.

BODY

This research project had three different components: technical tasks including hardware and software development to enable to conduct volumetric in vivo imaging in small animal models; radiopharmaceutical development of new metabotropic glutamate receptor ligands and enhance radiosynthesis of ligands to investigate dopamine receptor function; and experimental studies in rodent models of Huntington' disease to evaluate early and prolonged effects of neurotoxicity and neuroprotection. Achievements in each of these three components are evaluated in the following.

1. Technical tasks: Technical tasks were a major challenge during the first grant years. These technical tasks included the development of an imaging table for the super-high resolution positron emission tomography (PET) device, development of required software for data acquisition, implementation of image reconstruction programs to the unix (linux) based computer system and development of image analyses for multimodality data registration.

a) **Hardware development:** During the first two grant years we developed a computer controlled imaging "table" for the small super-high resolution positron emission tomograph and optimized the imaging condition for small animals, which also

effected to the general development of the high resolution PET systems for small animals (Correia et al. 2004, Appendix). The diameter of the bore in the used in-house developed PET system is 6 cm and the imaging "table" moves through it in a "step and shoot" mode. The length of the axial steps can be selected by the acquisition program of which the smallest step is 12.5 μm. The "table", which includes a stereotactic headholder with earbars and mouth (teeth) bar was designed separately for rat and mouse (Figures 1a and 1b) because the size of the head of these two species is significantly different as well as the other experimental maneuvering to prepare animals for imaging studies. For the experimental procedure the animal is secured onto the "table" through a stereotactic headholder to gas inhalation system. The "table" is then screwed into a cradle attached to the control motor in the imaging device. This design was extended during the fourth grant year to enable of imaging up to four animals simultaneously using commercial microPET system (MicroPET 4, Concord Microsystems).

b) **Software development:** Software development has been active throught the whole grant period. During the first year, software was developed to control the movement of the imaging "table" electronically to scan the whole brain slice by slice and enable volumetric data acquisition. Also image reconstruction programs were updated to run in modern high speed PC computers, both in windows and unix (linux) based system. After that the main challenge in software development has been to develop high resolution imaging techniques for multimodality registration. At first, we tested a frameless image comparison based on the joint intensity model for small animal imaging. This technique was challenging for PET receptor studies where accumulation of specific receptor ligands may occor only in a few sites and the overall anatomical information is minimal.

The other technique for multimodality image comparison, we tested, was based on edge detection. We compared extended convolution masks and active countour models. With Dr. Tuan Cao-Huu we tested three convolution mask techniques: Prewitt, Sobel and a "Truncated Pyramid" using four different sizes of computing molecules "matrix". Active contour models are based on "snake" algorithms, which represent a task of detecting high values or sudden changes in image brightness values as an energy minimization problem. However, this approach was challenging for PET imaging, where image information represents distribution of labeled ligand (high or low brightness) rather than sharply edged anatomical structures.

The technique, we finally implemented in research is based on volume rendering of MR images and fusion of MR and PET images based on the Normalized Mutual Information (NMI) voxel match algorithm of the ANALYZE software package and cubic spline interpolation (Brownell et al. 2003, Appendix).

2. Radiopharmaceutical development: During the first grant year the methods for radiosynthesis of dopamine receptor ligands were redesigned so that the specific activity was increased by ten-fold and activity concentration by fifty-fold. These improvements enabled imaging studies in small animals, like mice, where only tiny volume (50-70 μL) can be administered intravenously without changing homeostasis. However, this injected

volume should provide enough radioactivity into the target tissue to provide statistically meaningful images. The developed techniques has been utilized in all other radiosynthesis, when the product is used in small animals.

Dr. Alan Kozikowski has synthesized (Kozikowski et al 1998) and provided us the precursor for labeling of metabotropic glutamate receptor agonist; (methyl-2-(methoxycarbonyl)-2-(methylamino) bicycle[2.1.1] -hexane-5- carbocylate (MMMHC). During the second year we successfully radiolabeled the amine precursor with C-11 methyl triflate and a yield of 120 mCi of the labeled product was obtained (Figure 2, Appendix). This labeled ligand goes through the blood brain barrier (Figures 4 and 7a) and we hypothesize that it will be metabolized to (2-aminobicyclo [2.1.1]hexane-2,5-dicarboxylic acid-I (ABHxD-I) in the brain tissue through esterase and aminase (Yu et al. 2003, Appendix). Dr. Kozikowski and his team have shown that ABHx-D-I binds on group I and II metabotropic glutamate receptors. Reported EC50 values are mGluR2 (0.33uM) > mGluR5 (0.72 uM) > mGluR1 (1.6 uM) > mGluR3 (2.2 uM) > mGluR6 (5.3) > mGluR4 (23 uM) (Kozikowski et al 1998, Conti et al 2000). It should be emphasized that according to the published reports our studies are the first in vivo imaging studies in the world to visualize metabotropic glutamate subtype 2/3 receptor function (Yu et al. 2003, Appendix). We have presented these data in several meetings and been also invited to the Drug Development Meeting.

Dr. Kozikowski's team is further developing different precursor ligands for metabotropic glutamate receptors and has provided us three different precursors for metabotropic glutamate subtype 5 receptors. During the 4th grant year we radiolabeled them with carbon-11 and tested in rats (Figures 5 and 6, Appendix; Abstracts,Yu et al. 2003 and Yu et al. 2004, Appendix). These new receptor ligands will open new views to explore mechanism of neural circuitry of dopaminergic function including the role of the olfactory bulb especially in Parkinson's disease (Yu et al. 2004, Appendix).

3. Biological experiments: Experimental biological studies were conducted in 3-nitropropionic acid induced neurotoxicity rat model and transgenic mouse model of Huntington's disease. These experiments can be divided into four different categories; a) studies of neurotoxicity induced acute and prolonged effects in rats; b) studies of extented CAG-repeat length induced neurochemical changes in mice; c) neuroprotection against 3-NP induced neurotoxicity in rats and d) neuroprotection in transgenic mice. Achievements in each category is summarized in the following.

a) **Studies of 3-NP induced acute and prolonged effects in rats:** During the first two grant years we investigated 3-NP induced acute and prolonged effects in glucose metabolism, dopamine and glutamate receptor function and neurochemical changes. 3-NP, a suicide inhibitor of succinate dehydrogenese (Johnson et al 2000) creates mitochondrial inhibition and causes striatal degeneration (Storgaard et al 2000, Guyot et al 1997, Bowyer et al 1996). Experiments and results of PET studies of glucose metabolism and MRS studies of neurochemicals are published in the Journal of Neurochemistry (Brownell et al. 2004, Appendix). In addition, changes in dopaminergic function are published in the New York Academy of Science (Brownell et al. 2003, Appendix). As a summary it can be concluded that we

observed extensive inter animal variation as a response to 3-NP toxicity. The animals, which developed large striatal lesions had decreased glucose utilization in the striatum and cortex one day after starting daily 3-NP injections. Similarly succinate and lactate/macromolecule levels were enhanced; these changes being however, reversible. Progressive degneration was observed by decreasing striatal glucose utilization and N-acetylaspartate and increasing choline. In studies of dopamine receptor function we found progressively decreasing dopamine D1 and D2 receptor function and temporal variation in dopamine transporter binding (Figure 3, Appendix). These observations, obtained by in vivo imaging studies, paralleled with weight loss and in behavioral deficit. Animals that did not develop lesions showed reversible enhancement in cortical glucose utilization and no change in striatal glucose utilization or locomotor activity. Recent study by Guo et al (Guo et al 2000) shows that dietary restrictions can exhibit the effect of 3-NP neurotoxicity. However, a low glucose level alone, which could exhibit 3-NP neurotoxicity, is not enough to explain the interanimal variation observed in these studies.

b) **Experiments of metabolic and neurochemical changes in transgenic mice:** We conducted longitudinal imaging studies of glucose metabolism, dopamine D1 and D2 receptors and dopamine transporters in Huntington's disease mouse model and littermate controls. Technical arrangement of experimental imaging procedures with a super-high resolution PET system is presented Figure 1b (Appendix). The slice thickness was 1.5 mm and studies were performed with 1.25 mm steps.

For MRS, the imaging voxels were placed symmetrically over both basal ganglia (average size of 6x3.5x3mm, 63uL) or over the motor cortex (6x2x3 mm, 36uL). Spectra were integrated and normalized to the creatine/phosphocreatine peak. Longitudinal analyses of glucose utilization in HD mice showed in striatum a progressive decrease of 0.05%/day. The decrease in the striatal NAA (0.56%/day) was one order higher than the glucose utilization. In the same time period, Cho was increased 34 % compared to the littermate control. These observations parallel the developing of HD symptoms. Interestingly, no significant changes were observed in cortical metabolism. These results have been presented in the Society of Nuclear medicine Meeting (Brownell et al. 2002 abstract and in the Meeting on High Resolution Imaging in Small Animals (Brownell et al. 2001, abstract).

c) **Neuroprotection against 3-NP induced neurotoxicity in rats:** We investigated characteristics of metabotropic glutamate receptor agonist; ABHxD-I as a neuroprotective agent. These experiments showed less decrease in glucose utilization and glutamate receptor binding after 3-NP neurotoxicity than in non-protected animals. However, dopamine receptor binding decreased in all protected animals more than in non-protected animals.

Since glucose utilization is a major energy source of the brain, the change in glucose utilization can be a sensitive indicator for the energy dysfunction in the brain. 3-NP, a permanent inhibitor of succinate dehydrogenese (Johnson et al 2000) can disrupt the mitochondrial function, decrease glucose utilization and cause striatal degeneration (Storgaard et al 2000, Guyot et al 1997, Bowyer et al 1996).

Interestingly, Reynolds et al (Reynolds et al 1998) published that dopamine deficiency may protect against 3-NP toxicity and Johnson et al (Johnson et al 2000) published that long term exposure to 3-NP increases dopamine turnover.

In our experiments, neuroprotection with ABHxD-I originated dopamine receptor deficiency and enhance glucose utilization (Figures 7a and 7b, Appendix).

In addition, we investigated neuroprotection by using cystamine, which is transglutaminase inhibitor. Cystamine was administered (9mg/kg ip.) one hour before a single dose of 3-NP (25 mg/kg iv.). Glucose utilization evaluated by PET imaging 2 hours after 3-NP administration showed 18% decrease in the cortex, 23% decrease in the striatum and cerebellum in cystamine treated animals compared to 3-NP only treted animals. The observation of decreased glucose utilization with cystamine treatment is an indication of enhanced neurotoxicity of 3-NP when combined with cystamine. These results paralleled with behavioral observations as reported in the annual report in 2003.

d) Neuroprotection in transgenic mice: We used 7-hydroxyiminocyclo propan [b]chromen-1a-carboxylic acid ethyl ester, (CPCCOEt), an antagonist for metabotropic glutamate subgroup 1 receptors and cystamine, which is a transglutaminase inhibitor to investigate neuroprotection in transgenic mouse model of HD. We conducted longitudinal imaging studies of glucose utilization and dopamine D2 receptors in transgenic mice treated with neuroprotective drug and in untreated transgenic mice as controls to investigate the efficacy of neuroprotection. Studies conducted with cystamine are presented in the manuscript Wang et al (submitted to the Journal of Neuroscience, Appendix) and in the abstract presented in the Society of Nuclear Medicine Meeting in June 2004, which was selected the finalist in the Young Investigators' Competition. As a summary, using cystamine we observed dose dependent neuroprotection based on glucose utilization, dopamine D2 receptor binding and development of inclusions. CPCCOEt provided also neuroprotection based on glucose utilization comparable to the level obtained with cystamine dose of 9 mg/kg.

Table 1. Rate of percent decrease of glucose utilization after the age of 70 days investigated by ^{18}F-FDG PET studies. The number of animals in each group was 6.

Treatment	Percent decrease of glucose utilization per day		
	Cortex	Striatum	Cerebellum
Untreated mice	3.873	3.186	3.090
Cystamine 50mg/kg	1.986	1.841	1.739
Cystamine 100mg/kg	1.224	2.385	1.899

Decrease of glucose utilization in the brain of untreated mice has an exponential form starting from the age of 58 days. This might be an indication of fast changes in glucose utilization when the HD-related changes start to progress in the

mouse brain. After the age of 70 days changes were stabilized and degenerative process was linear.

Table 2. ^{11}C-raclopride binding in the striatum of the transgenic mouse model of HD at the age of 74 days. The mice were treated with 4 different doses of cystamine. The number of the studies in each group was 4.

Treatment	Binding potential
Untreated	1.072+/-0.029
Cystamine 5.4 mg/kg	1.064+/-0.071
Cystamine 9 mg/kg	1.076+/-0.065
Cystamine 50 mg/kg	1.218+/-0.058
Cystamine 100mg/kg	1.258+/-0.076

KEY RESEARCH ACCOMPLISHMENT

- design and construction of imaging "tables" with stereotactic headholders for rat and mouse

- development of software for data acquisition and reconstruction for modern PC and linux based systems

- development and testing image algorithms for image reconstruction for multi modality image registration

- observation of significant interanimal variation in the response for 3-NP induced neurotoxicity in motor activity and energy metabolism

- observation of significant weight loss during 3-NP administration in all animals independently of response to motor activity or energy metabolism

- observation that cortical glucose metabolism may be enhanced to compensate striatal deficit

- observation that striatal lesion in glucose (energy) metabolism can be introduced immediately after first administration of 3-NP

- observation that striatal lesions demonstrating energy deficit show progressive decrease in dopamine D1 and D_2 receptor

- observation that dopamine transporter binding is slightly increased immediately post 3-NP and progressively decreases later

- observation that metabotropic glutamate receptor binding is decreased after 3-NP focally in striatal area similarly as glucose utilization

- observation that MRS shows increased peaks of succinate and lactate and macromolecules in early 3-NP toxication and these are reversible changes

- observation that decreasing of glucose utilization as well as NAA is linearly correlated with age in the striatum of HD mice

- observation that after MPTP treatment, the same metabotropic glutamate receptor ligand had also affinity to mGluR1 and mGluR5 receptors and had locally decreased binding in striatal and cortical area which also showed decreased blood flow and significantly decreased striatal dopamine transporter binding

  observation that MRS shows increased succinate immediately after 3-NP and can be used in real time to follow development of lesion and effect of neuroprotection

  observation that ABHxD-I developes neuroprotection by enhancing glucose utilization and dopamine receptor degeneration

- development of stack system to image up to 4 animals simultaneously and further enhance of the stereotactic headholders for mouse and rat studies

- development of data acquisition and reconstruction for stack imaging with a newly installed microPET system

- conclusion of enhanced neurotoxicity in a 3-NP rat model of HD pretreated with cystamine (dose 9 mg/kg ip.) based on observations of decreased glucose utilization in different brain areas, increased deficit in motor score, increased mortality and histological verification of neural damage

- observation that decrease of glucose utilization (energy metabolism) has exponential correlation with age in early ages and correlates with development of HD like degeneration in a transgenic mouse model of HD

- observation that partial neuroprotection can be provided by cystamine in transgenic mouse model of HD even with a low dose of 5.4 mg/kg ip. based on studies of glucose (energy) metabolism by PET, MRS studies of neurochemicals and endpoint histological verification

- observation that neuroprotection in dopaminergic system of transgenic mouse can be obtained with cystamine, doses higher than 50 mg/kg based on studies of ^{11}C-raclopride of dopamine D2 receptors

REPORTABLE OUTCOME

Publications:

Wang Xukui, Sarkar Aparajita, Cicchetti Francesca, Yu Meixiang, Zhu Aijun, Jokivarsi Kimmo, Saint-Pierre Martine, Lapointe Nicolas, Brownell Anna-Liisa. Cerebral PET imaging and histological evidence of transglutaminase inhibitor cytamine induced neuroprotection in transgenic R6/2 moue model of Huntington' dieae. Journal of Neuroscience (submitted)

Brownell Anna-Liisa, Chen Y.Iris, Yu Meixiang, Wang Xukui, Dedeoglu Alpashan, Cicchetti Francesca, Jenkins BruceG., Beal M.Flint. 3-Nitropropionic acid induced neurotoxicity – assessed by ultra high resolution PET with comparison to MRS. Journal of Neurochemistry 89:1206-1214, 2004.

Correia John A., Burnham Charles A., Kaufman David, Brownell Anna-Liisa, Fischman Alan J. Performance evaluation of MMP-II: a second-generation small animal PET. IEEE Transactions on Nuclear Science 51: 21-26, 2004.

Brownell Anna-Liisa, Canales Kelly, Chen Y.Iris, Jenkins Bruce G., Owen Christopher, Livni Eli, Yu Meixiang, Cicchetti Francesca, Sanchez- Pernaute Roario, Isacson Ole. Mapping of brain function after MPTP induced neurotoxicity in a primate Parkinson's disease model. NeuroImage 20: 1064-75, 2003.

Yu Meixiang, Nagren Kjell, Chen Y.Iris, Livni Eli, Elmaleh David, Kozikowski Alan, Brownell Anna-Liisa. Radiolabeling and biodistribution of methyl 2-(methoxycarbonyl) -2- (methylamino)bicyclo[2.1.1] –hexane-5-carboxylate, a potential neuroprotective drug. Life Science 73:1577-1585, 2003.

Brownell Anna-Liisa, Chen Y.Iris, Wang Xukui, Yu Meixiang, Jenkins Bruce G. Neurotoxicity-induced changes in striatal dopamine receptor function. Ann. N.Y. Acad. Sci 991:281-283, 2003.

Abstract and Presentations:

Yu Meixiang, Zhu Aijun, Wang Xukui, Jokivarsi Kimmo, Brownell Anna-Liisa. Imaging of the dopamine system in olfactory bulb by positron emission tomography (PET) in rats. Society Nuclear Medicine. 51st Annual Meeting. June 2004.

Yu Meixiang, Wang Xukui, Jokivarsi Kimmo, Kozikowski Alan, Brownell Anna-Liisa. Synthesis and evaluation of [11C]M-MPEP and [11C]M-PEPy, potent and selective radioligands for metabotropic glutamate subtype 5 (mGlu5) receptor by positron emission tomography (PET). Society Nuclear Medicine. 51st Annual Meeting. June 2004.

Wang Xukui, Sarkar Aparajita, Yu Meixiang, Cicchetti Francesca, Jokivarsi Kimmo, Brownell Anna-Liisa. Cystamine induced neuroprotection in transgenic R6/2 mouse model of Huntington's disease – assessed by positron emission tomography (PET) studies. Society Nuclear Medicine. 51st Annual Meeting. June 2004. (Finalist in the Young Investigators' Competition)

Yu Meixiang, Wang Xukui, Zhu Aijun, Brownell Anna-Liisa. Synthesis and evaluation of C-11 MPEP, potent and selective radioligand for metabotropic glutamate subtype 5 (mGlu5) receptor by positron emission tomography (PET). Society for Molecular Imaging. Annual Meeting. September 2004.

Yu Meixiang, Klaess Thomas, Kozikowski Alan, Brownell Anna-Liisa. Synthesis of [11C]methoxymethyl-MTEP and [11C]methoxy-PEPy, potent and selective PET radioligand for metabotropic glutamate subtype 5 (mGlu5) receptor. Society of Neuroscience. Annual Meeting. October 2003.

A-L Brownell, YI Chen, KE Canales, E. Livni, RT Powers, A Dedeoglu, FM Beal, BG Jenkins. 3-NP induced neurotoxicity – assessed by ultra high resolution PET with comparison to MRI and MRS. 1st Annual Meeting of the Society for Molecular Imaging. Boston, August 24-26, 2002

K. Canales, A-L. Brownell. New approaches in parametric imaging -use of direct algorithm. 49th Annual Meeting of the Society of Nuclear Medicine. Los Angeles, June 15-19, 2002. The Journal of Nuclear Medicine 2002; 45:(S5):209.

A-L. Brownell, Y.I. Chen, K. Canales, B. Powers, B.G. Jenkins. Neural degeneration in a transgenic HD mouse model - an ultra high resolution PET study with comparison to MRI/MRS. 49th Annual Meeting of the Society of Nuclear Medicine. Los Angeles, June 15-19, 2002. The Journal of Nuclear Medicine 2002;45:(S5):61.

A-L. Brownell, K. Canales, Y.I. Chen, C. Owen, R. Powers, A. Kozikowski, D. Elmaleh, M. Yu. Metabotropic glutamate receptors - new targets for neuroimaging. 49th Annual Meeting of the Society of Nuclear Medicine. Los Angeles, June 15-19, 2002. The Journal of Nuclear Medicine 2002;45:(S5):110.

M.Yu, E. Livni, K. Nagren, K. Canales, R.Powers, D. Elmaleh, A. Kozikowski, A-L. Brownell.11C-labeling of methyl 2-(methoxycarbonyl)-2-(methylamino) bicycle (2.1.1)hexane-5-carboxylate, a potent neuroprotective drug. 49th Annual Meeting of the Society of Nuclear Medicine. Los Angeles, June 15-19, 2002. The Journal of Nuclear Medicine 2002;45:(S5):167.

Correia John A., Burnham Charles A., Kaufman David, Brownell Anna-Liisa, Fischman Alan J. Performance evaluation of a second-generation small animal PET. Nuclear Science Symposium Conference Record, 2002 IEEE, vol 2, pp 802-806.

Anna-Liisa Brownell, Y. Iris Chen, Kelly Canales, Robert Powers, Ole Andreasson, Flint Beal, Bruce Jenkins. Glucose utilization assessed by high resolution PET with comparison to MRI/MRS in a transgenic mouse model of Huntington's disease. HiRes2001, Meeting on High Resolution Imaging in Small Animals: Instrumentation, Applications and Animal Handling, September 9-11, 2001, Rockville, Maryland.

A-L Brownell, YI Chen, KE Canales, RT Powers, A Dedeoglu, FM Beal, BG Jenkins. 3-NP induced neurotoxicity – assessed by ultra high resolution PET with comparison to MRI and MRS. 31st Annual Meeting of Neuroscience. San Diego, November 10-15, 2001.

A-L. Brownell, Y.I. Chen, K.E. Canales, R.T. Powers, A.Dedeoglu, B.G. Jenkins. Coupling of glucose utilization to neuronal toxicity – an ultra high resolution PET study. The Annual Meeting of Society Nuclear Medicine. Toronto, Canada, June 25-29, 2001. Journal of Nuclear Medicine 42:5s, 2001

Cao-Huu T, Lachiver G, Brownell A-L "High Resolution Imaging and Multi-Modal Registration with Joint Intensities" Presentation at IEEE Medical Imaging Conference. October 15-20, 2000

Personnel supported by the grant DAMD17-99-1-9555 during 7/15/99-7/14/04

CONCLUSIONS

Challenging technical tasks have been resolved and developed for successful imaging techniques in small animal models during the first two grant years including designing and constructing computer controlled imaging "table" and other accessories needed to accomplish the whole project. Algorithm development for data acquisition, image reconstruction and data analyses have been very successful and automated programs are now running both in windows and linux based systems. This enables fast data analyses for the experimental measurements.

Significant amount of biological information has been obtained regarding the 3-NP induced degenerative processes in energy metabolism as well as dopaminergic regulation during degeneration. We observed increase in dopamine transporter binding to presynaptic terminals immediately after 3-NP intoxication. This phenomen as well as early increases of lactate and succinate in MRS were reversible. Metabotropic glutamate receptors provide a new interesting insight to investigate the degenerative processes and their neuroprotective characteristics will be investigated by the big drug companies world

wide in the coming years. We also investigated characteristics of transglutaminase inhibitor, cystamine as a neuroprotective agent in transgenic mouse model of HD and found dose dependent neuroprotection based on glucose utilization, dopamine D2 receptor function and development of inclusions.

REFERENCES

Bowyer JF, Clausing P, Schmued L, Davies DL, Binienda Z, Newport GD, Scallet AC, Slikker W Jr. Parenterally administered 3-nitropropionic acid and amphetamine can combine to produce damage to terminals and cell bodies in the striatum. Brain Res 1996; 712(2):221-9.

Conti P, Kozikowski AP. New synthesis of 2-aminobicyclo[2.1.1]hexane-2,5-dicarboxylic acid-I (ABHxD-I), a potent metabotropic receptor agonist. Tetrahedron Letters 0 (2000) 1-4.

Gorrell JM, DiMonte D, Graham D. The role of the environment in Parkinson's disease. Environmental Health Perspective1996; 104: 652-4.

Guo Z, Ersoz A, Butterfield DA, Mattson MP. Beneficial effects of dietary restriction on cerebral cortical synaptic terminals: preservation of glucose and glutamate transport and mitochondrial function after exposure to amyloid beta-peptide, iron, and 3-nitropropionic acid. J Neurochem 2000: 75(1):314-20.

Guyot MC, Hantraye P, Dolan R, Palfi S, Maziere M, Brouillet E. Quantifiable bradykinesia, gait abnormalities and Huntington's disease-like striatal lesions in rats chronically treated with 3-nitropropionic acid. Neuroscience 1997; 79(1):45-56.

Johnson JR, Robinson BL, Ali SF, Binienda Z. Dopamine toxicity following long term exposure to low doses of 3-nitropropionic avid (3-NPA) in rats. Toxicol Lett 2000; 116(1-2):113-8.

Kozikowski AP, Steensma D, Araldi GL, Tuckmantel W, Wang S, Pshenichkin S, Surina E, Wroblewski JT. Synthesis and biology of the conformationally restricted ACPD analogue, 2-aminobicyclo[2.1.1]hexane-2,5-dicarboxylic acid-I, a potent mGluR agonist. J Med Chem 1998; 41,1641-1650.

McNaught KSP, Perl Dsaniel P, Brownell Anna-Liisa, Olanow C Warren. Systemic exposure to proteasome inhibitors causes a progressive model of Parkinson's disease. Ann Neurol 2004; 56:149-162.

Reiter LM, DeRosa C, Kavlock RJ, Lucier G, Mac MJ, Melillo J, Melnick RL, Sinks T, Walton BT, The U.S. Federal framework for research on endocrine disruptors and an

analysis of research programs supported during fiscal year 1996. Environmental Health Prespect 1998; 106: 105-113.

Reynolds DS, Carter RJ, Mortion AJ. Dopamine modulates the susceptibility of striatal neurons to 3-nitropropionic acid in the rat model of Huntington's disease. J neurosci 1998; 18(23)1011-27.

Storgaard J, Kornblit BT, Zimmer J, Bert J, Gramsbergen P. 3-Nitropropionic acid in organotypic striatal and corticostriatal slice cultures is dependent on glucose and glutamate. Exp Neurol 2000; 164(1):227-35.

Zayed J, Mikhail M, Loranger S, Kennedy G, L'Esperance G. Exposure of taxi drivers and office workers to total and respirable manganese in an urban environment. American Industrial Hygiene Association Journal 1996; 57: 376-80.

APPENDICES

Figures 1-7.

Wang Xukui, Sarkar Aparajita, Cicchetti Francesca, Yu Meixiang, Zhu Aijun, Jokivarsi Kimmo, Saint-Pierre Martine, Lapointe Nicolas, Brownell Anna-Liisa. Cerebral PET imaging and histological evidence of transglutaminase inhibitor cytamine induced neuroprotection in transgenic R6/2 moue model of Huntington' dieae. Journal of Neuroscience (submitted)

Brownell Anna-Liisa, Chen Y.Iris, Yu Meixiang, Wang Xukui, Dedeoglu Alpashan, Cicchetti Francesca, Jenkins BruceG., Beal M.Flint. 3-Nitropropionic acid induced neurotoxicity – assessed by ultra high resolution PET with comparison to MRS. Journal of Neurochemistry 89:1206-1214, 2004.

Correia John A., Burnham Charles A., Kaufman David, Brownell Anna-Liisa, Fischman Alan J. Performance evaluation of MMP-II: a second-generation small animal PET. IEEE Transactions on Nuclear Science 51: 21-26, 2004.

Brownell Anna-Liisa, Canales Kelly, Chen Y.Iris, Jenkins Bruce G., Owen Christopher, Livni Eli, Yu Meixiang, Cicchetti Francesca, Sanchez- Pernaute Roario, Isacson Ole. Mapping of brain function after MPTP induced neurotoxicity in a primate Parkinson's disease model. NeuroImage 20: 1064-75, 2003.

Yu Meixiang, Nagren Kjell, Chen Y. Iris, Livni, Elijahu, Elmaleh David, Kozikowski Alan, Wang Xukui, Jokivarsi Kimmo, Brownell Anna-Liisa. Radiolabeling and biodistribution of methyl 2-(methoxycarbonyl)-2-(methylamino) bicyclo [2.1.1] – hexane -5-carboxylate, a potential neuroprotective drug. Life Science 73:1577-1585, 2003.

Brownell Anna-Liisa, Chen Y.Iris, Wang Xukui, Yu Meixiang, Jenkins Bruce G. Neurotoxicity-induced changes in striatal dopamine receptor function. Ann. N.Y. Acad. Sci 991:281-283, 2003.

Yu Meixiang, Klaess Thomas, Kozikowski Alan, Brownell Anna-Liisa. Synthesis of [11C]methoxymethyl-MTEP and [11C]methoxy-PEPy, potent and selective PET radioligand for metabotropic glutamate subtype 5 (mGlu5) receptor. Society of Neuroscience. Annual Meeting. October 2003.

Yu Meixiang, Zhu Aijun, Wang Xukui, Jokivarsi Kimmo, Brownell Anna-Liisa. Imaging of the dopamine system in olfactory bulb by positron emission tomography (PET) in rats. Society Nuclear Medicine. 51st Annual Meeting. June 2004.

Yu Meixiang, Wang Xukui, Jokivarsi Kimmo, Kozikowski Alan, Brownell Anna-Liisa. Synthesis and evaluation of [11C]M-MPEP and [11C]M-PEPy, potent and selective radioligands for metabotropic glutamate subtype 5 (mGlu5) receptor by positron emission tomography (PET). Society Nuclear Medicine. 51st Annual Meeting. June 2004.

Wang Xukui, Sarkar Aparajita, Yu Meixiang, Cicchetti Francesca, Jokivarsi Kimmo, Brownell Anna-Liisa. Cystamine induced neuroprotection in transgenic R6/2 mouse model of Huntington's disease – assessed by positron emission tomography (PET) studies. Society Nuclear Medicine. 51st Annual Meeting. June 2004. (Finalist in the Young Investigators' Competition)

Yu Meixiang, Wang Xukui, Zhu Aijun, Brownell Anna-Liisa. Synthesis and evaluation of C-11 MPEP, potent and selective radioligand for metabotropic glutamate subtype 5 (mGlu5) receptor by positron emission tomography (PET). Society for Molecular Imaging. Annual Meeting. September 2004.

PI. Anna-Liisa Brownell: "Evaluation of Early and Prolonged Effects of Acute Neurotoxicity Using Novel Functional Imaging Techniques"

Rat and mouse frames used for PET studies
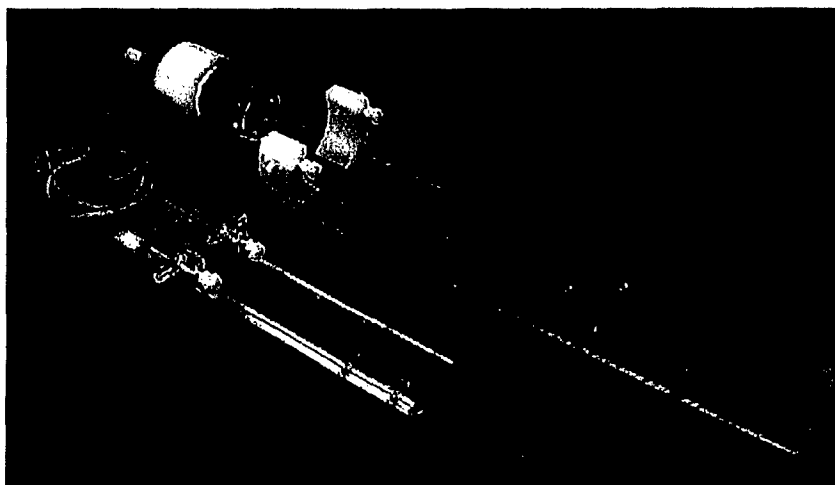
Rat experiment in a super high resolution PET camera
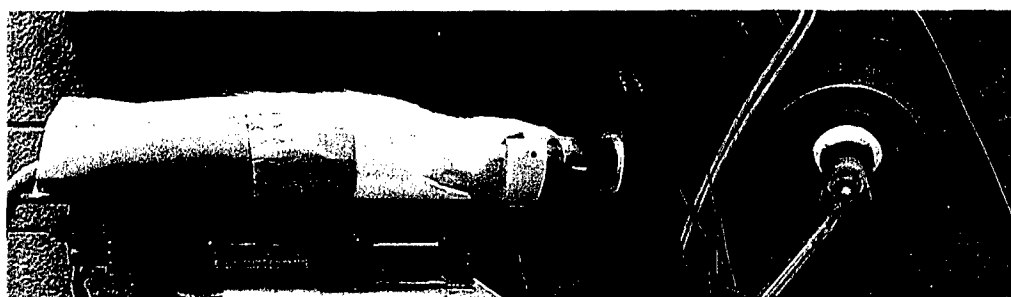
Side View   **Front View**

Figure 1. Stereotactic headholders for mouse and rat and experimental arrangement for PET imaging.

Figure 1a. Stereotactic headholder for mouse and rat (above) and experimental arrangement for PET imaging (below).

Mouse experiment in a super high resolution PET camera

Side view

Front view
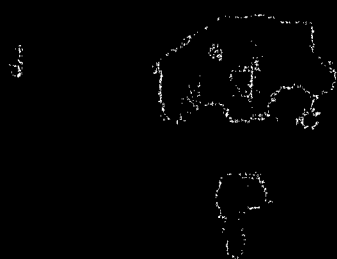
Scale
10 mm

**Coronal slice
of midbrain**

**Coronal slice
of heart**

18F-FDG washout curve from the left ventricle cavity

$Y = 63.1 * exp(-0.267t) + 35.5 * exp(-0.063t) + 59.9$
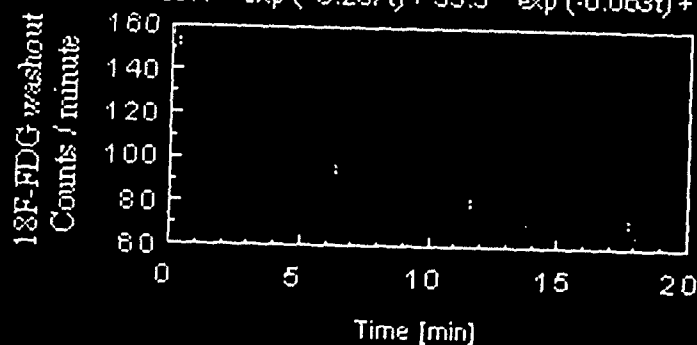
Figure 1b. (top) Mouse experiment in a house-built super high resolution PET scanner.
(middle) Coronal slices of midbrain and heart illustrate regional glucose utilization.
(below) Washout curve of radioactivity (^{18}F-FDG) from the left ventricle detected by in
vivo imaging over heart.

Design New Drug-- MMMHC

methyl-2-(methoxycarbonyl)-2-(methylamino) bicycle [2.1.1]-hexane-5-carboxylate
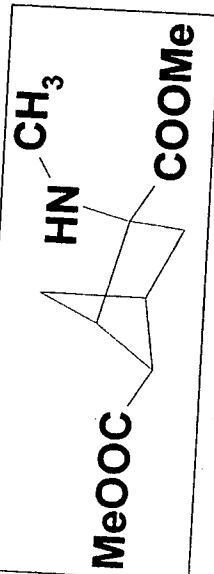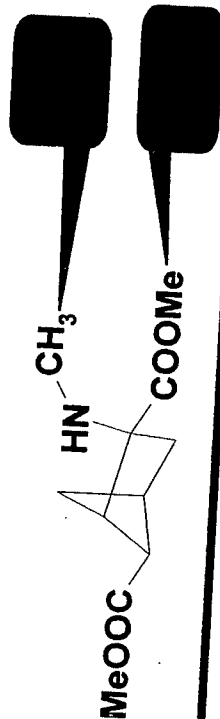

MMMHC

In the brain

1. Esterase   2. Aminase
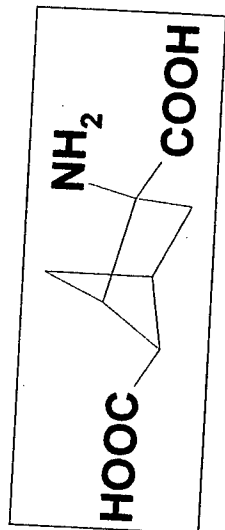
ABHxD-I

Labeling strategies

C-11 Labeling MMMHC

11C-Methyl Triflate

Acetone, 60°C 3min.

Figure 2. Schematic diagram of the radiolabeling of precursor for ABHxD-I with methyl iodide technique and carbon-11. (top) Expected metabolic pathway of the precursor ligand in the brain. (middle) Possible labeling sites for carbon-11. We used HN-CH3 link. (bottom) Radiochemical procedure to introduce carbon-11 to the precursor molecule.
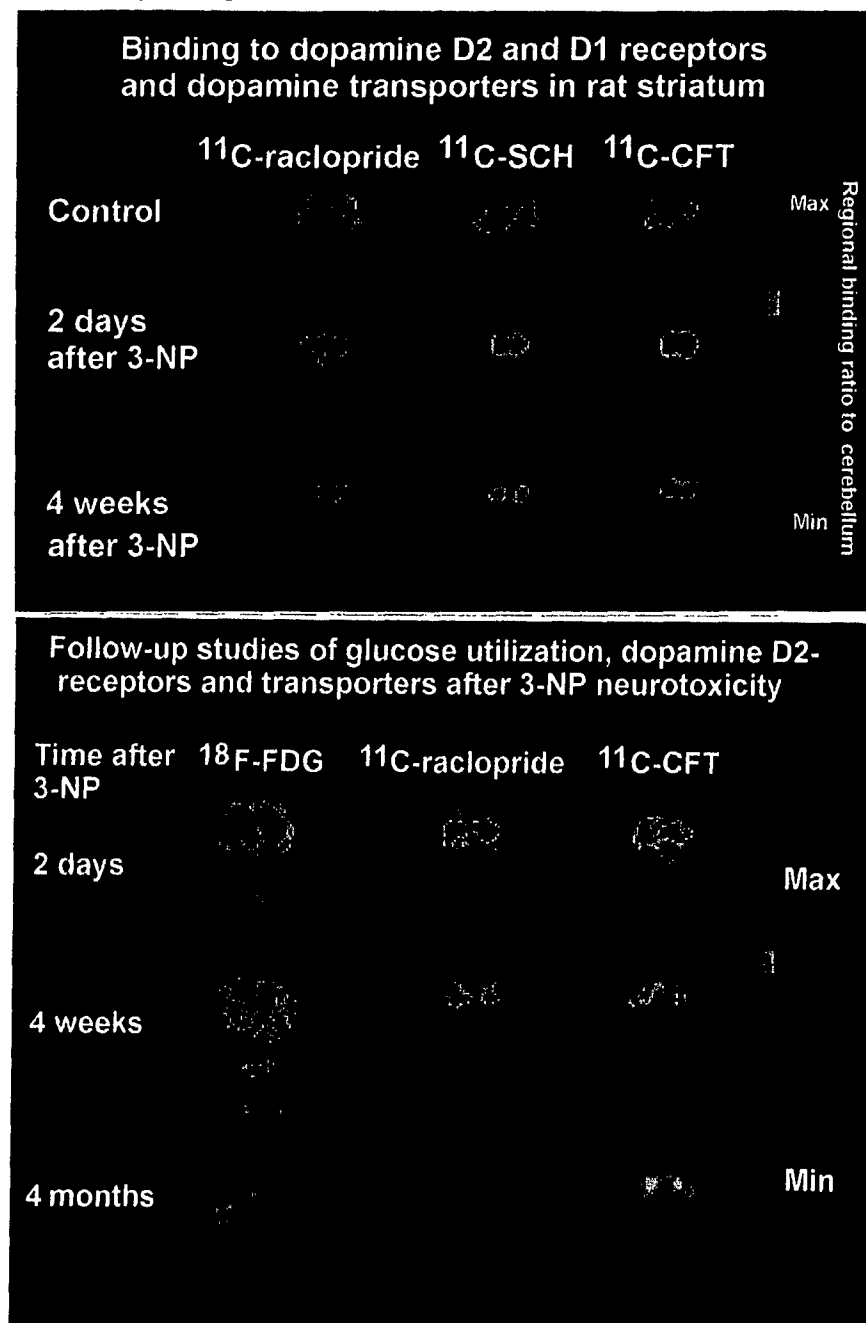
Figure 3. Longitudinal PET studies of glucose utilization (18F-FDG), dopamine D2 receptors (^{11}C-raclopride), dopamine D1 receptors (^{11}C-SCH) and dopamine transporters (^{11}C-CFT) pre and post 3-NP. Note the local decrease of glucose utilization in striatum in 2 days after 3-NP and late recovery. Dopamine D1 and D2 receptors show gradual decrease in binding while dopamine transporter shows first enhanced binding and later decrease.
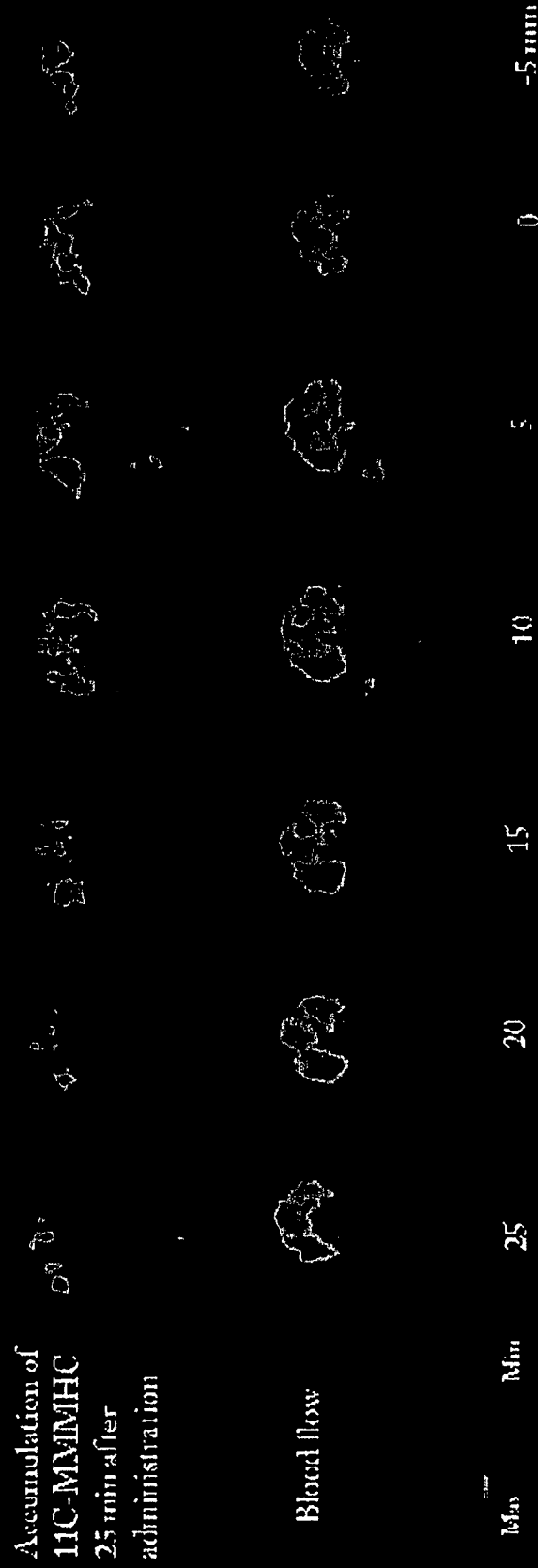
Figure 4. (top) Distribution of C-11 labeled mGluR receptor ligand (11C-MMMHC) 25 min after administration in the normal monkey (Macaca fascicularis) brain. (bottom) Blood flow study in the same animal. These images show that 11C-MMMHC binds dominantly in cortical areas.

11C-M-PEPy accumulation in rat brain

Olfactory bulb and
Harderian gland

Control study

Striatum

Thalamus

After blocking with
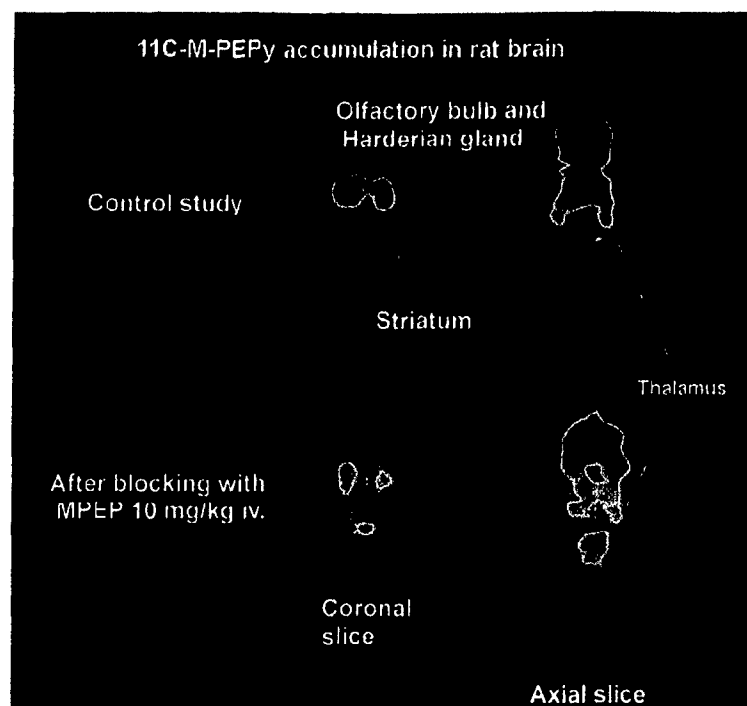MPEP 10 mg/kg iv.

Coronal
slice

Axial slice

Figure 5. [^{11}C]M-PEPy accumulation in rat brain 8 min after injection of the
radiolabeled ligand at the mid-striatal level. Control study (above) and
replacement study 3 min after administration of "cold" MPEP (dose 10
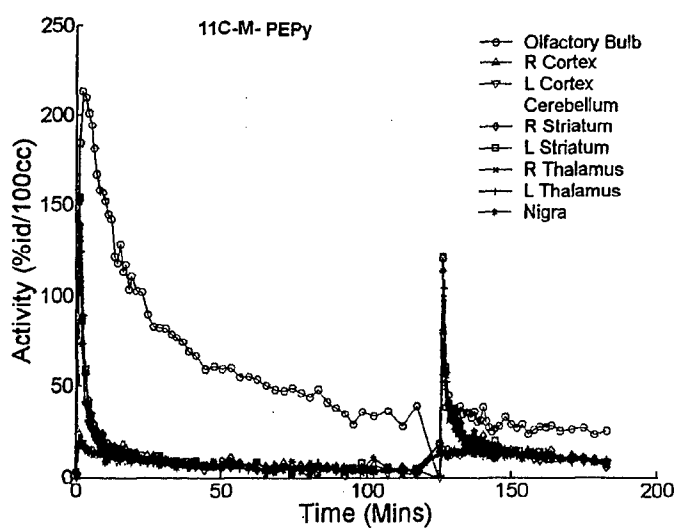mg/kg iv) (below).

Figure 6. Time-activity curves of the above experiment demonstrate selective
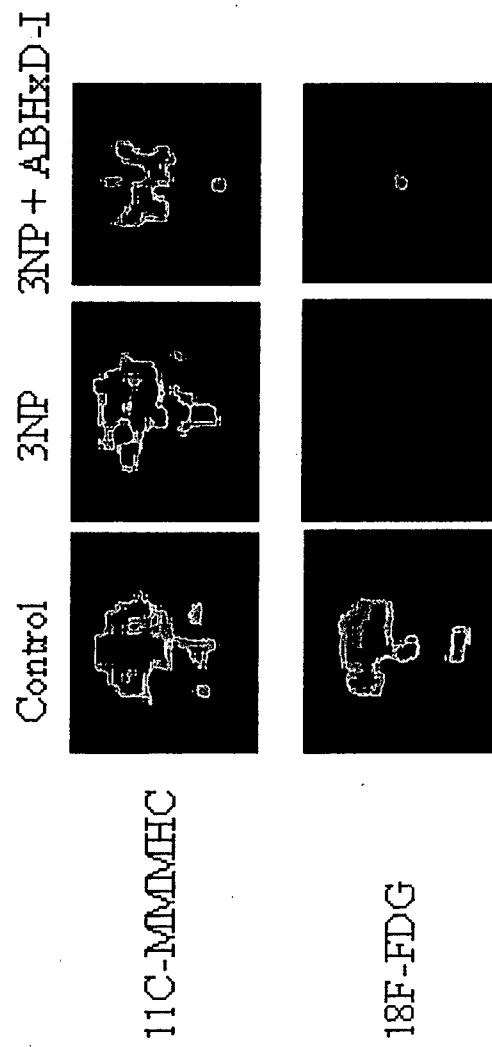blocking with cold MPEP in several brain areas.

Figure 7a. Study of glucose utilization and binding of 11C-MMMHC in a control rat, a rat treated with 3-NP only (a high single dose) and a rat having neuroprotection with ABHxD-I 30 min before 3-NP injection (a high single dose). Imaging studies were done 2 days after 3-NP administration. These images clearly show enhanced glucose utilization in a rat protected with ABHxD-I compared to 3-NP only injected rat.
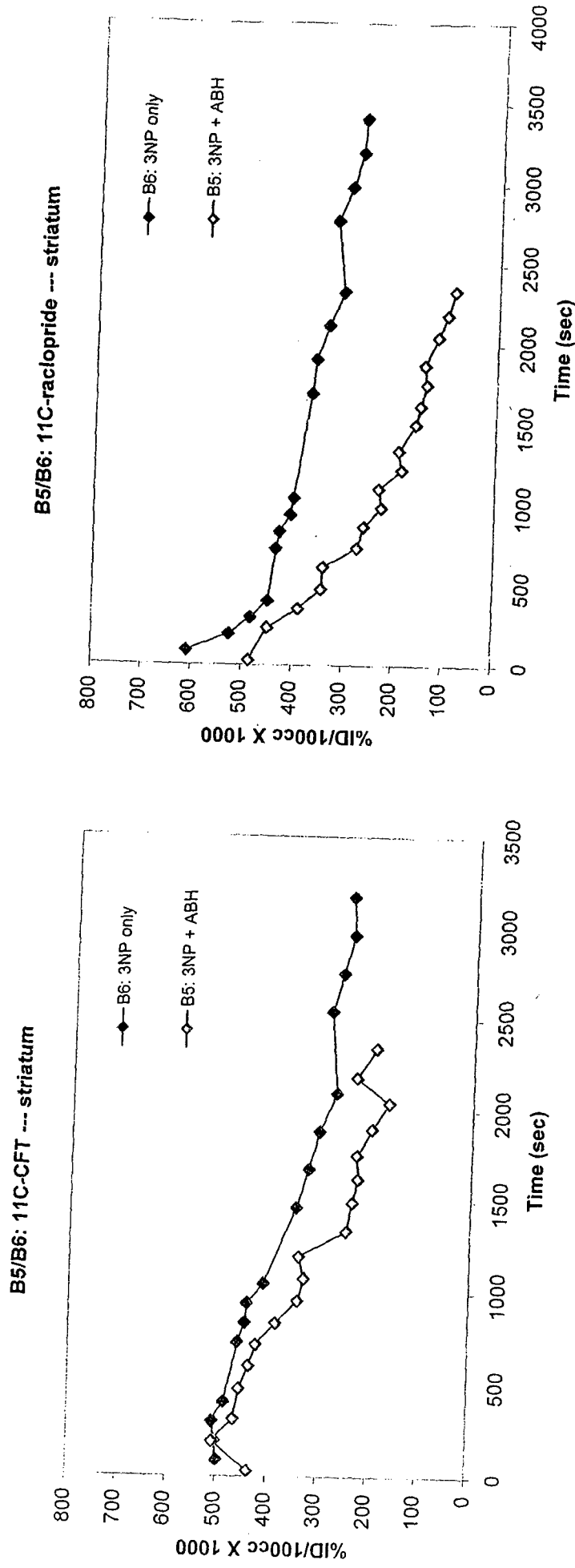
Figure 7b. Binding curves of 11C-CFT (binding in dopamine transporters) and 11C-raclopride (binding in dopamine D2 receptors) in the striatum of two rats; the other had 3-NP treatment only (B6) and the other had protection with ABHxD-I with 3-NP. ABHxD-I did not block original binding sites for transporter or D2 receptor, but it significantly accelerated the washout of the tracer ligand (11C-CFT or 11C-raclopride) decreasing the binding potential.

· **Neurobiology of Disease**

Senior Editor: Dr. Gary Westbrook
Vollum Institute, L 47
Oregon Health Sciences University
3181 SW Sam Jackson Park Road
Portland, OR 97201
Email: jneurosc@ohsu.edu

Title: Cerebral PET imaging and histological evidence of transglutaminase inhibitor cystamine induced neuroprotection in transgenic R6/2 mouse model of Huntington's disease

Abbreviated title: Evaluation of cystamine induced neuroprotection

Authors:

Xukui Wang[1], Aparajita Sarkar[1], Francesca Cicchetti[2], Meixiang Yu[1], Aijun Zhu[1], Kimmo Jokivarsi[1], Martine Saint-Pierre[2], Nicolas Lapointe[2], Anna-Liisa Brownell[1]

[1] Department of Radiology, Massachusetts General Hospital, Harvard Medical School, Boston, Massachusetts 02114, USA; [2] Centre de recherche en Neurosciences, RC-9800, 2705 Boul. Laurier, Ste-Foy, Québec, Canada, G1V 2G2.

Corresponding author: Anna-Liisa Brownell, Ph.D., Bartlett Hall 504R, Radiology, Massachusetts General Hospital, Boston, MA 02114, email: abrownell@partners.org

Number of figures: 6 figures

Number of tables: 2 tables

Number of pages: 28

Key words: glucose metabolism, dopamine D2 receptor, neuroprotection, cystamine, Huntington's disease, cellular inclusion

Abstract

To investigate the efficacy of cystamine induced neuroprotection, we conducted PET imaging studies of cerebral glucose metabolism with [^{18}F]FDG (2-deoxy-2-[^{18}F]fluoro-D-glucose) and striatal dopamine D2 receptor function with [^{11}C]raclopride in 42 R6/2 transgenic Huntington mice; 12 control and 30 cystamine treated animals, using intraperitoneal doses of 100, 50, 9 or 5.4 mg/kg. In the control mice, exponentially decreasing glucose utilization was observed in the striatum $N_{str}[SUV] = (41.75+/-11.80)_{58,str} *exp(-(0.041+/-0.007)*t[days])$; cortex $N_{cort}[SUV] = (24.14+/-3.66)_{58,cort} *exp(-(0.043+/-0.007)*t[days])$; and cerebellum $N_{cer}[SUV] = (34.97+/-10.58)_{58,cer}*exp(-(0.037+/-0.008)*t[days])$ as a function of age starting at 58 days. Given that the underlying degeneration rate in the cystamine treated mice is similar to that observed in control animals, the protection coefficient (β) calculated from the equation $N_t = N_{58} * exp(-(1-\beta)* k*t)$ was 0.133 +/-0.035 for the striatum; 0.122+/-0.028 for the cortex and 0.224+/00.042 for the cerebellum with a dose of 100 mg/kg. The 50mg/kg cystamine dose provided significant protection only for the striatum. Minor protection for the striatum was obtained using the lower doses of 9 or 5.4 mg/kg. Striatal binding potential of [^{11}C]raclopride in D2 receptors was 1.059+/-0.030 in the control mice, and enhanced in the cystamine treated animals in a dose dependent manner up to 1.245+/-0.063 using the 100mg/kg dose, indicative of neuronal sparing.

Histological analysis confirmed cystamine induced neuroprotection of striatal and cortical neurons. Nissl staining revealed more numerous and healthier neurons in cystamine treated animals and formation of cellular inclusions was reversed by a dose dependent matter. Cerebral imaging and histological evidence concurrently provide evidence that the inhibition of

Tgase by cystamine reflects decreased neuronal loss and support the use of cystamine as a neuroprotective agent for Huntington's disease pathology.

Introduction

Huntington's disease (HD) is an autosomal dominant inherited neurodegenerative disorder (Young and Penney, 1984). The onset of HD is usually in mid-life with a mean survival of 15-20 years after diagnosis. The clinical features of HD involve a progressive development of motor, psychiatric, and cognitive symptoms (Ross et al., 1997; Witjes-Ane et al., 2003) correlated with metabolic, neurochemical, and neuropathological changes (Albin and Tagle, 1995; Heizmann and Braun, 1992). The HD mutation is an expansion of CAG repeat in exon 1 of the HD gene that encodes a stretch of polyglutamine (polyQ) residues close to the N-terminus of the huntingtin protein (The Huntington's Disease Collaborative Group, 1993). The expanded polyQ sequence, beyond 36-40 residues, is the result of HD symptoms (MacDonald, 2003). Although the pathogenic mechanisms of HD are unknown, it is likely that abnormally expanded forms of the polyQ are the trigger of functional toxicity (Green, 1993; Burke et al., 1996), which can lead to neurodegeneration.

Aggregation of polyQ, which contains proteolytic N-terminal fragments of huntingtin in the nuclei of neurons forming neuronal intranuclear inclusions, is an important pathological hallmark of HD and has been the target of intensive investigation (DiFiglia et al., 1997; Kim et al., 1999; Meade et al., 2002). Intracellular inclusions have been found in cell models (Taniguchi et al., 2004), transgenic mice (Zemskov et al., 2003) as well as affected brain areas of HD patients (Mangiarini et al., 1996; Davies et al., 1997; Becher et al., 1998). It still remains unclear whether these inclusions are the result or the cause of neuronal death. Since transglutaminase can cross-link the mutant protein huntingtin into aggregations (Karpuj et al., 1999; Zainelli et al.,

3

2003), it has been suggested that Tgase may play a role in the etiology of HD. These findings have raised the hypothesis that inhibition of Tgase may be an effective therapeutic strategy for HD.

Cystamine is a competitive inhibitor of Tgase. This compound has the capacity to block active sites of the enzyme for the glutamine residues to form N-(γ-glutamyl)-lysine bonds in huntingtin (Folk, 1980; Lorand, 1998). Recent studies have suggested that cystamine attenuates Tgase activity, which feasibly induces reduction of abnormal movement, halt weight loss and prolong lifespan in transgenic mouse models of HD (Dedeoglu et al., 2002; Karpuj et al., 2002b).

Reduction of the cerebral glucose metabolism, observed by PET imaging, is also a well-known feature in symptomatic HD and the preclinical gene carrier state (Kuhl et al, 1982; Kuwert et al., 1990; Feigin et al., 2001). Recent studies have suggested that dopamine D2 receptor binding and glucose utilization are decreased in the animal models of HD (Araujo et al., 2000; Ariano et al., 2002; Brownell et al., 1994 and 2003). Here, we used microPET imaging to investigate whether cystamine treatment can ameliorate the cerebral energy metabolism and dopamine receptor function in the striatum of transgenic R6/2 mouse model of HD. These studies were combined to post-mortem evaluation of cystamine effects on nuclear inclusion and cell survival.

Materials and Methods

Animals: Male transgenic R6/2 mice, which depict many clinical features of juvenile HD were purchased from the Jackson Laboratories (Bar Harbor, ME). The mice were housed 3-4 per cage under standard conditions with free access to food and water. The mice were randomized and

handled under the same conditions by one investigator. In total, 42 mice were studied from the ages of 8 to 13 weeks. Weight fluctuations were closely monitored and if the total weight loss exceeded 25 %, animals were immediately euthanized according the Institutional Policy. All experiments were performed in accordance with the National Institutes of Health Guide for the Care and Use of Laboratory Animals and were approved by the Institutional Policy by the Subcommittee on Research Animals of the Harvard Medical School and Massachusetts General Hospital.

Drug administration: Neuroprotection studies were conducted in 30 R6/2 mice using 4 different doses of cystamine (Cystamine dihydrochloride, Sigma, St. Louis, MO) dissolved in PBS and prepared fresh for daily intraperitoneal (i.p.) injection starting from the age of 8 weeks and continuing for 5 subsequent weeks. The selected cystamine doses were 100mg/kg or 50mg/kg, each group comprising 6 mice; 9mg/kg dose was administered to 12 mice and 5.4mg/kg to 6 mice. To evaluate repeated injections induced stress related factors on the final results, we utilized a total of 12 R6/2 HD mice as control animals. The control mice were divided into 2 groups of 6 animals; group 1 had longitudinal PET imaging studies and received daily administration of PBS as methodological control for cystamine treated mice; group 2 strictly underwent longitudinal PET imaging studies.

Motor performance and weight assessment: Locomotor activity was video recorded for each treatment group and the control mice at the age of 12 weeks. The test consisted of recording free motion of the individual animals for 15 min in a square box (30 cm x 40 cm), bottom marked with squares of 5 cm x 5 cm. The videocamera (Sony DV Digital Handycam, 120x digital zoom) was mounted 90 cm above the box at the midpoint so that the zoomed field of view covered the bottom of the box. Recorded parameters were the area of total movement (the number of 5 x 5 cm squares covered) and the number of lines crossed (each of 5 cm) during the 15 min recording.

This is an in-house simplified version of the commercially available locomotor activity boxes, which measure light beam crossings.

MicroPET studies: For imaging studies, mice were anaesthetized with halothane (1.0-1.5% with flow rate of 3L/min oxygen and 2L/min nitrogen). A tail vein was catheterized for administration of radiolabeled ligands. A heated waterbed was used to maintain body temperature. The mouse was placed ventrally to the imaging position and the head was adjusted securely in a stereotaxic headholder, equipped with a gas inhalation system.

PET imaging studies were conducted with a microPET, P4 system (Concorde Microsystems Inc, Knoxville, TN). The length of the field of view is 8 cm and the diameter is 22 cm allowing the entire body imaging of the mouse in a single acquisition. We developed a stack for positioning the animal holders including stereotactic head frames and were able to image 4 mice at a time. The spatial resolution at the center of the imaging field is 1.8 mm and declines to the edges of the field, however, providing at least 2 mm resolution for stacked positions.

In studies of glucose metabolism, 200 µCi [^{18}F]FDG was injected into the tail vein of the animal. This compound is then transported via the blood stream into the brain and enters a metabolic cycle by hexakinase enzyme. Since hexakinase is activated by energy requirement, the accumulation of [^{18}F]FDG reflects the metabolic rate of glucose. PET imaging studies of glucose metabolism were repeated at seven different time points between the age of 58 and 86 days. Three-dimensional dynamic data were acquired in list mode for 1 hour. Imaging studies of dopamine D2 receptor function ([^{11}C]raclopride binding) were conducted in 80-day-old mice. For imaging studies, 500 µCi of [^{11}C]raclopride was injected into the tail vein and volumetric dynamic data was acquired for an hour, as described above.

In vivo imaging data analysis: Imaging data were corrected for uniformity, sensitivity, attenuation and decay. Dynamic images were processed using filtered backprojection with the Ramp filter and cut off value of 0.5 of the software ASIPRO 4.12, provided by the manufacturer. Volumetric regions of interests (VOIs), including left and right striata, cortex and cerebellum were drawn on the screen from the anatomical border based on the Mouse Brain Atlas (Paxinos and Franklin, 2001). Time dependent activity concentrations were determined for each region. These data were transferred onto a Dell XPST600 computer for final data analyses using Matlab software (Matlab, Natic, MA).

For quantification of glucose metabolism, standard unit values [SUV] were determined for each brain region (left and right striata, cortex and cerebellum) by dividing the mean radioactivity concentration obtained at the steady state by the injected radioactivity and the body mass. These values were converted to correspond to percent value of the injected radioactivity per 100 mg. The unit of SUV is percent of the injected activity per 100 mg of tissue.

For the studies of dopamine D2 receptor function, binding parameters of ^{11}C-raclopride were determined as a binding ratio of the specific and non-specific bindings. Specific binding was obtained by substracting the cerebellar radioactivity accumulation (non-specific) from striatal levels. The specific binding values calculated for the left and right striata were integrated in the time interval of 15-30 min; data from the left and right hemispheres were averaged and divided by the integrated data from cerebellum at the same time interval [the binding ratio = $\Sigma_{15\text{-}30}$ (striatum-cerebellum) / $\Sigma_{15\text{-}30}$ (cerebellum).

Evaluation of neuroprotection: Longitudinal PET imaging studies were conducted in each treatment group between the age of 8 and 13 weeks to evaluate cystamine induced changes in glucose metabolism. Age related degeneration rate was determined in 12 control mice. The values obtained in different brain regions (striatum, cortex and cerebellum) in the control mice

7

were fitted to a monoexponential function ($N_{t(brain\ region)} = N_{58,\ brain\ region} * \exp(-k*t)$) using the method of least squares and SAAM II program [Foster, 1994 #133]. For each brain region, the base (first) values were obtained at 58 days. In cystamine treated animals, the corresponding equation is $N_{t\ (brain\ area)} = N_{58,\ brain\ area} * \exp(-(1-\beta)*k*t)$, where β is the protection coefficient. Assuming that the underlying degeneration rate (k) is similar to that observed in the control mice, the value for neuroprotection coefficient β can be resolved.

Histological Evaluation: Total of 12 R6/2 transgenic mice from cystamine (8 animals) and vehicle (4 animals) treated groups were used for endpoint histological evaluation. These animals were deeply anesthetized with sodium pentobarbital (80mg/kg i.p.) and transcardially perfused with 4% buffered paraformaldehyde (PFA) (pH 7.4). The brains were removed, post-fixed in 4% PFA for approximately 8 hours, and cryoprotected in 20% sucrose. Brains were cut with a freezing microtome into 30μm-thick coronal sections that were serially collected in cold PBS and placed for 30 minutes at room temperature in a 3% hydrogen peroxide to eliminate endogenous peroxidase activity. The sections were then processed for histochemistry to visualize the mutant protein huntingtin, corresponding the nuclear aggregates possibly synonym of ongoing neuronal death and the calcium-binding protein calbindin, specifically expressed in striatal projection neurons.

After overnight incubation at 4°C with the monoclonal antibody against huntingtin (Chemicon, Temecula, CA) (dilution 1:500), the sections were extensively washed in PBS and incubated for 1 hour at room temperature in a PBS solution containing biotinylated goat anti-mouse IgG(Vector Labs, Burlingame, CA; dilution 1: 1500), Triton X-100 (0.1%), and NGS (5%). After further washing in PBS, the sections were placed in a solution containing avidin-biotin-peroxidase complex (ABC; Vector) for 1 hour at room temperature. The bound peroxidase was revealed with nickel-intensified DAB as the chromogen. After immunostaining for

huntingtin, the sections were reincubated with a polyclonal antibody raised against calbintin (Sigma, St-Louis, MA) (dilution 1:2500). The incubation procedures were the same as above, except that sections were revealed using 0.05% 3,3'-diaminobenzidine tetrahydrochloride (DAB, Sigma) and 0.01% hydrogen peroxide in 0.05M Tris-imidazole (pH 7.2) at room temperature. The reaction was stopped after 10 to 15 minutes by extensive washing in PBS.

Histochemistry: Sections were stained for Nissl substance and the presence of the enzyme nicotinamide adenine dinucleotide phosphate diaphorase (NADPH-d) was revealed by using a slightly modified version of the histochemical tetrazolium salt technique described by (Scherer-Singler et al., 1983) (Vincent and Johansson, 1983).

All immunostained and histochemically treated sections were mounted on gelatin-coated slides, air-dried, and dehydrated in ascending grades of alcohol. Finally, the sections were cleaned in xylene, and coverslipped with Permount.

Post-mortem image analyses: Nuclear inclusions, as observed with huntingtin staining were measured in the striatum and cortex using the Stereo investigator software (Microbrightfield, Colchester, VT) mounted onto a E800 Nikon microscope. One hundred inclusions were sampled in the striatum and 100 in the cortex in animals of each group. Comparison of inclusion diameters (cortical versus striatal inclusions) was performed by one-way ANOVA using Stat View 4.51.

Results

Effect of cystamine on the progression of weight loss and behavior in R6/2 transgenic mice

All animals showed weight loss during the follow up period starting from the age of 58 days. Two phases were observed during weight monitoring. In the first phase, from age of 58 days to 72 days, the control animals (vehicle treated and untreated) lost 3-5% of their total body weight,

(Ravikumar et al., 2003). Although the mechanism of 3-NP induced neurotoxicity is different than that of the extended CAG repeat, the outcome response on hexakinase activity is similar and can be detected by changes of glucose metabolism.

The basal ganglia structures are critically involved in motor control, motor planning, and behavioral learning (O'Connor et al., 1998; Ostergaard et al., 2000). Dysfunction of these subcortical nuclei can result in profound motor disturbances (e.g., ataxia, dysmetria, tremor, rigidity, and bradykinesia). Dopamine-producing neurons, which originate from the substantia nigra pars compacta (SNc) and project to the dorsal striatum, play a critical role in basal ganglia functions (Cross and Rossor, 1983; Hume et al., 1996). In HD, neuronal degeneration most specifically targets the striatum medium spiny neurons (Araujo et al., 2000; Spektor et al., 2002), which express dopamine receptors. Striatal dopamine D2 receptor density is an important indicator of many neuropsychiatric disorders and motor activity. Several studies have demonstrated that dopamine D2 receptor binding is decreased in animal models of HD (Brandt et al., 1990; Araujo et al., 2000; Ariano et al., 2002;(Brownell et al., 2003) and striatal dopamine receptor binding decreases proportionally to the degree of cell loss in this pathology (Augood et al. , 1997). Here, we found that, although the dopamine D2 receptor binding potential had no difference between the control R6/2 mice and low dose treatments of cystamine (5.4mg and 9 mg/kg), dopamine D2 receptor binding was significantly increased 15% and 17.3% when higher doses of cystamine (50mg and 100mg/kg) were administered. Our results also indicate that the increased D2 receptor binding potential in striatum feasibly reflects the decreased neuronal cell loss in cystamine treated R6/2 transgenic HD mice.

Cystamine, a competitive inhibitor of transglutaminase, may have neuroprotective effect for HD. Recent studies have supported the contribution of transglutaminase in pathogenesis of

Albin R, Tagle DA (1995) Genetics and molecular biology of Huntington's disease. Trends Neurosci 18:11-14.

Antonini A, Leenders KL, Spiegel R, Meier D, Vontobel P, Weigell-Weber M, Sanchez-Pernaute R, de Yebenez JG, Boesiger P, Weindl A, Maguire RP. (1996) Striatal glucose metabolism and dopamine D2 receptor binding in asymptomatic gene carriers and patients with Huntington's disease. Brain 119:2085-2095.

Araujo MD, Cherry SR, Tatsukawa KJ, Toyokuni T, Kornblum HI (2000) Deficits in striatal dopamine D2 receptors and energy metabolism detected by in vivo micro PET imaging in a rat model of Huntington's disease. Exp Neurol 166:287-297.

Ariano M, Aronin N, Difiglia M, Tagle DA, Sibley DR, Leavitt BR, Hayden MR, Levine MS (2002) Striatal neurochemical changes in transgenic models of Huntington's disease. J Neurosci Res 68:716-729.

Augood S, Faull RL, Emson PC (1997) Dopamine D1 and D2 receptor gene expression in the striatum in Huntington's disease. Ann Neurol 42:215-221.

Beal M, Brouillet E, Jenkins BG, Ferrante RJ, Kowall NW, Miller JM, Storey E, Srivastava R, Rosen BR, Hyman BT. (1993) Neurochemical and histologic characterization of striatal excitotoxic lesions produced by the mitochondrial toxin 3-nitropropionic acid. J Neurosci 13:4181-4192.

Becher M, Kotzuk JA, Sharp AH, Davies SW, Bates GP, Price DL, Ross CA (1998) Intranuclear neuronal inclusions in Huntington's disease and dentatorubral and pallidoluysian atrophy: correlation between the density of inclusions and IT15 CAG triplet repeat length. Neurobiol Dis 4:387-397.

Bokde A, Pietrini P, Ibanez V, Furey ML, Alexander GE, Graff-Radford NR, Rapoport SI, Schapiro MB, Horwitz B (2001) The effect of brain atrophy on cerebral hypometabolism in the visual variant of Alzheimer disease. Arch Neurol 58:480-486.

Brandt J, Folstein SE, Wong DF, Links J, Dannals RF, McDonnell-Sill A, Starkstein S, Anders P, Strauss ME, Tune LE, et al. (1990) D2 receptors in Huntington's disease: positron emission tomography findings and clinical correlates. J Neuropsychiatry Clin Neurosci 2:20-27.

Brownell A-L, Chen I.Y., Wang X., Yu M., Jenkins B.G. (2003) Neurotoxicity-induced changes in striatal dopamine receptor function. Ann of N Y Acad Sci 991:281-283.

Brownell A-L, Chen Y.I., Yu M., Wang X., Dedeoglu A., Cicchetti C., Jenkins B.G., Beal M.F. (2004 (in press) 3-Nitropropionic acid induced neurotoxicity - assessed by ultra high resolution PET with comparison to MRS. J Neurochem.

Brownell A-L, Hantraye, P., Wullner, U., Hamberg, L., Shoup, T., Shoup, T., Elmaleh, D R., Frim, D M., Madras, B K., Brownell, G L., Rosen, B R., Isacson, O (1994) PET- and MRI-based assessment of glucose utilization, dopamine receptor binding, and hemodynamic changes after lesions to the caudate-putamen in primates. Experimental Neurology 125:41-51.

Burke J, Enghild JJ, Martin ME, Jou YS, Myers RM, Roses AD, Vance JM, Strittmatter WJ (1996) Huntingtin and DRPLA proteins selectively interact with the enzyme GAPDH. Nat Med 2:347-350.

Cicchetti F, Gould PV, Parent A . (1996) Sparing of striatal neurons coexpressing calretinin and substance P (NK1) receptor in Huntington's disease. Brain Res 730:232-237.

17

Cicchetti F, Parent A (1996) Striatal interneurons in Huntington's disease: selective increase in the density of calretinin-immunoreactive medium-sized neurons. Mov Disord 11:619-626.

Cooper A, Jeitner TM, Gentile V, Blass JP (2002) Cross linking of polyglutamine domains catalyzed by tissue transglutaminase is greatly favored with pathological-length repeats: does transglutaminase activity play a role in (CAG)(n)/Q(n)-expansion diseases? Neurochem Int 40:53-67.

Cooper A, Sheu KF, Burke JR, Onodera O, Strittmatter WJ, Roses AD, Blass JP (1997) Polyglutamine domains are substrates of tissue transglutaminase: does transglutaminase play a role in expanded CAG/poly-Q neurodegenerative diseases? J Neurochem 69:431-434.

Cross A, Rossor M (1983) Dopamine D-1 and D-2 receptors in Huntington's disease. Eur J Pharmacol 88:223-229.

Davies S, Turmaine M, Cozens BA, DiFiglia M, Sharp AH, Ross CA, Scherzinger E, Wanker EE, Mangiarini L, Bates GP (1997) Formation of neuronal intranuclear inclusions underlies the neurological dysfunction in mice transgenic for the HD mutation. Cell 90:537-548.

Dedeoglu A, Kubilus JK, Jeitner TM, Matson SA, Bogdanov M, Kowall NW, Matson WR, Cooper AJ, Ratan RR, Beal MF, Hersch SM, Ferrante RJ (2002) Therapeutic effects of cystamine in a murine model of Huntington's disease. J Neurosci 22:8942-8950.

DiFiglia M, Sapp E, Chase KO, Davies SW, Bates GP, Vonsattel JP, Aronin N (1997) Aggregation of huntingtin in neuronal intranuclear inclusions and dystrophic neurites in brain. Science 277:1990-1993.

Igarashi S, Koide R, Shimohata T, Yamada M, Hayashi Y, Takano H, Date H, Oyake M, Sato T, Sato A, Egawa S, Ikeuchi T, Tanaka H, Nakano R, Tanaka K, Hozumi I, Inuzuka T, Takahashi H, Tsuji S (1998) Suppression of aggregate formation and apoptosis by transglutaminase inhibitors in cells expressing truncated DRPLA protein with an expanded polyglutamine stretch. Nat Genet 18:111-117.

Karpuj M, Becher MW, Springer JE, Chabas D, Youssef S, Pedotti R, Mitchell D, Steinman L (2002b) Prolonged survival and decreased abnormal movements in transgenic model of Huntington disease, with administration of the transglutaminase inhibitor cystamine. Nat Med 8:143-149.

Karpuj M, Becher MW, Steinman L (2002a) Evidence for a role for transglutaminase in Huntington's disease and the potential therapeutic implications. Neurochem Int 40:31-36.

Karpuj M, Garren H, Slunt H, Price DL, Gusella J, Becher MW, Steinman L (1999) Transglutaminase aggregates huntingtin into nonamyloidogenic polymers, and its enzymatic activity increases in Huntington's disease brain nuclei. Proc Natl Acad Sci U S A 96:7388-7393.

Kelly P, Graham DI, McCulloch J. (1982) Specific alterations in local cerebral glucose utilization following striatal lesions. Brain Res 233:157-172.

Kim M, Lee HS, LaForet G, McIntyre C, Martin EJ, Chang P, Kim TW, Williams M, Reddy PH, Tagle D, Boyce FM, Won L, Heller A, Aronin N, DiFiglia M (1999) Mutant huntingtin expression in clonal striatal cells: dissociation of inclusion formation and neuronal survival by caspase inhibition. J Neurosci 19:964-973.

Kuhl D, Phelps ME, Markham CH, Metter EJ, Riege WH, Winter J (1982) Cerebral metabolism and atrophy in Huntington's disease determined by 18FDG and computed tomographic scan. Ann Neurol 12:425-434.

Oliverio S, Amendola A, Rodolfo C, Spinedi A, Piacentini M (1999) Inhibition of "tissue"

transglutaminase increases cell survival by preventing apoptosis. J Biol Chem

274:34123-34128.

Ostergaard K, Sunde NA, Dupont E (2000) Basal ganglia disease. Functional neuroanatomy and

therapeutic perspectives. Ugeskr Laeger 162:5480-5483.

Palombo E, Porrino LJ., Bankiewicz KS., Crane AM., Sokoloff L., Kopin IJ. (1990) Local

cerebral glucose utilization in monkeys with hemiparkinsonism induced by intracarotid

infusion of the neurotoxin MPTP. J Neurosci 10:860-869.

Pavese N, Andrews TC, Brooks DJ, Ho AK, Rosser AE, Barker RA, Robbins TW, Sahakian BJ,

Dunnett SB, Piccini R (2003) Progressive striatal and cortical dopamine receptor

dysfunction in Huntington's disease: a PET study. Brain 126:1127-1135.

Paxinos G, Franklin KBG. (2001) The Mouse Brain in Stereotaxic Coordinates. 2nd Edition. San

Diego, California: Academic Press.

Ravikumar B, Steward A, Kita H, Kato K, Duden R, Rubinsztein DC (2003) Raised intracellular

glucose concentrations reduce aggregation and cell death caused by mutant huntingtin

exon 1 by decreasing mTOR phosphorylation and inducing autophagy. Hum Mol Genet

12:985-994.

Ross C, Margolis RL, Rosenblatt A, Ranen NG, Becher MW, Aylward E (1997) Huntington

disease and the related disorder, dentatorubral-pallidoluysian atrophy (DRPLA).

Medicine (Baltimore) 76:305-338.

Scherer-Singler U, Vincent SR, Kimura H, McGeer EG (1983) Demonstration of a unique

population of neurons with NADPH-diaphorase histochemistry. J Neurosci Methods

9:229-234.

Table 1.   Cerebral PET imaging revealed an exponential decrease of $[^{18}F]$FDG accumulation in various brain areas of transgenic HD mice as a function of age (also see Figure 2). Degeneration rates (k) in different brain structures in 12 control mice were calculated using the equation $N_t = N_{58} * \exp(- k*t)$.   Assuming that the underlying regional degeneration rate is similar in the cystamine treated mice, the protection factor (β) was calculated using an equation $N_t = N_{58} * \exp(-(1-\beta)* k*t)$. N=number of animals; significance [P] <0.05.

Treatment	N	Striatum	Cortex	Cerebellum
		D e g e n e r a t i o n r a t e (k) [1/day]		
Control	12	0.041+/-0.007	0.043+/-0.007	0.037+/-0.008
		P r o t e c t i o n f a c t o r (β)		
Cystamine; 100 mg/kg	6	0.133+/-0.035 [P]	0.122+/-0.028 [P]	0.224+/-0.042 [P]
Cystamine; 50 mg/kg	6	0.123+/-0.041 [P]	0.020+/-0.012	0.088+/-0.032
Cystamine; 9 mg/kg	7	0.033+/-0.012	0.009+/-0.007	0.021+/-0.014
Cystamine; 5.4 mg/kg	4	0.003+/-0.002	0.012+/-0.005	0.061+/-0.035

Figure legends

Figure 1. Color coded images of $[^{18}F]$FDG accumulation in the brain of transgenic HD mice (R2/6 mice) at the age of 85 days. The mice were treated with vehicle (PBS) or with different doses of cystamine starting from the age of 58 days. The top row illustrates a comparison of $[^{18}F]$FDG accumulation in a wild-type mouse. Coronal, axial and sagital levels show activity distribution at the mid-striatal levels 40 min after administration of $[^{18}F]$FDG revealing the highest accumulation with a dose of 100 mg/kg cystamine. Accumulation in the cerebellum and Harderian gland is visible on axial and sagital sections. The slice thickness is 1.26 mm.

Figure 2. Exponential decrease of glucose utilization as a function of age in striatum, cortex and cerebellum of transgenic HD mice (R2/6) based on PET imaging studies of $[^{18}F]$FDG accumulation starting from the age of 58 days. This data is averaged from a group of 12 control mice comprising 6 vehicle treated (PBS) and 6 untreated R6/2 mice.

Figure 3. Post-mortem histological evaluation of HD R6/2 transgenic mice treated with the transglutaminase inhibitor cystamine. Photomicrographs illustrate frontal sections through the striatum at the level of the anterior commissure in wild-type (a), R6/2 HD mice treated with vehicle (c) and cystamine treated HD mice (e). Nissl staining reveals that following cystamine treatment (100 mg/kg), striatal cells are more numerous and depict a healthier appearance (e) closely resembling that of wild-type (a). The presence and intensity of the enzyme B-nicotinamide adenine dinucleotide phosphatase (nadph-d), associated to a subpopulation of interneurons not targeted in HD, shows no significant difference in wild type, vehicle or cystamine treated HD mice (b, d,f). Scale bar in a,c,e: 100μm; b,d,f: 40μm.

Figure 4. Neuroprotective effects of cystamine are dose dependent. High dose treatment (a, 100mg/kg) shows more neuroprotection (number of cells and overall health appearance) than lower doses (b, 50mg/kg), which also demonstrate neuroprotective potential, as revealed by Nissl staining. Scale bar: 100μm.

Figure 5. Effects of cystamine treatment on cellular inclusions in R6/2 HD mice. Photomicrographs depicting abundant cellular inclusion staining (black) within neuronal elements of the striatum (b) and the cortex (c) of R6/2 HD mice treated with vehicle. Neurons of animals treated with cystamine (dose 100 mg/kg) depict cellular inclusions diminished in size as illustrated by the lack of staining at low (d) and high magnification (e-f) in the striatum (e) and cortex (f) (see black arrows) as compared to untreated animals (a). Scale bar in a,d = 250μm and in b,c,e,f = 25μm.

Figure 6. Dose dependent decrease in striatal (a) and cortical (b)inclusion size after cystamine treatment. Column 1 illustrates inclusion size in control mice; Column 2 - after cystamine administration of 9 mg/kg; Column 3 - after cystamine treatment of 50 mg/kg and; Column 4 - after treatment with a dose of 100 mg/kg. Cystamine induced decrease in inclusion size is 52.8% in striatum and 18.0% in cortex using 100mg/kg dose, indicating stronger protective effect in the striatum than in the cortex.
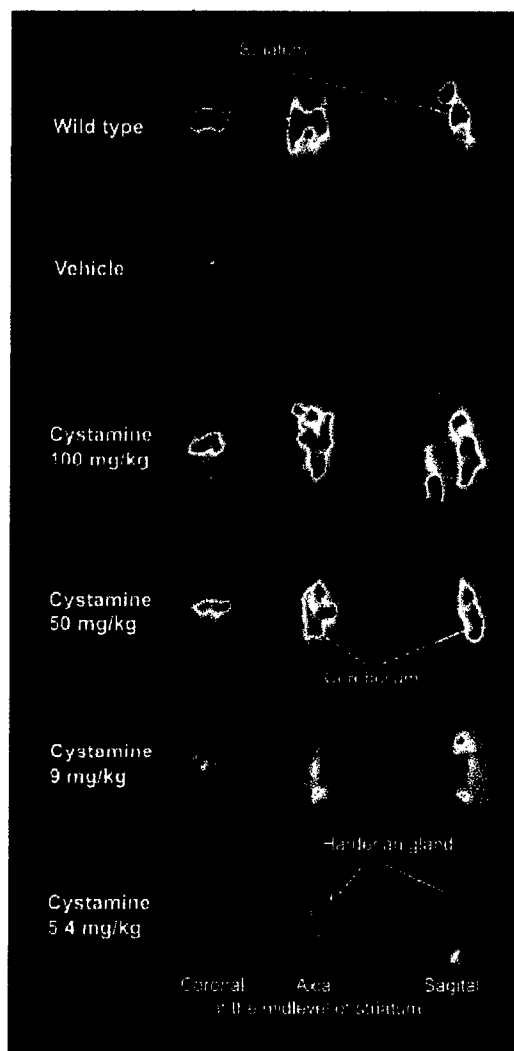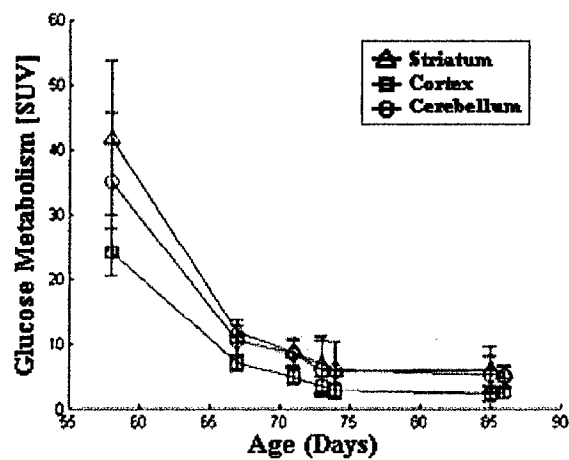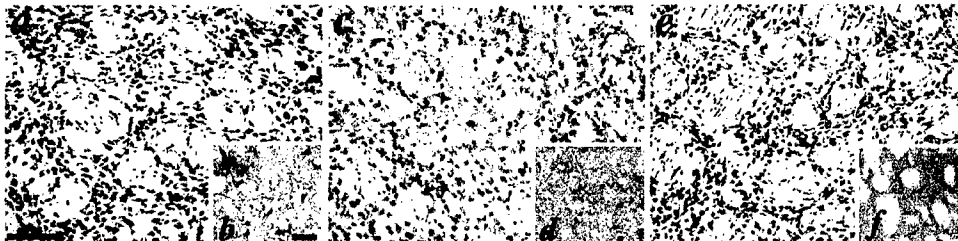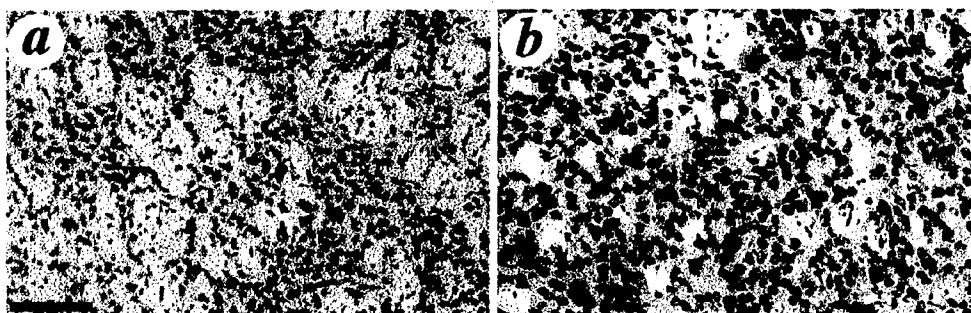
Figure 1.

Figure 2.

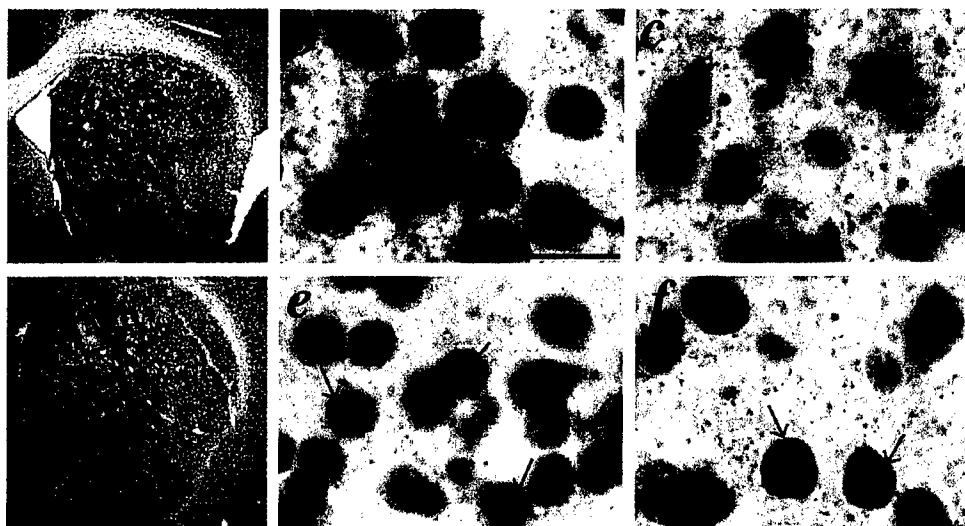Figure 3.

Figure 4.

Figure 5.

Striatum

Figure 6a.

Cortex
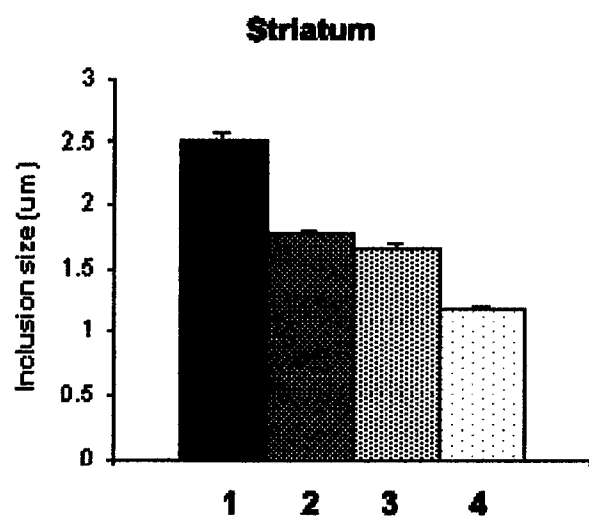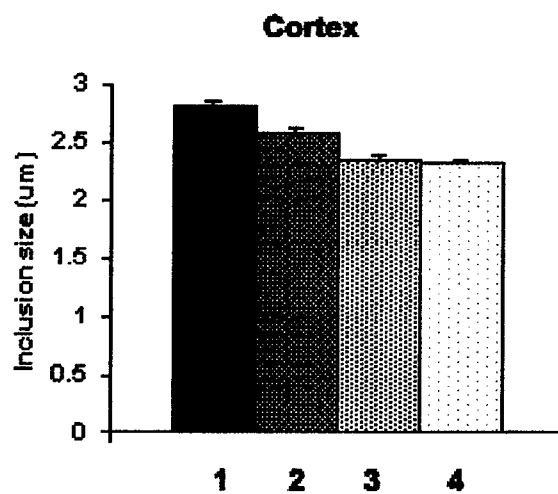
Figure 6b.

Performance Evaluation of MMP-II: A Second-Generation Small Animal PET

John A. Correia, *Member, IEEE*, Charles A. Burnham, *Senior Member, IEEE*, David Kaufman, Anna-Liisa Brownell, and Alan J. Fischman

Abstract—We have completed construction of a second-generation, single-plane small animal PET instrument based on LSO detectors. The second-generation design addresses some of the limitations in the first-generation. The purpose of the work reported here was to characterize the physical performance of this instrument. Results of the performance measurements include: Spatial resolution = 1.25 mm at field center and 1.5 mm at 2 cm radius; point source sensitivity = 56 cps/uCi,; scatter fractions of 0.019 and 0.056 in 3.8 and 6 cm diameter cylinders respectively; linearity of reconstructed signal within 5% up to 100 uCi/cc and acceptable dead-time performance up to 25 k true cps. Examples of phantom and animal images are also presented.

Index Terms—LSO, PET, small animal imaging.

I. INTRODUCTION

DURING the recent past there has been a growing interest in the physiologic and biochemical imaging of small animals. Several factors have contributed to this interest. Firstly, the tremendous growth of the genetic engineering field has resulted in the development of a number of models of human disease in genetically manipulated mice and the study of such models is of great interest. Positron emission tomography (PET) provides the best available means of nondestructively studying the time course of general physiological parameters as well as specific biochemical changes in such disease models. Secondly, the pharmaceutical industry has become more and more aware of the advantages of nondestructive methods for preliminary drug kinetic studies. A major advantage of using PET for these studies is that the course of a labeled drug can be followed over time in a single animal thus requiring fewer animals and resulting in lower variability of parameter estimates due to tighter experimental controls.

The availability of new detector materials such as Lutetium Oxyorthosylicate (LSO), Yttrium Aluminum Pyrovskite (YAP) and Gadolinium Silicate (GSO) for PET have led to the possibility of producing small-scale, high-resolution instruments which are appropriate for rodent imaging. The major properties of these materials that make higher resolution possible are high light output and fast light decay. Increased light output makes possible the identification of very small detectors while fast decay allows for fast timing and potentially high-count rate ca-

pability. There have recently been a number of efforts toward the development of small-animal PET imaging devices. The earliest used Bismuth Germinate (BGO) detectors [1]. Cherry, *et al.* [2], [3] subsequently developed the first LSO-based animal-imaging instrument having approximately 2 mm spatial resolution and volumetric imaging capability. A number of other investigators have developed scintillator-based systems at this resolution using either LSO [4], [5], YAP [6], [7] or GSO [8] scintillators and several different types of light readouts including position sensitive photomultiplier tubes and photodyode arrays [9], [10]. Several investigators including ourselves have designed and constructed scintillator-based detector modules with resolution in the 1 mm range [6]–[8]. Others have taken alternative approaches to the design of very high-resolution detector modules [9], [10], for example stacked wire chambers with lead converter plates.

We have previously developed a single-plane, LSO-based-PET instrument with 1 mm spatial resolution in objects on the scale of small animals [6]. Although this instrument performed well it was limited by low sensitivity due to the use of short crystals and by limitations in detector performance due to light losses at the center of the detector blocks. In order to address these issues, a second-generation instrument, Millimeter PET-II (MMP-II), which sacrifices a small amount of spatial resolution in order to improve detector performance was designed and constructed [11], [12].

The purpose of the work reported here was to evaluate the physical performance of this recently completed second-generation instrument, which is intended to be a proof of concept for the LSO detector module design. Our eventual aim is to extend the design to a volumetric device.

II. METHODS

A. System Description

The second-generation system consists of a single 14.7 cm diameter ring of 1.2 mm wide by 7 mm deep by 4.5 mm high LSO crystals organized into 36 blocks of ten crystals each viewed by two photomultipliers. The blocks are positioned so that each block end is at the center of a photomultiplier. A total of 36 photomultipliers view the crystal array. The details of the light optics and surface preparations of the detector modules have been previously described [6], [11]. Crystal events are identified via a series of block-specific lookup tables for crystal identification based on a normalized difference in photomultiplier signals, energy bounds to account for variations in crystal response across blocks and gain corrections. These have also been described previously [6], [11]. A diagram of the system electronics and data
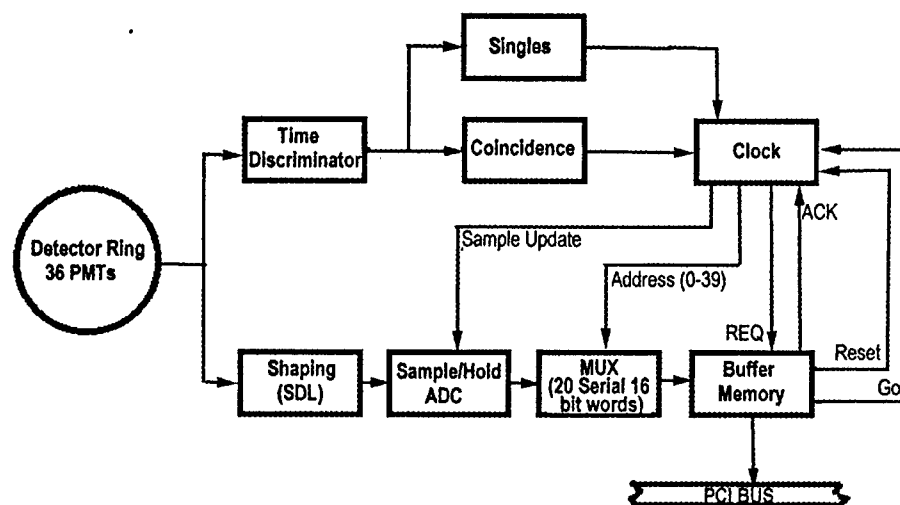
Fig. 1.   Diagram of MMP-II electronics and data acquisition.

TABLE I
DESIGN SPECIFICATIONS OF MMP-II SINGLE-PLANE SMALL-ANIMAL PET

PARAMETER	MMP-II SPECIFICATION
Diiameter (cm)	14.7
LSO Crystals	360
Element Size (mm)	.2 x 4.5 x 7
Number of PMTs	36
Resolution (mm) Center	1.2
Resolution (mm) 2.5 cm	1.8
Axial Resolution (mm)	1.7
Sensitivity (cps/uCi)	>70

acquisition is shown in Fig. 1 and the instrument's design specifications are summarized in Table I.

Once a coincidence is identified all 36 photomultiplier signals are transferred through a buffered interface into a PC computer via the PCI bus. The crystal identification and binning computations are subsequently carried out in software. System singles rates are also transferred with each event for use in computing randoms and dead time corrections.

As demonstrated previously [11] modification of crystal-element size from 1 x 5 x 4.5 mm to 1.2 x 7 x 4.5 mm and improvement of light optics within the blocks leads to improved light collection compared to the first generation system (from 50%–65%) and better identification of the end crystals.

B. Performance Evaluation

In order to characterize the performance of the MMP-II system, a series of physical measurements have been carried

out. These include measurements of spatial resolution, axial resolution, sensitivity, field uniformity, linearity and count-rate response. The measurement methods are described in detail below.

High contrast spatial resolution was measured using line sources of ^{18}F placed axially in the field. Each source consisted of a 22ga stainless steel spinal needle (0.4 mm i.d.) sealed with quick-drying epoxy after filling with approximately 30 uCi of [18]F. A series of data sets were collected for five minutes each with two sources in the field, one at the center and one at a radius which was varied in 0.5 cm steps from collection to collection. The data sets were sensitivity corrected and reconstructed by filtered back-projection using a ramp filter and a zoom factor of two. FWHM and FWTM were measured from Gaussian fits to profiles through the source centers and corrected for finite source size.

The system sensitivity was measured for both a point source and an extended cylinder source of [18]F. The point source consisted of 1.8 uCi of radioactivity absorbed into a cotton ball that been packed into the end of a 19 gage spinal needle. The cylindrical source consisted of a 4.5 cm diameter by 4.5 cm high plastic cylinder containing an initial radioactivity concentration of 8 uCi/cc. Sensitivity collections were carried out at low count rates such that the contribution to the total signal from random coincidences was below three percent and scattered coincidences are included in the sensitivity determination.

The energy bounds used were typical of those used in practice, approximately 60%–125% of the crystal photopeak energies, and total counts were corrected for decay during acquisition.

The axial response of the instrument was measured using a collimator with a 4.5 mm z-gap. This gap can be reduced to provide thinner slices by changing the collimator. Measurements were made at the field center and at 2 cm radius using a point source of ^{18}F fabricated as described above. The source was stepped through the instrument in 0.1-mm increments. The total

coincidence count rate was recorded at each point and all values were corrected for decay back to the start of the measurement sequence.

The uniformity of reconstructed signal was measured in a 4.5 cm diameter cylinder filled with ^{18}F solution. Data sets were collected for a series of four differing total counts, corrected for randoms, sensitivity variations and attenuation and by filtered back-projection reconstructed using a Hanning filter. A circular ROI encompassing the whole object was placed on each image and a histogram of the count distribution extracted. Since both statistical noise and nonuniformity contribute to the spreading of the histograms, an estimate of the nonuniformity contribution was made by extrapolating the measured standard deviation as a function of total events collected to infinite events.

The linearity of reconstructed radioactivity over a dynamic range of 10:1 was measured using an array of five 3 mm-diameter cylindrical sources arranged in a radially symmetric pattern 1.5 cm from the center of a 4 cm cylindrical plastic absorber. Image data sets were collected for 15 min duration at an interval of 2 h. Data were corrected for attenuation, randoms and sensitivity variations and values of reconstructed signal were extracted from small regions-of-interest centered over the cylinders.

The system scatter fraction was measured for several cylindrical scatterer diameters. Polyethylene cylinders of 3.8 and 6 cm diameter were used as scattering medium. The former is close to the maximum object size that can be accommodated by the instrument and the latter represents more typical objects such as rodent torso. In each case a line source of ^{18}F prepared as described above was placed at the center of the scatterer and a low count rate, moderate total count image was collected. The random rates for these collections were below 2%. The sources were aligned at the field center. Sinogram data were summed over angle to provide a single integrated projection. The scatter fraction was computed as the sum of all events in the region below 1% of the peak counts divided by the sum of all events.

The count-rate response of the system electronics was measured using a 3 cm-diameter source of ^{13}N in solution placed at the field center. A series of 2 min data collections were carried out over a dynamic range of 500:1 in radioactivity concentration.

III. RESULTS

The results of the measurements described in the previous section are presented in detail below and compared with simulated values where appropriate.

Fig. 2 shows the results of the high contrast spatial resolution measurements. The measured FWHM resolution is 1.25 mm at the center of the field and 1.5 mm at 2 cm radius. The FWTM, also illustrated, are consistent with a Gaussian response.

The measured sensitivities are presented in Table II along with comparable values determined by Monte Carlo simulation. The point source sensitivity based on the measurements described was determined to be 59 cps/uCi (0.16% of emitted photons) and that for the cylindrical source 386 cps/(uCi/cc). A separate set of measurements using a ^{68}Ge point source gave comparable results.
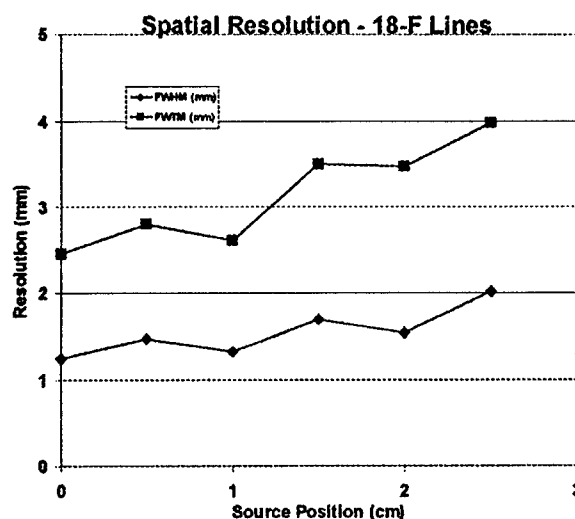

Fig. 2. Spatial resolution as a function of field radius measured with 0.4 mm 18-F line sources. Measurements are corrected for source size. FWHM and FWTM determined from Gaussian fits are shown.

TABLE II

COMPARISON OF MEASURED AND SIMULATED SENSITIVITIES FOR POINT SOURCE AND CYLINDER. MEASUREMENTS WERE MADE WITH ^{18}F

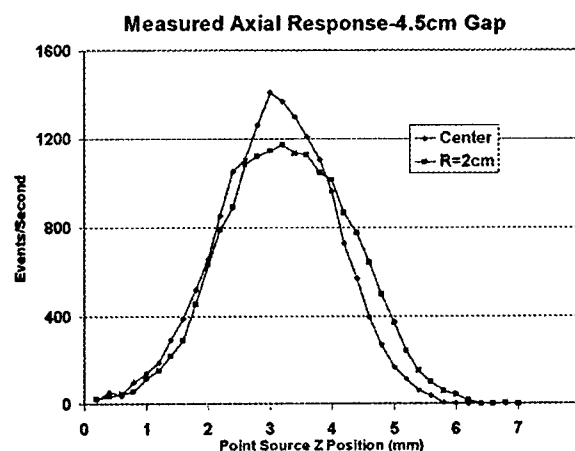| SENSITIVITY	Measured	Simulated
Point (cps/uCi)	59	70
Point (percent)	0.16	0.19
4.5 cm Cylinder (cps/uCi/cc)	386	402

Fig. 3. Axial response measurements at field center and 2 cm radius for 4.5 cm z-gap. An ^{18}F point source of 0.4 mm diameter was stepped at 0.1 mm steps axially through the field.

The results of the axial response measurements are shown in Fig. 3. The axial resolution was measured from fitted Gaussians to be 1.9 mm at the field center and 2.3 mm at 2 cm radius.
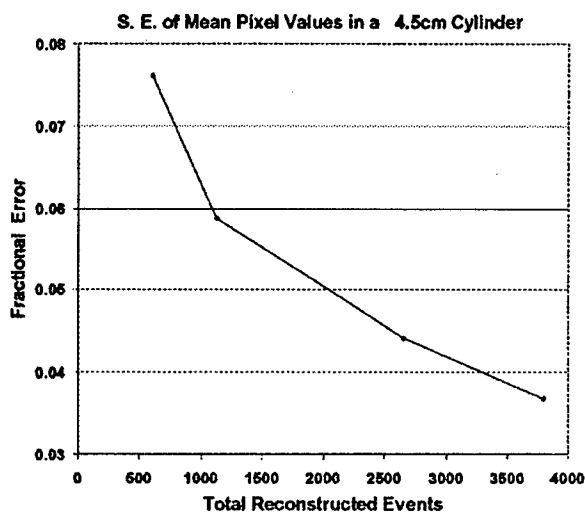
S. E. of Mean Pixel Values in a 4.5cm Cylinder

Fig. 4. The standard deviation of the reconstructed pixel values over a 4.5 cm cylinder of ^{18}F at four levels of total counts.
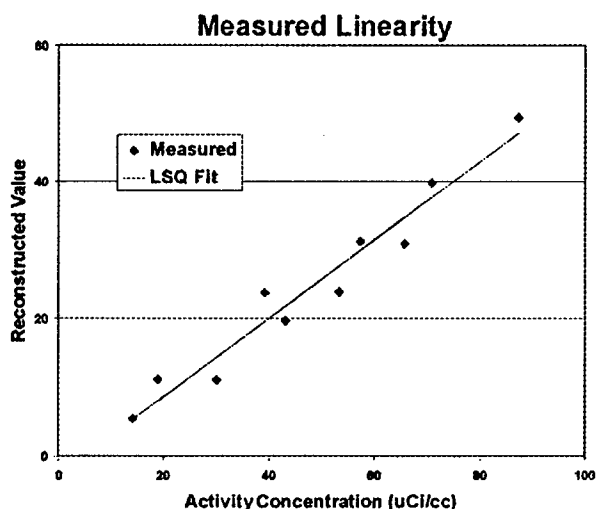

Measured Linearity

Fig. 5. Reconstructed values in 3 mm cylinders located at 1.5 cm radius in a 4 cm absorber. Linear least squares fit to the measured values is also shown.

Scatter Measurement - 6cm Cylinder

Scatter Measurement - 3.8 cm Cylinder

Fig. 6. Measurement of scatter distribution from a line source of ^{18}F at the center of two different sized tissue equivalent cylindrical absorbers. Shown is the sum of the projection data over all angles. The measured scatter fraction is 0.019 for the 3.8 cm absorber and 0.056 for the 6 cm absorber.

Similar results were obtained in separate experiments using a ^{68}Ge point source.

The results of the field uniformity measurements described above are shown in Fig. 4. The extrapolated nonuniformity at infinite count density resulting from this procedure is approximately 3.25%.

The system response to varying radioactivity concentration in 3 mm diameter cylindrical objects is shown in Fig. 5. The measured concentrations and the corresponding linear least squares fit to them are consistent with linear response over a dynamic range of 10 : 1 in radioactivity concentration.

Fig. 6 summarizes the scatter correction measurements described above. The integrated projection data for cylindrical scatterers of two different sizes is shown. The measured scatter fraction for the smaller (3.8 cm diameter) cylinder was 0.019
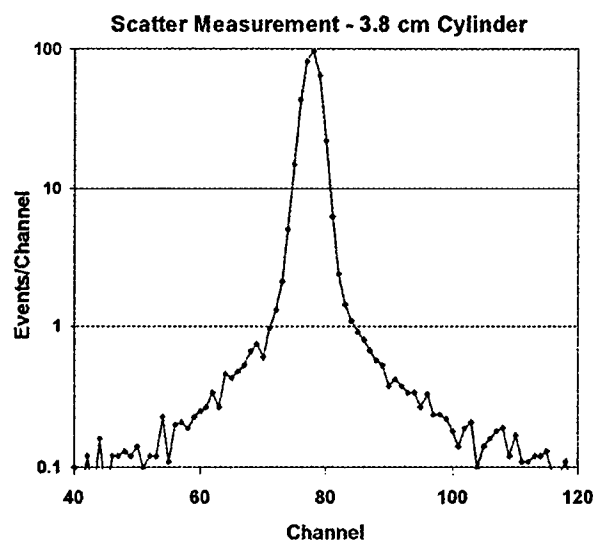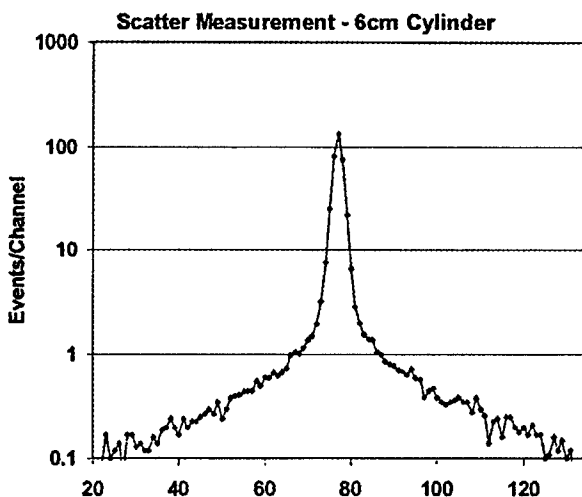
and that for the larger (6 cm diameter) was 0.056. The result for the smaller scatterer agrees well with the value of 0.025 predicted by Monte Carlo simulation but the measured result is somewhat higher than the Monte Carlo result of 0.04 for the larger.

Fig. 7 shows plots of the singles, total coincidences, true coincidences and random coincidences over a 500 : 1 dynamic range of total coincidence count rate. The limiting useful count rate defined as that at which randoms equals trues was determined to be 29 000 true coincidences per second. At this rate the measured system dead time was 53%.

In order to demonstrate the system's imaging capability several extended objects were imaged. Fig. 8 shows an image of a high-resolution micro-Jaczczak phantom consisting of triangular arrays of cold rods surrounded by radioactivity. The rod diameters in mm are indicated and the rod spacing in each array is
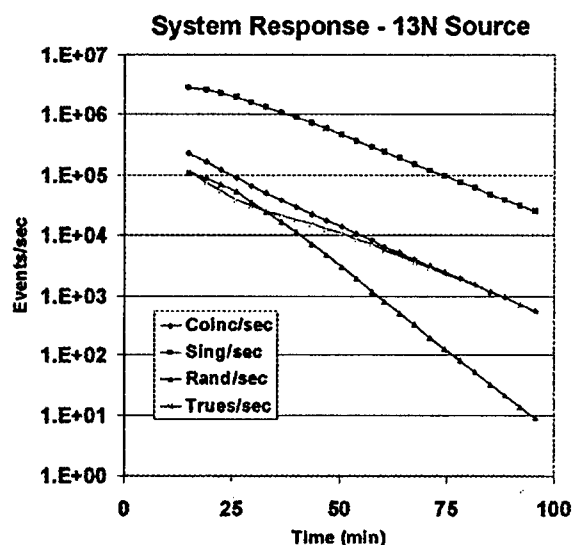
Fig. 7. Count-rate performance: Shown are singles, total coincidences, trues and randoms measured with a decaying source of 13-N solution contained in a 3.5 cm cylindrical container. The 100 min time scale corresponds to ten half-lives or a dynamic range of approximately 500:1 in the data shown.
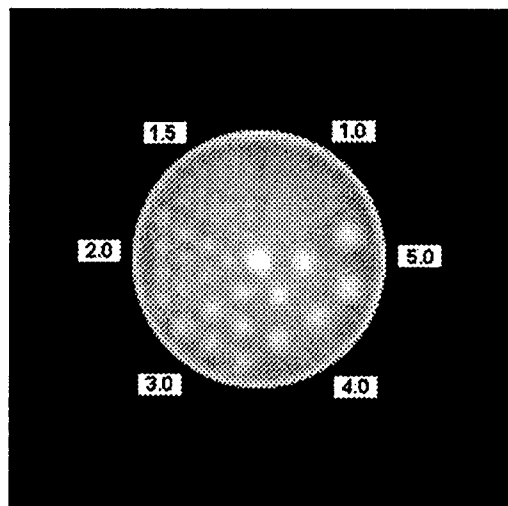

Fig. 8. Image of a high-resolution micro-Jaszczak cold spot phantom of diameter 4.5 cm filled with ^{18}F. The cold rod sizes in mm are indicated. The rod separation is two times the diameter in each array and the image contains 60 M total coincidence events.

twice the rod diameter. The data were corrected for randoms, attenuation and nonuniformity but not scatter corrected. The data set collected consists of approximately 60 million events. The 1.5 mm cold rods are well separated and a hint of the 1 mm rods can be seen near the object center, but they become blurred with increasing radius due to decreasing resolution.

Fig. 9 shows the distribution of ^{18}F radioactivity in the heart of a 25 gm mouse 45 min after the injection of approximately 2 mCi of FDG. The mouse is under anesthesia and no cardiac gating was used. The myocardial wall is clearly separated from the surrounding ventricle.
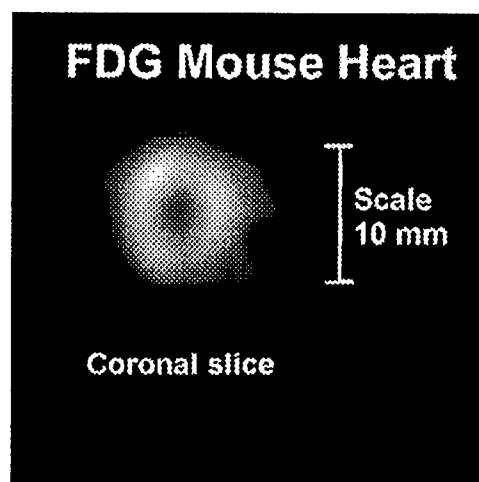

Fig. 9. ^{18}F-FDG image of a mouse heart in coronal section. The animal is anesthetized and no cardiac gating was applied. The myocardial wall and ventricle are well separated.

IV. DISCUSSION

A second-generation single-plane small animal PET has been completed and its properties evaluated experimentally. Most of the parameters evaluated agree reasonably well with those predicted in preliminary design studies. The measured sensitivities however are slightly lower than simulated values, 4% lower for the extended cylindrical source and 20% lower for the point source. These differences can be explained by the fact that additional events in the real system may be rejected based on energy criteria due do detector-block nonidealities. Similarly, the measured scatter fraction for the larger scatterer is higher than predicted by approximately 30%. This is as yet unexplained and may be the result of the data analysis method.

The system described here is a second-generation device intended to address some of the limitations of the first generation [6]. In the original system 5 mm deep detectors were used in order to bias detection toward single interaction events. Subsequent simulation studies [12] showed that this depth could be increased to 7 mm without a major increase in multiple interactions. Further the first-generation system was based on blocks of twelve 1 mm wide crystals yielding 1 mm spatial resolution at the center. This design yielded relatively high light losses at the center of the blocks and difficulties in identifying some end crystals. To address this limitation some resolution was sacrificed in the second-generation system to improve block performance. Crystal widths were increased to 1.2 mm and organized in blocks of ten resulting in a concomitant increase in detector-ring diameter from 12.5 to 14.6 cm and a decrease in central resolution to 1.25 mm. The overall effect of these changes was to increase sensitivity by approximately a factor of two and improve block performance considerably.

The intent of constructing the single-plane system described here was to develop approaches to detector design and data processing which could be extended to a volumetric system and such a design has been developed through bench-top studies and simulation [12]. However, a single-plane is still a useful tool for some types of small animal imaging studies, particu-

larly those involving slowly varying radioactivity distributions such as ^{18}F-FDG.

REFERENCES

[1] P. M. Bloomfield et al., "The design and physical characteristics of a small-animal PET," Phys. Med. Biol., vol. 40, pp. 1105–1126, 1995.

[2] A. F. Chatziioannou et al., "Performance evaluation of MicroPET: A high resolution lutetium oxyorthosilicate PET scanner for animal imaging," J. Nucl. Med., vol. 40, pp. 1164–1175, 1994.

[3] S. R. Cherry et al., "MicroPET: A high resolution PET scanner for imaging small animals," IEEE Trans. Nucl. Sci., vol. 44, pp. 1161–1166, 1997.

[4] J. J. Vaquero et al., "Performance characteristics of a compact, position sensitive LSO module," IEEE Trans. Med. Imaging, vol. 17, pp. 967–978, 1998.

[5] M. V. Green et al., "High resolution PET, SPECT and projection imaging in small animals," Comput. Med. Imaging Graph, vol. 25, pp. 79–96, 2001.

[6] J. A. Correia, C. A. Burnham, D. Kaufman, and A. J. Fischman, "Development of a small animal PET imaging device with resolution approaching 1 mm," IEEE Trans. Nucl. Sci., vol. 46, pp. 631–635, 1999.

[7] R. S. Miyaoka, S. G. Kohlmyer, and T. K. Lewellen, "Design of a micro crystal element (MICE) detector unit," J. Nucl. Med., vol. 41, p. 19P, 2000.

[8] A. Bevilaqua et al., "A Monte-Carlo simulation of a small animal PET with 1 mm resolution," IEEE Trans. Nucl. Sci., vol. 46, pp. 697–701, 1999.

[9] P. Bruyndoncks et al., "Performance study of a 3D small animal PET scanner based on BaF2 crystals and a photosensitive wire chamber," Nucl. Inst. Methods, vol. A392, pp. 407–413, 1997.

[10] A. P. Jeavons et al., "A 3D HIDAC-PET camera with sum-millimeter resolution for imaging small animals," IEEE Trans. Nucl. Sci., vol. 46, pp. 1067–1072, 1999.

[11] J. A. Correia, C. A. Burnham, D. Kaufman, and A. J. Fischman, "Performance of a small animal PET instrument with 1 mm resolution," in Proc. IEEE Medical Imaging Conf. Conf. Rec., Seattle, WA, Oct. 1999, pp. M7-32: 1–5.

[12] ——, "Design studies for volumetric high resolution small animal PET," in Proc. IEEE Medical Imaging Conf. Conf. Rec., Lyon, France, Oct. 2000, pp. 2639–2643.
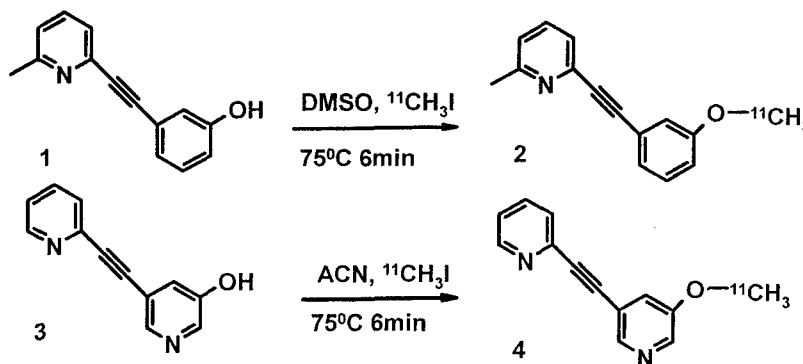
Synthesis of [11C]Methoxymethyl-MTEP and [11C]Methoxy-PEPy, potent and selective PET radioligands for Metabotropic Glutamate Subtype 5 (mGlu5) receptor

Meixiang Yu[1], Thomas Klaess[2], Alan P. Kozikowski[2], Anna-Liisa Brownell[1]

[1]Department of Radiology, Massachusetts General Hospital, Boston, MA.
[2]Departments of Neurology, Georgetown University Medical Center, Washington, DC

Metabotropic glutamate receptors (mGluRs) are a family of receptors coupled with G-protein in the mammalian nervous system and are activated by L-glutamate. Excessive activation of mGluRs has been implicated in several disease states including pain, anxiety, depression, drug addiction or withdrawal. Research of the mGluRs has been hampered because of the lack of in vivo imaging ligands. We have developed radio-labeling for two antagonists of mGluR5; 2-[(3-methoxy-phenyl) ethynyl]-6-methyl-pyridine (M-MPEP, 2), a novel

Synthesis of [11C]M-MPEP (2) and [11C]M-PEPy (4)

ligand with high affinity (Kd=2 nM), and 3-methoxy-5-(pyridin-2-ylethynyl)pyridine (M-PEPy, 4) also a mGlu5 antagonist with high affinity (Kd=3.4 nM). O.5 mg of precursor 1 dissolved in 400 μL DMSO and 6 mg KOH was used to react with [11C]CH3I, which was produced by standard method. The reaction mixture was heated at 75^0C for 6 min, after which [11C]M-MPEP was purified on a μ-Bondapak® C-18 preparative HPLC column (7.8 × 300 mm, Waters) by washing with methanol and phosphate buffer (pH 7.4) 60/40 at 6 ml/min, with 40% yield. Similarly, O.5 mg of precursor 2 dissolved in 400 μL acetonitrile (CAN) and 6 mg of KOH was used to receive [11C]CH3I, then the reaction mixture was heated at 75^0C for 6 min. [11C]M-PEPy was purified on a above HPLC system, by washing with methanol and phosphate buffer (pH 7.4) 50/50 at 6 ml/min, with 50.5% yield.

The radiolabeled ligands were administered into the normal rats (male Spraque-Dawley, 2 mCi into the tail vein) to evaluate in vivo biodistribution by PET. In 3 min the activity reached the maximum in the brain followed by rapid washout. The abdominal area (liver, spleen and pancreas) had the highest accumulation and the radioactivity did not wash out during the 60 min follow up time. In conclusion, we have successfully labeled M-MPEP and M-PEPy with C-11 in high yield, and in vivo imaging studies have shown that the ligands go through the blood brain barrier. Further analyses will be done to localize possible specific binding sites in the brain.

No. 808

IMAGING OF THE DOPAMINE SYSTEM IN OLFACTORY BULB BY POSITRON EMISSION TOMOGRAPHY (PET) IN RATS.

M. Yu*[1], A. Zhu[1], X. Wang[1], K. Jokivarsi[1], A. Brownell[1]. [1]Radiology, Massachusetts General Hospital, Harvard Medical School, Boston, MA, United States. (652072)

Objectives: Olfactory disorders in Alzheimer's disease (AD) and Parkinson's disease (PD) have been the topic for the work both in clinical and in research. The olfactory deficits involve both identification and recognition of odors and detection thresholds. The pathological basis in PD is well known: the olfactory bulb (OB) contains numerous Lewy bodies and severe neuronal loss is present in the anterior olfactory nucleus. The olfactory function is disordered especially in the idiopathic PD. In AD there is a close relationship between the olfactory and cortical degenerative changes indicating that olfactory bulb and tract is one of the earliest events in the degenerative process of the central nervous system. In vitro study and immunochemistry studies have demonstrated that D1 and D2 had similar regional distributions in rat, monkey, and human brain, with the most intense staining in striatum, olfactory bulb, and substantia nigra, regions known to have dopaminergic neurons and innervations. However, dopamine transporter (DAT) mRNA is not abundant in the olfactory bulb at any stage of development. It is important to confirm these in vitro information with in vivo imaging data, and the in vivo imaging study in olfactory bulb might be an assistant method to identify the PD and AD in the earlier disease development stage. However, according to our knowledge, there is no report about the in vivo imaging of the dopamine system in the olfactory bulb. **Methods:** [^{11}C]CFT and [^{11}C]raclopride were used to imaging the dopamine transporter and dopamine D2 receptor respectively in rats. Concord MicroPET system was used to do the dynamic imaging study. **Results:** During 20-40 min, the average counts ratio of striatum/cerebellum were 3.64±0.38 (n=5) and 1.91±0.18 (n=6) for DAT and D2 respectively, and the average counts ratio of olfactory bulb /cerebellum were 1.42±0.16 (n=5) and 1.11±0.10 (n=6) for DAT and D2 respectively. **Conclusions:** PET imaging study in rats showed that dopamine transporter consistently expressed in olfactory bulb and D2 receptor is rarely expressed in the olfactory bulb.

No. 300

SYNTHESIS AND EVALUATION OF [11C]M-MPEP AND [11C]M-PEPy, POTENT AND SELECTIVE RADIOLIGANDS FOR METABOTROPIC GLUTAMATE SUBTYPE 5 (mGlu5) RECEPTOR BY POSITRON EMISSION TOMOGRAPHY (PET). M. Yu[*1], X. Wang[1], K. Jokivarsi[1], A. P. Kozikowski[2], A. Brownell[1]. [1]radiology, Massachusetts General Hospital, Harvard Medical School, Boston, MA, United States; [2]Drug Discovery Group, Georgetown University Medical Center, Washington, DC, United States. (650468)

Objectives: We have successfully synthesized two potent and selective PET radioligands, 2-[(3-[11C]methoxyphenyl) ethynyl]-6-methylpyridine ([11C]M-MPEP) and 3-[11C]methoxy-5- [(2-pyridyl)ethyl] pyridine ([11C]M-PEPy), to image mGluR5, which has been found involved in neurodegenerative disorders. **Methods:** [11C]M-MPEP and [11C]M-PEPy were synthesized by the reaction of precursors and [11C]methyl iodide followed by high pressure liquid chromatography (HPLC) purification. The PET imaging studies were performed by using Concord MicroPET system. The displacement experiments were carried out by using a selective mGluR5 antagonist 2-methyl-6-(phenylethynyl)-pyridine (MPEP) at 10 minutes before the administration of [11C]M-MPEP and [11C]M-PEPy at a dose of 5 mg/kg. The plasma radiolabeled metabolites were analyzed by HPLC. **Results:** [11C]M-MPEP and [11C]M-PEPy were successfully prepared within 45 minutes in a yield of over 30-40%, with radiochemical purity of over 97% and specific radioactivity of about 1000 mCi/µmol. PET studies showed that [11C]M-MPEP and [11C]M-PEPy passed the brain blood barrier and accumulated in the olfactory bulb (OB) subsequent to the peak within 5 minutes. From 15-30 minutes, the binding activity of [11C]M-MPEP and [11C]M-MPEP to OB were 9 - 7 and 18 – 14 % activity/i.d. 100ml respectively, while to cortex, striatum and cerebellum remained similar 4–2 % activity/i.d. 100ml. After pretreatment with MPEP, the radioactivy of [11C]M-MPEP and [11C]M-PEPy in OB significantly reduced to 3.1 and 2.1 activity %/i.d. 100 ml at 20 minutes respectively. These Data indicated that the bindings are reversible with high selectivity. HPLC plasma metabolite analysis showed that the unchanged [11C]M-MPEP and [11C]M-PEPy in plasma were 22% and 8.5% respectively at 20 minutes and no lipophilic radiolabeled metabolite was detected. **Conclusions:** [11C]M-MPEP and [11C]M-PEPy could be synthesized and they are binding to olfactory bulb reversibly with high selectivity, they can be used to map the mGluR5 in the brain.
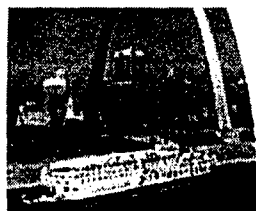
No. 25

CYSTAMINE INDUCED NEUROPROTECTION IN TRANSGENIC R6/2 MOUSE MODEL OF HUNTINGTON'S DISEASE – ASSESSED BY POSITRON EMISSION TOMOGRAPHY (PET) STUDIES.

X. Wang*[1], A. Sarkar[1], M. Yu[1], F. Cicchetti[2], K. Jokivarsi[1], A. Brownell[1]. [1]Radiology, Massachusetts General Hospital, Harvard Medical School, Boston, Massachusetts, United States; [2]Neurosci. unit, CRCHUL, Ste-Foy, PQ, Canada. (650464)

Objectives: Huntington's disease (HD) is an autosomal dominant neurodegenerative disease with no effective treatment and unknown mechanism. However, evidences have been shown the involvement of transglutaminase (TGase) in pathogenesis of Huntington disease. Cystamine, an anti-oxidant, and a competitive inhibitor of transglutaminase, has been found to reduce abnormal movements, decrease body weight loss and prolong the lifespan in R6/2 transgenic mice model of HD. In this study we used PET to investigat the efficacy of cystamine induced neuroprotection. **Methods:** Three groups of R6/2 HD transgenic mice were used in this study, control group, and the groups with cystamine daily i.p. treatment at the dose of 50 and 100 mg/kg respectively. We conducted PET imaging studies of cerebral glucose metabolism with [^{18}F]FDG and striatal dopamine D_2 receptor function with [^{11}C]raclopride using Concord MicroPET system. Each animal was anesthetized for tail vein injection of radiolabeled ligand, and PET data was collected for 60 min and blood glucose is determined from tail vein. **Results:** We found that in untreated R6/2 mice the decrease of glucose metabolism was age dependent with an exponential function after the age of 60 days. The percent decrease of glucose metabolism between 70 to 85 days was 3.87, 3.19 and 3.09 per day in the cortex, striatum and cerebellum correspondingly. In the cystamine treated R6/2 HD mice (at the dose of 50/100 mg/kg) the percent decrease of glucose utilization per day was 1.99/1.22, 1.84/2.38 and 1.74/1.90 in the cortex, striatum and cerebellum, respectively. The binding potential of [^{11}C]raclopride at the age of 74 days in the striatum was 1.07±0.03 in untreated mice and 1.22±0.06 and 1.26±0.08 in cystamine treated mice with doses of 50 and 100 mg/kg, respectively. **Conclusions:** Our findings suggest that cystamine significantly decreases the declining rate of glucose metabolism and improves dopamine D2 receptor function, which might reflect an increased neuronal activity and decreased neuronal loss. These data support that cystamine is a potential neuroprotective drug in the treatment of Huntington disease.

The Third Annual Meeting of **The Society for Molecular Imaging**™ *St. Louis, M(*

September 9-12, 2004

SYNTHESIS AND EVALUATION OF C-11 MPEP, POTENT AND SELECTIVE RADIOLIGAND FOR METABOTROPIC GLUTAMATE SUBTYPE 5 (mGlu5) RECEPTOR BY POSITRON EMISSION TOMOGRAPHY (PET)

Meixiang Yu, PhD, Xukui Wang, MD, Aijun Zhu, PhD, Anna-Liisa Brownell, PhD.
Massachusetts General Hospital, USA.

Objectives: We have successfully synthesized a potent and selective PET radioligand, 2-methyl-6-(phenylethynyl)-pyridine (MPEP), to image mGluR5 receptors.
Methods: [11C]MPEP was synthesized by the reaction of stannyl precursor and [11C]methyl iodide catalyzed by palladium complex, followed by high pressure liquid chromatography (HPLC) purification. The PET imaging studies were performed by using Concord MicroPET system.
Results: [11C]MPEP was successfully prepared within 45 minutes in a yield of over 50%, with radiochemical purity of over 97% and specific radioactivity of about 800 mCi/mmol. PET studies showed that [11C]MPEP passed the brain blood barrier and accumulated in the olfactory bulb (OB), striatum and cerebellum with the maximum activity at 5 to 6 minutes. The binding potentials (% ID/100cc) at 10, 20, 30, 40, 50 and 60 minute after injection were 126.4, 106.3, 87.5, 79.6, 71.8 and 61.4 for Olfactory Bulb, 30.4, 13.0, 11.7, 13.0, 9.4 and 11.6 for striatum, and 23.4, 20.7, 12.8, 11.9, 11.0 and 7.24 for cerebellum, respectively.
Conclusions: [11C]MPEP could be synthesized and it accumulated to olfactory bulb, striatum, and cerebellum reversibly. [11C]MPEP can be used to map the mGluR5 receptors in the brain.

Mapping of brain function after MPTP-induced neurotoxicity in a primate Parkinson's disease model

Anna-Liisa Brownell,[a,d,*] Kelly Canales,[a] Y. Iris Chen,[a] Bruce G. Jenkins,[a] Christopher Owen,[b] Elijahu Livni,[a] Meixiang Yu,[a] Francesca Cicchetti,[d] Rosario Sanchez-Pernaute,[c] and Ole Isacson[c,d]

[a] Department of Radiology, Massachusetts General Hospital, Boston, MA 02114, USA
[b] Department of Neurosurgery, Massachusetts General Hospital, Boston, MA 02114, USA
[c] Department of Neurology, Massachusetts General Hospital, Boston, MA 02114, USA
[d] Udall Parkinson's Disease Research Center of Excellence, Neuroregeneration Laboratory, McLean Hospital, Belmont, MA 02478, USA

Abstract

Neurophysiological studies of the brain in normal and Parkinson's disease (PD) patients have indicated intricate connections for basal ganglia-induced control of signaling into the motor cortex. To investigate if similar mechanisms are controlling function in the primate brain (*Macaca fascicularis*) after MPTP-induced neurotoxicity, we conducted PET studies of cerebral blood flow, oxygen and glucose metabolism, dopamine transporter, and D2 receptor function. Our observations after MPTP-induced dopamine terminal degeneration of the caudate and putamen revealed increased blood flow (15%) in the globus pallidus (GP), while blood flow was moderately decreased (15–25%) in the caudate, putamen, and thalamus and 40 % in the primary motor cortex (PMC). Oxygen extraction fraction was moderately increased (10–20%) in other brain areas but the thalamus, where no change was observable. Oxygen metabolism was increased in the GP and SMA (supplementary motor area including premotor cortex, Fig. 3) by a range of 20–40% and decreased in the putamen and caudate and in the PMC. Glucose metabolism was decreased in the caudate, putamen, thalamus, and PMC (range 35–50%) and enhanced in the GP by 15%. No change was observed in the SMA. In the parkinsonian primate, [^{11}C]CFT (2β-carbomethoxy-3β-(4-fluorophenyltropane) dopamine transporter binding was significantly decreased in the putamen and caudate (range 60–65%). [^{11}C]Raclopride binding of dopamine D$_2$ receptors did not show any significant changes. These experimental results obtained in primate studies of striato-thalamo-cortico circuitry show a similar trend as hypothetized in Parkinson's disease-type degeneration.
© 2003 Elsevier Inc. All rights reserved.

Keywords: Positron emission tomography; Volume rendering; MPTP; Parkinson's disease

Introduction

Parkinson's disease (PD) is characterized neuropathologically by a severe depletion of DA neurons and an associated loss of axons and terminals in the basal ganglia (Kish et al., 1988). Diagnosis is based on clinical signs of

tremor, rigidity, bradykinesia, and postural instability (Marsden, 1992).

Hypotheses of the etiology of PD focus on the potential contribution of environmental toxins (exogenous and/or endogenous) and their interactions with genetic components (Checkoway and Nelson, 1999; Gorrell et al., 1996; Mizuno et al., 1999; Schapira, 1996). Cell death introduced by toxins may trigger a cascade of biological processes with an endpoint of continuous degeneration (Brownell et al., 1998, 1999; Schmidt and Ferger, 2001). These biological processes affect primarily the dopaminergic system in the basal ganglia and the neural network of the motor system (Alex-

* Corresponding author. Department of Radiology, Massachusetts General Hospital, Bartlett Hall 504R, Boston, MA 02114. Fax: +1-617-726-5123.
E-mail address: abrownell@partners.org (A.L. Brownell).

ander et al., 1986, 1990; Wichman and DeLong, 1996; DeLong and Wichman, 2001).

MPTP (1-methyl-4-phenyl-1,2,5,6-tetrahydropyridine) neurotoxicity has long been used as a model for Parkinson's disease because it induces dopaminergic cell death in the substantia nigra pars compacta and striatal dopaminergic degeneration (Palombo et al., 1991; Schmidt and Ferger, 2001). MPTP-induced dopaminergic degeneration causes decreases in the binding of presynaptic dopamine transporters and reduces locomotor activity (Hantraye et al., 1992; Wullner et al., 1994).

A number of in vivo imaging studies in PD patients have shown regional differences in glucose metabolism and blood flow (Brooks, 2001; Eidelberg et al., 1995b; Fukuda et al., 2001; Markus et al., 1995). These studies show that glucose utilization and cerebral blood flow reductions in the brain correlate with the severity of the disease (Berding et al., 2001; Eberling et al., 1994; Eidelberg et al., 1995a; Moeller and Eidelberg, 1997; Imon et al., 1999). Antonini et al. (1998) have even proposed that studies of glucose metabolism can be used for differential diagnosis of PD.

There is, however, great variability in the reports of absolute values of local metabolic functions (Antonini et al., 1995; Bohnen et al., 1999; Eberling et al., 1994). This may originate from methodological differences during imaging studies, variability in the resolution of the imaging devices and, finally, differences in the selection of regions of interest, as well as level of degenerative process. Eidelberg et al. (1996) and Brooks (2001) have used a statistical parametric mapping technique with normalized values to evaluate metabolic changes in different brain areas in PD patients before and after therapeutic regimen. Autoradiographic studies in awake primates (Palombo et al., 1990; Porrino et al., 1987) have shown significant local changes in glucose utilization in basal ganglia, cerebral cortex, and cerebellum after an unilateral intracarotid administration of MPTP.

Based on neurophysiological experiments five different loops have been characterized to control signaling between the basal ganglia and the cortex (Alexander et al., 1990). In PD, the most sensitive loop is between the putamen, globus pallidus, thalamus, and cortex. The motor loop links the supplementary motor area (SMA) to the primary motor cortex, dorsal putamen, pallidum and ventrolateral thalamus, while the dorsolateral prefrontal cortex loop links dorsal caudate and ventroanterior thalamus (Isacson et al., 2001). Studies in PD patients have postulated that the nigrostriatal DA deficiency leads to decreased inhibition of the internal segment of the globus pallidus by both direct and indirect pathways (Alexander et al., 1990). The resulting excessive inhibitory output from the globus pallidus suppresses the ventral thalamus, reducing activation of the supplementary motor area and prefrontal cortex, and creates the motor impairments characteristic of PD (Alexander, 1987; Crutcher and DeLong, 1984; Wichman and DeLong, 1996).

To investigate if similar neural circuitry-linked mecha-

nisms are operating in primate models of parkinsonism induced by MPTP, we conducted experimental imaging studies before and after MPTP of cerebral blood flow, oxygen extraction fraction, oxygen and glucose metabolism, dopamine transporters, and dopamine D_2 receptors using positron emission tomography (PET).

For data analyses, a volumetric technique was developed to select regions of interest based both on a primate brain atlas (Paxinos et al., 2000) and on actual MRI data. PET data were coregistered with the complete brain volume of MR data, and the resulting volumetric-PET data were used for quantitative data analyses.

Methods

Procedures in primates

Five male aged monkeys (*Macaca fascicularis*) (age: 11–16 years) were injected with MPTP (0.3 or 0.5 mg/kg iv weekly) until PD symptoms appeared including hypokinesia, tremor, rigidity, and bradykinesia (Wullner et al., 1994). The total dose of the injected MPTP varied between 25 and 42 mg and the total administration time between 6 and 21 months. PET imaging studies were conducted before MPTP administrations and 2–3 months after cessation of MPTP, when the PD symptoms were stabilized. For the imaging studies, primates were anesthetized using halothane (1.5% with oxygen flow rate of 3 L/min). Arterial and venous catheterization was done for drawing blood samples and injecting of labeled ligands. Animals were adjusted into a stereotactic head holder with ear bars at the origin. Interior orbital supports ensure that images are acquired on a pseudocoronal plane perpendicular to the orbito-meatal line. This allows superposition of the data from MRI studies. Level of anesthesia, blood gases, heartbeat, and vital signs were monitored throughout the imaging procedures (Propaq, Vital Signs Monitor, Protocol Systems. Inc., Beaverton, OR).

Imaging studies of blood flow and oxygen and glucose metabolism were conducted in one imaging session, and studies of dopamine transporters and D_2 receptors were conducted in another session within the time span of a week. The MRI studies, needed for anatomical data, were conducted within a month. This short time span is necessary to eliminate possible errors in volumetric data fusion, raised by neurotoxicity-induced morphologic volumetric changes. MPTP-induced changes in blood flow, oxygen, and glucose metabolism were conducted in four primates and changes in dopamine transporter and receptor function in five primates, correspondingly.

Animals used in this study were maintained according to the guidelines of the Committee on Animals of the Harvard Medical School and Massachusetts General Hospital and of the *Guide for Care and Use of Laboratory Animals* of the Institute of the Laboratory Animal Resources, National Re-

search Council, Department of Health, Education and Welfare, Publication No. (NIH)85-23.

Detection of locomotor activity

Spontaneous locomotor activity was monitored by an Actiwatch system (Mini Mitter Company, Inc., Sunriver, OR) mounted in a shirt pocket in the back of the animal (Puyau et al., 2002). The Actiwatch reader was connected to a computer, and data were transferred from the Actiwatch to a computer through a wireless link. The Actiwatch allows analyses of circadian rhythms, average activity during light and dark, mean activity score, movement, and movement-type index. Prior to MPTP injections, there was a significant difference between day and night time locomotor activities, while after MPTP no activity difference was observable (Fig. 1). Even though the Actiwatch data cannot be used to measure clinical score of PD, it provides a useful follow-up method to visualize daily changes in spontaneous locomotor activity.

MR imaging

MR imaging was conducted in anesthetized primates using the same stereotactic head frame as in the PET studies. T2-weighted images (TR = 4500, TE = 100/10 ms) were acquired with a GE Signa 3.0 T imager in coronal planes using continuous acquisition of 3-mm slices to obtain anatomical information to be used in fusion with PET data to obtain volume of interest for quantitative analyses.

PET imaging

PET imaging studies were conducted with an in-house-built single ring PET device, PCR-I (Brownell et al., 1989). The resolution of PCR-I for a point source at the center is 4.5 mm, and the sensitivity is 46 kHz/μCi for a source of 20 cm in diameter with a concentration of 1 μCi/ml. The overall efficiency is 64% of the theoretical maximum for a 1-cm-plane thickness corresponding to the 2-cm-high detectors. The plane thickness of 5 mm used in this study is obtained by the use of cylindrical collimators, which limit the effective height of the detectors. The resolving time of PCR-I is 6 ns (FWHM). Data acquisition over the whole brain volume with this single ring device was done with 5-mm steps starting from the cerebellar level. Imaging data were corrected for uniformity, sensitivity, attenuation, decay, and acquisition time. PET images were reconstructed using a Hanning filtered convolution backprojection with a cutoff value of 1.0 (Chesler, 1973). Calibration of the positron tomograph was performed prior to each study using a cylindrical plastic phantom (diameter 6 cm) containing water solution of ^{18}F. The corrected reconstructed data set was repacked on the Linux workstation and converted into ANALYZE/AVW image format. The voxel size in coronal

PET images is 5 mm in the axial Z direction and 1.19 mm × 1.19 mm in x-y plane.

After that T2-weighted MRI data from the same subject were loaded and converted into ANALYZE/AVW image format. A segmentation routine in ANALYZE was used to separate the brain from the surrounding tissue in the MRI data. PET data were then thresholded and coregistered to its respective MRI data using the NMI (Normalized Mutual Information) voxel match algorithm of the ANALYZE software package and cubic spline interpolation. A resulting transformation matrix maps the PET images onto its respective MR images, and the multimodality image registration routine returns fused PET-MRI images. The fused PET-MR images were then volume rendered for display (Fig. 2).

Selection of the volume of interest

Three-dimensional regions of interest were outlined on coronal MR slices based on anatomical borderlines observed from the primate brain atlas and MR images (Fig. 3). These regions were also computationally compared and verified with the corresponding slices in the primate brain atlas (Paxinos et al., 2000). The transformation matrix for fusing the PET data to the MRI data was then reapplied to the PET images to generate the data for three- dimensional VOI (volume of interest) analysis. Volumetric radioactivity concentration was calculated for each VOI, and these data were then used for further data analyses to calculate values for blood flow, oxygen extraction fraction and metabolism, glucose metabolism, and binding potential for dopamine transporters and dopamine D$_2$ receptors.

Validation of the volumetric data analyses

To validate the three-dimensional data analyses we conducted studies with a phantom consisting of two concentric spheres (Data Spectrum Corporation, Chapel Hill, NC). The volume of the inner sphere was 20 ml, and the volume of the outer sphere was 79 ml. In the first experiment the outer sphere was filled with ^{18}F-labeled water, and the inner sphere was filled with water without radioactivity. The phantom was scanned stepwise with 5-mm steps (Fig. 4). In the second experiment the inner sphere was filled with higher radioactivity concentration than in the outer sphere, which had the same radioactivity concentration as in the first experiment. Additionally, T2-weighted MR images were done with both concentric spheres filled with water. The data analyses were conducted in the same way as above by drawing ROIs on MR images and then fusing PET data with MRI data. Finally, radioactivity concentration was determined and compared with actual measured radioactivity. For comparison, radioactivity concentration was also calculated based on conventional 2-dimensional pixel analyses (Table 1).

Before MPTP   **After MPTP**

1

2

1. Caudate nucleus   5. Premotor Cortex
2. Putamen   6. Primary Motor Cortex
3. Globus Pallidus   7. Cerebellum
4. Thalamus

3
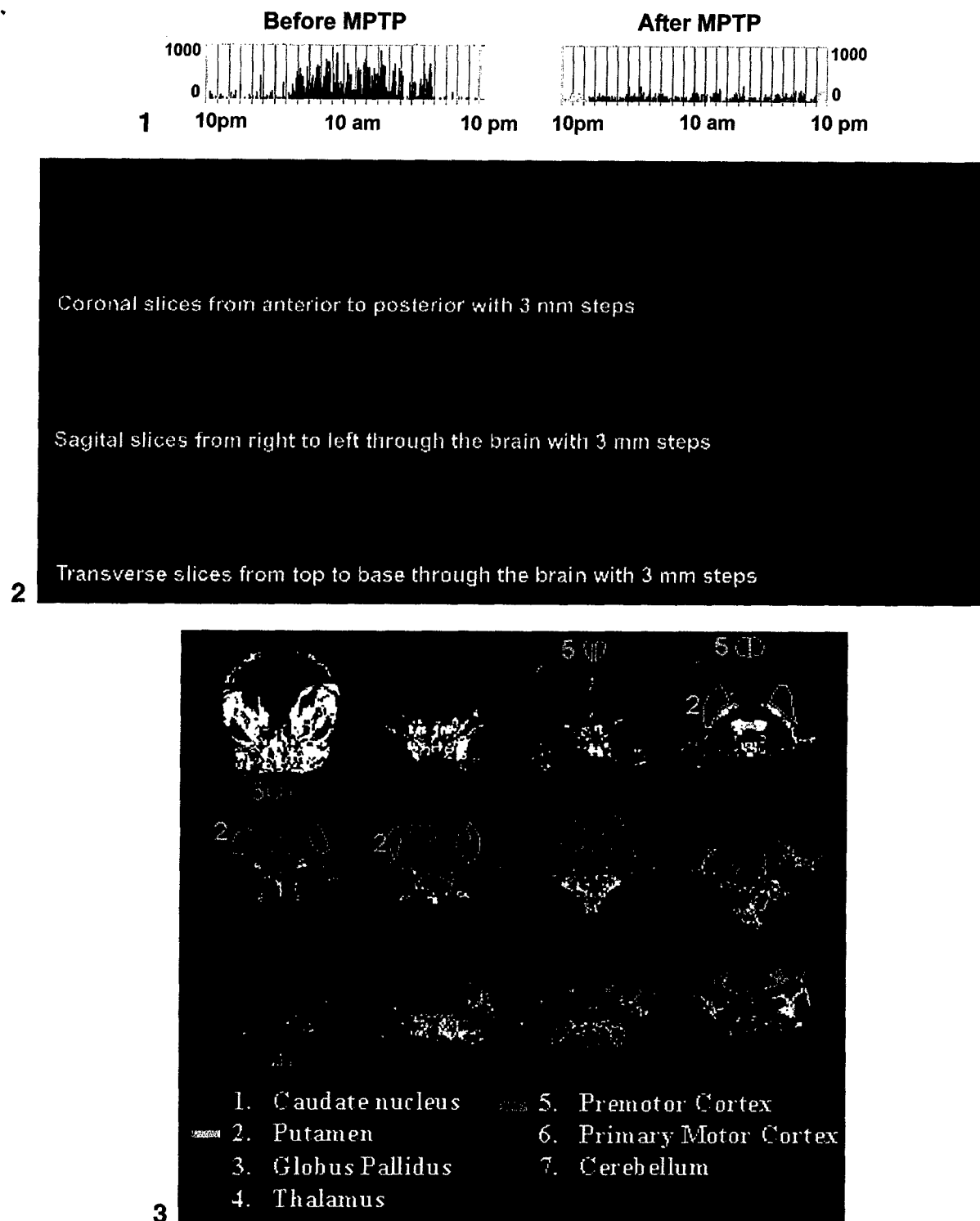
Fig. 1. Effect of MPTP-induced neurotoxicity on spontaneous locomotor activity detected by an Actiwatch before and after MPTP. Before MPTP there was a significant difference between day and night time locomotor activity, while after MPTP no activity difference was observable.

Fig. 2. A PET study of the distribution of [^{11}C]raclopride binding in dopamine D_2 receptors after MPTP toxicity in a primate brain. PET data were fused with volume-rendered MR images. The upper row shows coronal slices from anterior to posterior direction. Binding to D_2 receptors are localized mainly in the putamen and caudate. The middle row shows sagital slices from right to left. Slices 1–7 represent right hemisphere and slices 8–13 left hemisphere. At the bottom row transverse slices are shown from top to base. Volumetric distribution of radioactivity is used in selecting region (volumes) for interest used in quantitative data analyses of receptor function.

Fig. 3. Anatomical borderlines observed from MR images were used to define the regions of interest for volumetric data analysis on the fused PET-MRI data set. Segmented brain areas are numbered and color-coded as shown in the image. The data from the left and right hemispheres were analyzed separately.

Fig. 4. To evaluate the accuracy of the volumetric data reconstruction a phantom consisting of two concentric spheres was imaged by PET. Coronal PET images were acquired with 5-mm steps and slice thickness of 5 mm over the phantom. The middle row shows images, when the outer sphere was filled with ^{18}F-labeled water and the inner sphere with water without radioactivity. The lower row shows images, when the inner sphere was filled with the same radioactivity concentration as above an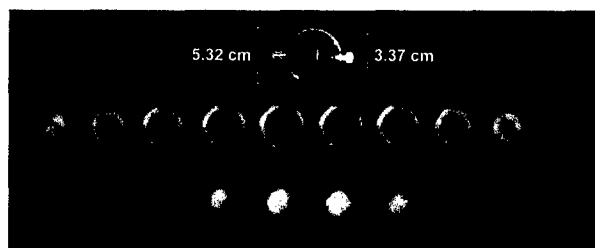d activity concentration in the outer shell was about 44% of it. For data analysis PET images were fused with T2-weighted MR images and radioactivity concentrations in the inner and outer shell were determined (Table 1) using the same volumetric data analysis as in the experimental primate studies.

Blood flow studies

Blood flow studies were conducted using a steady-state technique based on the inhalation of $C^{15}O_2$ (Frackowiak et al., 1980; Jones et al., 1976; Subramanyam et al., 1978). ^{15}O-labeled CO_2 gas mixture was delivered at a constant concentration and flow rate (2 L/min) into the inhalation tube. After 6–8 min of inhalation of $C^{15}O_2$ gas mixture, a steady-state activity level was obtained in the brain, and sequential imaging over the brain was performed starting from the cerebellar level using 5-mm steps and an acquisition time of 60 s. During imaging, a series of arterial blood samples were drawn to determine blood gases and radioactivity in the plasma and whole blood. These data are needed for calculation of the oxygen extraction level (Subramanyam et al., 1978). Radioactivity was measured in a gammacounter (Packard Cobra Auto-gamma, Downers, IL), which was cross-calibrated with the tomograph. Arterial blood and plasma radioactivity concentrations were then computed after corrections for dead time and decay.

Fig. 5. Coronal midbrain slices of a monkey brain illustrate the quantitative distribution of hemodynamic, metabolic, and dopamine receptor function before and after MPTP neurotoxicity. Studies of blood flow were conducted with a steady-state inhalation technique using a $C^{15}O_2$ gas mixture (Jones, 1976). Studies of oxygen metabolism were conducted with a steady-state inhalation technique using a $^{15}O_2$ gas mixture (Jones, 1976; Subramanyam, 1978). Studies of glucose metabolism were conducted with [18F]FDG (2-^{18}F-fluoro-2-deoxy-D-glucose). Studies of dopamine transporters were conducted with [11C]CFT (2β-carbomethoxy-3β-(4-fluorophenyltropane). Studies of dopamine D_2 receptors were conducted with [11C]raclopride.

Table 1
Radioactivity based on the volumetric data analyses compared to the measured radioactivity and the conventional 2-dimensional pixel analyses in two concentric spheres

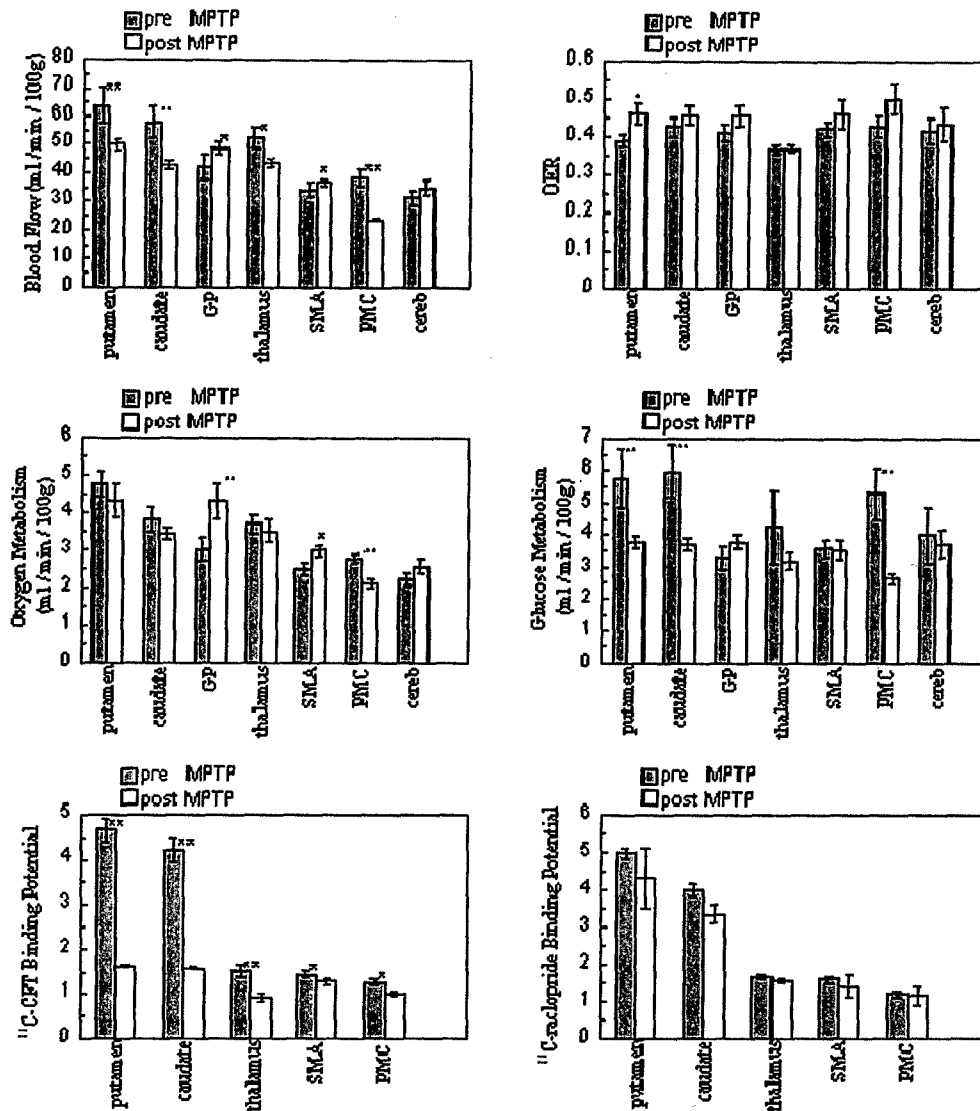|	Inner sphere (μCi/100 ml)	Outer sphere (μCi/100 ml)
First experiment		
Radioactivity determined on the volumetric data analyses	86 +/− 7	893 +/− 62
Measured radioactivity	0	869 +/− 11
Conventional 2D ROI analyses	110 +/− 12	1012 +/− 94
Second experiment		
Radioactivity determined on the volumetric data analyses	527 +/− 20	239 +/− 7
Measured radioactivity	516 +/− 5	225 +/− 4
Conventional 2D ROI analyses	572 +/− 72	275 +/− 55

Fig. 6. Quantitative topographic distribution (mean +/− SEM) of hemodynamic, metabolic, and dopamine receptor function before and after MPTP-induced neurotoxicity in the different brain areas. All the data analyses are based on volumetric data analyses using fused PET and MR images. Significant difference was calculated as compared to the pre-MPTP values by using Dunnett's t test. Blood flow studies show a significant decrease in putamen, caudate, and PMC ($P < 0.01$) and thalamus ($P < 0.05$) and an increase in GP and SMA ($P < 0.05$). Oxygen extraction fraction (OER) shows an overall increase with significant change in putamen ($P < 0.05$). Oxygen metabolism shows a significant increase in the GP ($P < 0.01$) and SMA ($P < 0.05$) and a significant decrease in PMC ($P < 0.01$) and an overall decrease in the other brain areas. Glucose metabolism shows a significant decrease in putamen, caudate, and PMC ($P < 0.01$) and an overall decrease in the other brain areas but GP and SMA. Dopamine transporter binding investigated by [11C]CFT shows significant decrease in putamen, caudate, and thalamus ($P < 0.01$) and SMA and PMC ($P < 0.05$). Dopamine D_2 receptor binding investigated by [11C]raclopride does not show any significant changes.

Studies of oxygen extraction fraction and metabolism

After the blood flow study, the inhalation gas mixture was switched to $^{15}O_2$. In 10–12 min a steady-state activity level was obtained in the brain based on stabilized oxygen metabolism and blood flow (Jones et al., 1976; Subramanyam et al., 1978). A similar sequential imaging over the whole brain was performed as above. During imaging arterial blood was drawn to determine blood gases, hematocrite, hemoglobin, and radioactivity levels in the plasma and whole blood. These data are necessary to calculate the oxygen extraction fraction (Jones, 1976;

Subramanyam et al., 1978). Regional cerebral oxygen metabolism can be calculated when blood flow, oxygen extraction fraction, blood gases, and hemoglobin are known (Subramanyam et al., 1978). Finally, values of oxygen metabolic rate were converted to molar units for stoichiometric comparisons with glucose utilization.

Studies of glucose metabolism

Studies of glucose metabolism were done using [18F]FDG (2-18F-fluoro-2-deoxy-D-glucose) as a tracer. FDG distributes in tissue like glucose but remains unme-

Table 2
Stoichiometry of glucose utilization and O_2 consumption in different brain areas before and after MPTP

	Before MPTP	After MPTP
Putamen	6.68 +/− 1.06	8.71 +/− 0.86
Caudate	5.13 +/− 0.69	6.92 +/− 0.34
GP	7.39 +/− 0.78	8.23 +/− 0.92
Thalamus	6.98 +/− 1.91	7.71 +/− 0.71
SMA	5.63 +/− 0.89	5.84 +/− 0.32
PMC	4.19 +/− 0.53	6.00 +/− 0.54
Cerebellum	4.42 +/− 0.98	5.04 +/− 0.38

tabolized in the form of 6-phosphate making quantitative imaging studies possible. The kinetic model of Sokoloff et al. (1977) extended by Phelps et al. (1979) was used in data analysis. Following a rapid intravenous injection of 5 mCi of ^{18}F-FDG, dynamic PET images were acquired at a level 15 mm anterior from the earbar for 30 min using an acquisition time of 15 s. After this, when activity had reached a steady-state level, coronal slices were acquired over the brain at 5-mm steps starting from the cerebellar level and an acquisition time of 60 s. Arterial blood samples were drawn for determination of plasma radioactivity. The plasma data were fitted to a 2-exponential function and used as an input function in calculating glucose metabolic rate. In addition, arterial glucose values were determined before and after the experiment. Values for the transport parameters k_1–k_4 were calculated from the dynamic tissue data using plasma input function (Phelps et al., 1979). Values for regional cerebral glucose metabolism were calculated using transport parameters and blood data information, regional tissue data from the areas of interest and a value of 0.5 for the lumped constant (Reivich et al., 1985). Finally, the values of glucose metabolic rate were converted to molar units for stoichiometric comparison with O_2 consumption.

Studies of dopamine D_2 receptors and transporters

Each study included two experiments. The first experiment was carried out with [^{11}C]raclopride to investigate dopamine D_2 receptors, and the second experiment was conducted 2–3 h later with [^{11}C]CFT (2β-carbomethoxy-3β-(4-fluorophenyltropane) in order to investigate dopamine transporters. Radiolabeled ligand, [^{11}C]raclopride (Ehrin et al., 1985) or [^{11}C]CFT (Brownell et al., 1996) (6–8 mCi, specific activity 600–1000 mCi/μmol) was injected into the femoral vein; and imaging data were acquired stepwise on seven coronal brain levels, initially using 15 s per image. The acquisition time was subsequently increased to 60 s, the total imaging time being 90 min in both experiments. Eighteen arterial blood samples of 0.1 ml were drawn at different time points starting from 10 s frequency and ending with 15 min frequency in order to monitor the decrease in radioactivity. In addition, three arterial blood samples were drawn for HPLC analyses of metabolites of the labeled ligands.

Kinetic behavior of [^{11}C]CFT was studied with a four-parameter estimation of the three-compartmental model approach. In the three-compartmental model, the first compartment is the plasma pool, the second is the exchangeable tracer pool including free and nonspecifically bound ligand in the brain, and the third compartment is a trapped tracer pool including bound ligand in the brain. The exchangeable tracer pool contains ligand but no receptors; and the third compartment includes all the receptors, partly or totally occupied by ligands. The kinetic parameters k_3 and k_4 describe the binding to and dissociation from the receptors.

The transfer coefficients k_1–k_4 were mathematically resolved using a least-square fit, Levenburg-Marquardt method. All numerical analyses were done with the optimization tool SAAM II (Foster et al., 1994). For stabilization of the k values the fitting procedure was performed using two steps. Since the cerebellum does not have specific receptor binding or is negligible, fitting was done with the cerebellar data, letting all the k values float. The ratio k_1/k_2 was then calculated. In further iterations this fixed ratio was used as a constraint and applied with a sequential quadratic programming method combined with a cost function to reach parameter optimization. Regional binding potential was calculated as a ratio of k_3/k_4 (the ratio of the transport from the exchangeable tracer pool into the bound tracer pool to the transport from the bound tracer pool back into the exchangeable tracer pool). Regional binding potentials were

Table 3
MPTP-induced changes in dopamine receptor function, hemodynamics, and metabolism in different brain areas

	Dopamine transporter	Dopamine D_2 receptor	Blood flow	Oxygen extraction	Oxygen metabolism	Glucose metabolism
Putamen	↓**	↓	↓**	↑*	↓	↓**
Caudate	↓**	↓	↓**	↑	↓**	↓**
GP	—	—	↑*	↑	↑**	↑
Thalamus	↓**	↕	↓*	↕	↓	↕
SMA	↓*	↓	↑*	↑	↑*	↕
PMC	↓*	↕	↓**	↑	↓**	↓**
Cerebellum	—	—	↑	↑	↑	↓

↑ indicates an increase, ↓ indicates a decrease and ↕ indicates no change compared to the pre-MPTP value.
* signs $P < 0.05$ and ** $P < 0.01$.

calculated separately for left and right caudate, putamen, thalamus, SMA, and PMC.

Results

Accuracy of the volumetric data analyses

Development of image fusion and volumetric data analysis has been an essential part of this work. This approach is absolutely necessary to obtain reliable data from small brain regions. Fig. 2 shows coronal, transverse, and sagittal segmentation with 3-mm steps (slice thickness) of a volume-rendered MR images fused with PET images of dopamine D_2 receptor distribution after MPTP. The original PET images were acquired with 5-mm steps and a slice thickness of 5 mm. Fig. 3 demonstrates selection of the regions of interest on a single slice level.

The validation of the volumetric data analyses was done with a phantom of concentric spheres (Fig. 4). Table 1 shows the accuracy of the obtained results based on the volumetric data analyses and actual measurement of radioactivity, with comparison to the conventional 2-dimensional pixel analyses. In the first experiment radioactivity was only in the outer sphere and the calculated radioactivity using volumetric data analyses was 3% and with conventional 2D pixel analyses 16% higher that the measured radioactivity. There was only water in the inner sphere, but because of the scatter and spillover of the radioactivity in the outer sphere it was possible to record an activity, which corresponded 9.7% of the activity in the outer sphere using volumetric data analyses and 10.9% using 2D analyses.

In the second experiment radioactivity was in both spheres with the inner sphere more active. The values calculated using volumetric data analyses were 2–6 % higher than measured radioactivity while conventional 2D pixel analyses gave 11–22% higher values. The activity concentration in the inner sphere was in the same range as the striatal activity concentration in blood flow and receptor studies before MPTP toxication. These phantom studies were not corrected for the partial volume effects, because in each slice the smallest thickness of the sphere in the image was equal or bigger than two times the resolution element of the tomograph (Hoffman et al., 1979).

These basic tools have been used to analyze data for blood flow, oxygen extraction fraction, and metabolism as well as glucose metabolism and binding parameters for dopamine transporters and dopamine D_2 receptors in different brain regions.

Hemodynamics and cerebral energy metabolism

Fig. 5 (see Table 3) shows the quantitative distribution and calculated values of blood flow, oxygen metabolism, glucose metabolism, dopamine transporters, and dopamine D_2 receptors at one midbrain level before and after MPTP.

From these images it can be observed, that the most striking change after MPTP is the decrease in striatal dopamine transporter binding. Fig. 6 shows the calculated values obtained by volumetric data analyses in different brain areas of hemodynamic, metabolic, and dopamine receptor function both before and after MPTP induced neurotoxicity.

The largest decrease in blood flow after MPTP was observed in the primary motor cortex (39+/−4%). Blood flow was decreased in the striatal area (caudate and putamen) by 22–26%, and in the thalamus by 17+/−3%. In the globus pallidus, blood flow was increased by 15+/−3% and in the SMA by 4+/−1%.

After MPTP, oxygen extraction fraction was moderately enhanced in other brain areas but the thalamus (Fig. 6). Values for oxygen metabolism in the GP and SMA were significantly elevated, partly being a reflection of elevated oxygen extraction fraction. Oxygen metabolism was decreased in the putamen and caudate by 10+/−2% and significantly in the PMC (23+/−2%).

Glucose metabolism was decreased in all other brain areas but the GP (Fig. 6). In the striatal area glucose utilization was decreased by 35+−/17% in the caudate, 38+/−8% in the putamen, 25+/−7% in the thalamus, and (50+/−12%) in the PMC. Glucose utilization was enhanced in the GP by 15+/−3% (see Table 3).

Stoichiometry of glucose utilization and O_2 consumption

Table 2 shows the calculated values for stoichiometric balance in different brain areas before and after MPTP. The stoichiometric balance increased in all brain areas after MPTP, indicating that, in addition to glucose, other substrates were also metabolized after MPTP.

Dopamine transporters and receptors

The binding of [^{11}C]CFT was significantly decreased in the putamen (65+/−4%), caudate (62+/−5%), thalamus (39+/−4%), SMA (25+/−2%), and PMC (25+/−2%) (Figs. 5 and 6), indicating degeneration of the dopamine transporter sites in the presynaptic terminals. [^{11}C] Raclopride binding in dopamine D_2 receptors showed overall decreases (Figs. 5 and 6, Table 3). However, because of a large variation in the results there was no significant change in raclopride binding after MPTP.

Studies of receptor function and metabolism in relation to neural circuitry

To compare the obtained experimental results of dopamine receptor function, hemodynamics, and metabolism with the known neural circuitry, we analyzed MPTP neurotoxicity-induced changes in different brain areas, conventionally included in neurophysiological studies of the neural networks. Table 3 shows the direction of MPTP-induced significant changes in different brain areas.

Discussion

Parkinson's disease is characterized neuropathologically by a severe depletion of dopamine neurons in the basal ganglia. Our experiments, conducted in primates after MPTP-induced neurotoxicity, showed significantly decreased binding of [11C] CFT in striatum, indicating depletion of presynaptic dopamine terminals. We have published this observation in 1992 (Hantraye et al., 1992), and in 1994 we further demonstrated the correlation to locomotor activity (Wullner et al., 1994). In these experiments we also found that the total dose or injection period of MPTP does not correlate with locomotor activity or clinical scores (Wullner et al., 1994). Since then, about 200 papers have been published, with a unanimous observation of declining dopamine transporter binding (van Dyck et al., 2002; Antonini et al., 2001; Chouker et al., 2001; Huang et al., 2001; Marck et al., 2001; Sakakibara et al., 2001). Even though there is an unequivocal decline in presynaptic dopamine transporter binding in PD, there is inconsistency in reported results of [11C]raclopride binding in dopamine D_2 receptors in PD (Doudet et al., 2000; Hwang et al., 2002; Kaasinen et al., 2000). In our present experiments, we have found a tendency for a decrease but with a large variation in dopamine D_2 receptor binding after MPTP toxication. During MPTP administration (acute MPTP-induced neurotoxicity) and after 6-hydroxydopamine toxicity (van Nguyen et al., 2000) we have observed a moderately increased [11C]raclopride binding in D_2 receptors. Altogether, our observations of dopamine D_2 receptor binding are consistent with a number of publications that propose a biphasic behavior of D_2 receptor binding; indicating that in the early phase of Parkinson's disease, D_2 receptor binding is enhanced because of supersensitivity and it will decline later with progression of the disease (Stoessl and de la Fuentes-Fernandez, 2003; Hwang et al., 2002; Kaasinen et al., 2000). In addition, there are some other aspects, which might effect on [11C]raclopride binding. First, it has low binding affinity, and it is impossible to determine whether the changes in binding reflect alterations in the number of available dopamine receptors or whether they are due to changes in synaptic dopamine concentration (Stoessl and de la Fuente-Fernandez, 2003). In addition, it may be possible that these effects could cancel each other out.

By using the volume of interest determined from the fusion with MR images we were able to investigate also binding characteristics of [11C]CFT and [11C]raclopride in the thalamus, SMA, and PMC. Using conventional PET image analysis it is impossible to localize these sites because the accumulation of radioactivity is so low compared to striatal accumulation. The binding values obtained (Figs. 5 and 6) correlate well with the values obtained using autoradiographic techniques (Kaufman and Madras, 1992).

In addition to studies of dopamine transporters and dopamine D_2 receptors, we conducted hemodynamic and metabolic studies in this preclinical model of PD with the ultimate aim of finding parallels to human PD in adaptive changes including metabolic neural networks and dopaminergic function.

Brooks (1997, 1999) has shown that slowness in free performed motion in PD patients corresponds with changes in blood flow in the supplementary motor area and dorsal prefrontal cortex, areas which get subcortical input from the basal ganglia. Notably, blood flow changes consistent with a compensatory overactivation in premotor area were observed. In PD, there appears to be a synchronization of GPe and GPi output signals as a result of the loss of DA tonic input to the putamen; that together with a reduced thalamic input to the SMA and PM cortices may explain the motor signs of PD (Brooks, 1999; Eidelberg et al., 1995b; Schmidt and Ferger, 2001). Moreover, the recruitment of more cortical regions and the increased and widespread activation of PM and SMA-associated cortices suggest that these structures are compensating for the abnormal input, to be able to activate the motor cortex for initiation of the movement (Brooks, 1997; Eidelberg et al., 1996).

We observed enhanced blood flow in the supplementary motor area as well as in the globus pallidus, while blood flow was decreased in the putamen, caudate, and primary motor cortex of the parkinsonian primate. Oxygen metabolism was marginally enhanced in the globus pallidus and supplementary motor area and decreased in the putamen, caudate, and primary motor cortex. Glucose metabolism was decreased in all brain areas after MPTP but the GP and SMA. In short, we found (1) a decreased striatal dopamine transporter binding, indicating degeneration of presynaptic terminals; (2) an increased blood flow in the globus pallidus, indicating activation in that brain area; (3) a decreased glucose metabolism in the thalamus, indicating decreased energy metabolism; and (4) decreased blood flow and glucose metabolism in the PMC, indicating decreased motor activity. However, at the same time, blood flow in the SMA was increased while no change in glucose metabolism was observed indicating a compensatory mechanism in motor function. These observations (see Table 3) support a neural circuitry-based reasoning for changes seen in functional interactions of the motor system in human parkinsonism (Wichman and DeLong, 2003; Carbon et al., 2003; DeLong and Wichman, 2001; Isacson et al., 2001).

As a comparison of the values obtained for the regional changes of glucose utilization in this "chronic" MPTP model it can be emphasized that Palombo et al. (1991) obtained 40% enhanced glucose utilization in a globus pallidus by autoradiographic studies of [14C]deoxyglucose in a hemiparkinsonian model induced by a unilateral intracarotid administration of MPTP into the striatum. As well Porrino et al. (1987) found a significantly reduced glucose utilization in substantia nigra, thalamus, and ventral tegmental area and increased values in globus pallidus by autoradiographic studies of [14C]deoxyglucose in MPTP-treated awake primates. Eidelberg et al. (1994) found in human Parkinson's disease patients a 20–30% average decrease in

glucose utilization depending on the level of disease. It is obvious that there is a difference in absolute values between animal models and species. However, interestingly the trend of the changes is similar.

We have considered the globus pallidus as one brain region in these experiments. However, it has two parts interna and externa, which have different functions. The observed increase in hemodynamic functions, blood flow and oxygen and glucose metabolism, in the GP area could reflect (1) an increased firing of GPi neurons (which project to the thalamus), (2) an increased metabolism at synaptic terminals from GPe and putamen, projecting to GPi, or (3) a metabolic activity of interneurons of GP. Differentiation of these mechanisms is not possible with the conducted PET techniques, but requires additional electrophysiological measurements.

In the normal in vivo state, glucose is the only substrate for energy metabolism in the brain. Under normal circumstances, no other potential energy yielding substrate has been found to be extracted from the blood in more than trivial amounts. For complete oxidation of glucose, the theoretical ratio of O_2 to glucose utilization is 6.0. A value of 5.2 has been obtained in human studies conducted with $^{15}O_2$ gas and [^{18}F]FDG (Frey, 1999). In the present experiments, an average value for the stoichiometry of the glucose utilization and oxygen consumption is 5.8+/− 0.6 before MPTP regimen and 7.0+/−0.9 after MPTP calculated as a mean of 8 investigated brain areas (see Table 2). An average 20% increase in oxygen consumption compared to glucose utilization after MPTP may be explained by a reduced mitochondrial function or combined effect of decreased metabolism and anesthesia. Halothane anesthesia might have an enhancing effect on the absolute values of blood flow and metabolism depending on the level of halothane concentration. The effect is, however, smaller in the spontaneous inhalation used in these experiments (Amory et al., 1971). In addition, the same anesthesia protocol was used before and after MPTP so the possible anesthesia-induced changes were minimized in the evaluation of MPTP-induced changes on blood flow, metabolism, and dopaminergic function.

To obtain quantitative information from small brain areas in imaging studies, we have developed a volumetric technique for data analyses and used fused PET and MRI data. In addition, the primate brain atlas was utilized to outline the regions of interest on MR images. Even when the selection of the volume of interest is accurate on a technical level, there is a potential error in the absolute values because of effects of partial volume (Hoffman et al., 1979). In addition, outlining tiny brain areas there is a personal factor. When these data were analyzed by two scientists independently, there was an average of 20% difference between the absolute values, they obtained. However, when they analyzed the data together, the values were equal to the lower values in the first time. Moreover, in the absolute values internal scatter radiation is a factor in nearby low activity

tissue if the neighboring tissue has a high activity concentration. In biological studies this shows up especially in the [^{11}C]CFT studies of dopamine transporters, where the putamen has a high activity accumulation compared to the nearby tissues (Fig. 5). To validate volumetric data analyses, imaging studies in concentric sphere phantoms were conducted. The absolute values calculated for radioactivity concentration were higher than measured radioactivity mainly because of the internal scatter. This is clearly demonstrated in the first phantom study when the inner sphere did not have any radioactivity but based on data acquisition and analyses it had about 10% of the activity of the outer sphere (Table 1).

These experiments provide in-depth information on changes in metabolic and dopaminergic function in neural networks after MPTP-induced parkinsonism in primates. This information is valuable for investigations of a compensatory mechanism during degeneration and structural repair. In addition, these experiments enhance the use of MPTP neurotoxicity as a model to investigate human Parkinson's disease.

Acknowledgments

References

Alexander, G., 1987. Selective neuronal discharge in monkey putamen reflects intended direction of planned limb movement. Exp. Brain Res. 67, 623–634.

Alexander, G., DeLong, M.R., Strick, P.L., 1986. Parallel organization of functionally segregated circuits linking basal ganglia and cortex. Annu. Rev. Neurosci. 9, 357–381.

Alexander, G.E., Crutcher, M.D., Delong, M.R., 1990. Basal ganglia thalamo-cortical circuits: parallel substrates for motor, oculomotor, "prefrontal" and "limbic" functions. Prog. Brain Res. 85, 119–146.

Amory, D.W., Steffenson, J.L., Forsyth, R.P., 1971. Systemic and regional blood flow changes during halothane anesthesia in the Rhesus monkey. Anesthesiology 35, 81–90.

Antonini, A., Kazumata, K., Feigin, A., Mandel, F., Dhawan, V., Margouleff, C., et al., 1998. Differential diagnosis of parkinsonism with [^{18}F]fluorodeoxyglucose and PET. Mov. Disord. 13, 268–274.

Antonini, A., Moresco, R.M., Gobbo, C., De Notaris, R., Panzacchi, A., Barone, P., et al., 2001. The status of dopamine nerve terminals in Parkinson's disease and essential tremor: a PET study with the tracer [^{11}C]FE-CIT. Neurol. Sci. 22, 47–48.

Antonini, A., Vontobel, P., Psylla, M., Gunther, I., Maguire, P.R., Missimer, J., et al., 1995. Complementary positron emission tomographic studies of the striatal dopaminergic system in Parkinson's disease. Arch. Neurol. 52, 1183–1190.

Berding, G., Odin, P., Brooks, D.J., Nikkhah, G., Matthies, C., Peschel, T., et al., 2001. Resting regional cerebral glucose metabolism in advanced Parkinson's disease studied in the off and on conditions with [^{18}F]FDG-PET. Mov. Disord. 16, 1014–1022.

Bohnen, N., Minoshima, S., Giordani, B., Frey, K.A., Kuhl, D.E., 1999. Motor correlates of occipital glucose hypometabolism in Parkinson's disease without dementia. Neurology 52, 541–546.

Brooks, D., 1997. PET and SPECT studies in Parkinson's disease. Baillieres Clin. Neurol. 6, 69–87.

Brooks, D., 1999. Functional imaging of Parkinson's disease: is it possible to detect brain areas for specific symptoms? J. Neural. Transm. Suppl. 56, 139–153.

Brooks, D.J., 2001. Cerebral blood flow activation studies, in: Calne, D., Calne, S. (Eds.), Parkinson's Disease: Advances in Neurology, Vol. 86. Lippincott Williams & Wilkins, Philadelphia, pp. 225–235.

Brownell, A.-L., Elmaleh, D.E., Meltzer, P.C., Shoup, T.M., Brownell, G.L., Fischman, A.J., et al., 1996. Cocaine congeners as PET imaging probes for dopamine terminals. J. Nucl. Med. 37, 1186–1192.

Brownell, A.-L., Jenkins, B.G., Elmaleh, D.R., Deacon, T.W., Spealman, R.D., Isacson, O., 1998. Combined PET/MRS brain studies show dynamic and long-term physiological changes in a primate model of Parkinson disease. Nature Med. 4, 1308–1312.

Brownell, A.-L., Jenkins, B.G., Isacson, O., 1999. Dopamine imaging markers and predictive mathematical models for progressive degeneration in Parkinson's disease. Biomed. Pharmacother. 53, 131–140.

Brownell, G.L., Burnham, C.A., Stearns, C.W., Chesler, D.A., Brownell, A.-L., Palmer, M., 1989. Development in high-resolution positron emission tomography at MGH. Int. J. Imaging Systems Technol. 1, 207–217.

Carbon, M., Edwards, C., Eidelberg, D., 2003. Functional brain imaging in Parkinson's disease, in: Gordin, A., Kaakkola, S., Teravainen, H. (Eds.), Parkinson's Disease: Advances in Neurology, vol. 91. Lippincott Williams & Wilkins, Philadelphia, pp. 175–181.

Checkoway, H., Nelson, L.M., 1999. Epidemiologic approaches to the study of Parkinson's disease etiology. Epidemiology 10, 327–336.

Chesler, D., 1973. Positron tomography and three-dimensional reconstruction technique, in: Freedman, G.S. (Ed.), Tomographic Imaging in Nuclear Medicine. Soc. Nucl. Med., New York, pp. 176–183.

Chouker, M., Tatsch, K., Linke, R., Pogarell, O., Hahn, K., Schwarz, J., 2001. Striatal dopamine transporter binding in early to moderately advanced Parkinson's disease: monitoring of disease progression over 2 years. Nucl. Med. Commun. 22, 721–725.

Crutcher, M., DeLong, M.R., 1984. Single cell studies of the primate putamen. II. Relations to direction of movement and pattern of muscular activity. Exp. Brain Res. 53, 244–258.

DeLong, M., Wichman, T., 2001. Deep brain stimulation for Parkinson's disease. Ann. Neurol. 49, 142–143.

Doudet, D.J., Holden, J.E., Jivan, S., McGeer, E., Wyatt, R.J., 2000. In vivo PET studies of the dopamine D2 receptors in rhesus monkeys with long term MPTP-induced parkinsonism. Synapse 38, 105–113.

Eberling, J., Richardson, B.C., Reed, B.R., Wolfe, N., Jagust, W.J., 1994. Cortical glucose metabolism in Parkinson's disease without dementia. Neurobiol. Aging 15, 329–335.

Ehrin, E., Farde, L., de Paulis, T., Eriksson, L., Greitz, T., Johnstrom, P., et al., 1985. Preparation of ^{11}C-labelled raclopride, a new potent dopamine receptor antagonist: preliminary PET studies of cerebral dopamine receptors in the monkey. Int. J. Appl. Radiat. Isot. 36, 269–273.

Eidelberg, D., Moeller, J.R., Dhawan, V., Spetsieris, P., Takikawa, S., Ishikawa, T., et al., 1994. The metabolic topography of parkinsonism. J. Cereb. Blood Flow Metab. 14, 783–801.

Eidelberg, D., Moeller, J.R., Ishikawa, T., Dhawan, V., Spetsieres, P., Chaly, T., et al., 1995a. Assessment of disease severity in parkinsonism with fluorine-18-fluorodeoxyglucose and PET. J. Nucl. Med. 36, 378–383.

Eidelberg, D., Moeller, J.R., Ishikawa, T., Dhawan, V., Spetsieres, P., Chaly, T., et al., 1995b. Early differential diagnosis of Parkinson's disease with 18F-fluorodeoxyglucose and positron emission tomography. Neurology 45, 1995–2004.

Eidelberg, D., Moeller, J.R., Ishikawa, T., Dhawan, V., Spetsieres, P., Silbersweig, D., et al., 1996. Regional metabolic correlates of surgical outcome following unilateral pallidotomy for Parkinson's disease. Ann. Neurol. 39, 452–459.

Foster, D., Barrett, P.H.R., Bell, B.M., Beltz, W.F., Cibelli, C., Golde. H.1994. Simulation, analysis and modeling software. BMES Bull., 18.

Frackowiak, R., Lenzi, G.L., Jones, T., Heather, J.D., 1980. Quantitative measurement of regional cerebral blood flow and oxygen metabolism in man using 15O and positron emission tomography: theory, procedure and normal values. J. Comput. Assist. Tomogr. 4, 727–736.

Frey, K.A., 1999. Positron emission tomography, in: Siegel, G.J., Agranoff, B.W., Albers, R.W., Fisher, S.K., Uhler, M.D. (Eds.), Basic neurochemistry. Lippincott-Raven, Philadelphia, pp. 1109–1131.

Fukuda, M., Mentis, M.J., Ma, Y., Dhawan, V., Antonini, A., Lang, A.E., et al., 2001. Networks mediating the clinical effects of pallidal brain stimulation for Parkinson's disease. A PET study of resting-state glucose metabolism. Brain 124, 1601–1609.

Gorrell, J., DiMonte, D., Graham, D., 1996. The role of environment in Parkinson's disease. Environ. Health Perspect. 104, 652–654.

Hantraye, P., Brownell, A.-L., Elmaleh, D.R., Spealman, R.D., Wullner, U., Brownell, G.L., et al., 1992. Dopamine fiber detection by [11C]-CFT and PET in a primate model of parkinsonism. NeuroReport 3, 265–268.

Hoffman, E.J., Huang, S.C., Phelps, M.E., 1979. Quantitation in positron emission tomography. 1 Effect of object size. J. Comput. Assist. Tomogr. 3, 299–308.

Huang, H.S., Lin, C.Z., Lin, J.C., Wey, S.P., Ting, G., Liu, R.S., 2001. Evaluation of early-stage Parkinson's disease with 99mTc-TRODAT-1 imaging. J. Nucl. Med. 42, 1303–1308.

Hwang, W.J., Yao, W.J., Wey, S.P., Shen, L.H., Ting, G., 2002. Down-regulation of striatal dopamine D2 receptors in advanced Parkinson's disease contributes to the development of motor flunctuation. Eur. Neurol. 47, 113–117.

Imon, Y., Matsuda, H., Ogawa, M., Kogure, D., Sunohara, N., 1999. SPECT image analysis using statistical parametric mapping in patients with Parkinson's disease. J. Nucl. Med. 40, 1583–1589.

Isacson, O., van Horne, C., Schumacher, J.M., Brownell, A.-L., 2001. Improved surgical cell therapy in Parkinson's disease—physiological basis and new transplantation methodology, in: Calne, D., Calne, S. (Eds.), Parkinson's Disease: Advances in Neurology, Vol. 86. Lippincott Williams & Wilkins, Philadelphia, pp. 447–454.

Jones, T., Chesler, D.A., Ter-Pogossian, M.M., 1976. The continuous inhalation ofxygen-15 for assessing regional oxygen extraction fraction in the brain of man. Br. J. Radiol. 49, 339–343.

Kaasinen, V., Ruottinen, H.M., Nagren, K., Lehikoinen, P., Oikonen, V., Rinne, J.O., 2000. Upregulation of putaminal D2 receptors in early Parkinson's disease: a comparative PET study with [^{11}C]raclopride and [^{11}C]N-methylspiperoni. J. Nucl. Med. 41, 65–70.

Kaufman, M.J., Madras, B.K., 1992. Distribution of cocaine recognition sites in monkey brain. II.Ex vivo autoradiography with [^{3}H]CFT and [^{125}I]RTI-55. Synapse 12, 99–111.

Kish, S., Shannak, K., Hornykiewicz, O., 1988. Uneven pattern of dopamine loss in the striatum of patients with idiopathic Parkinson's disease. N. Engl. J. Med. 318, 876–880.

Marck, K., Innis, R., van Dyck, C., Fussel, B., Early, M., Eberly, S., et al., 2001. [^{123}I]Beta-CIT SPECT imaging assessment of the rate of Parkinson's disease progression. Neurology 57, 2089–2094.

Markus, H., Lees, A.J., Lennox, G., Marsden, C.D., Costa, D.C., 1995. Patterns of regional cerebral blood flow in corticobasal degeneration studied using HMPAO SPECT; comparison with Parkinson's disease and normal controls. Mov. Disord. 10, 179–187.

Marsden, C.D., 1992. Parkinson disease. Postgrad. Med. J. 68, 538–543.

Mizuno, Y., Shimoda-Matsubayashi, S., Matsumine, H., Morikawa, N., Hattori, N., Kondo, T., 1999. Genetic and environmental factors in the pathogenesis of Parkinson's disease. Adv. Neurol. 80, 171–179.

Moeljer, J.R., Eidelberg, D., 1997. Divergent expression of regional metabolic topographies in Parkinson's disease and normal aging. Brain 120, 2197–2206.

Palombo, E., Porrino, L.J., Bankiewicz, K.S., Crane, A.M., Sokoloff, L., Kopin, I.J., 1990. Local cerebral glucose utilization in monkeys with hemiparkinsonism induced by intracarotid infusion of the neurotoxin MPTP. J. Neurosci. 10, 860–869.

Palombo, E., Porrino, L.J., Crane, A.M., Bankiewicz, K.S., Kopin, I.J., Sokoloff, L., 1991. Cerebral metabolic effects of monoamine oxidase in normal and 1-methyl-4-phenyl-1,2,3,6-tetrahydropyridine acutely treated monkeys. J. Neurochem. 56, 1639–1646.

Paxinos, G., Huang, X.-F., Toga, A.W., 2000. The Rhesus Monkey Brain Atlas in Stereotaxic Coordinates. Academic Press, San Diego.

Phelps, M.E., Huang, S.C., Hoffman, E.J., Selin, C., Sokoloff, L., Kuhl, D., 1979. Tomographic measurement of local cerebral glucose metabolic rate in humans with (F-18-2-fluoro-2- deoxy-D-glucose: validation of method. Ann. Neurol. 6, 371–388.

Porrino, L., Burns, R.S., Crane, A.M., Palombo, E., Kopin, I.J., Sokoloff, L., 1987. Changes in local cerebral glucose utilization associated with Parkinson's syndrome induced by 1-methyl-4-phenyl-1,2,3,6-tetrahydropyridine (MPTP) in the primate. Life Sci. 40, 17657–17664.

Puyau, M., Adolph, A.L., Vohra, F.A., Butte, N.F., 2002. Validation and calibration of physical activity monitors in children. Obes. Res. 10, 150–157.

Reivich, M., Alavi, A., Wolf, A., Fowler, J., Russell, J., Arnett, C., et al., 1985. Glucose metabolism rate kinetic model parameter determination in humans: the lumped constants and rate constants for [^{18}F]fluorodeoxy- and [^{11}C]deoxyglucose. J. Cereb. Blood Flow Metab. 5, 179–192.

Sakakibara, R., Shinotoh, H., Yoshiyama, M., Hattori, T., Yamanishi, T., 2001. SPECT imaging of the dopamine transporter with [^{123}I]-beta-CIT reveals marked decline of nigrostriatal dopaminergic function in Parkinson's disease with urinary dysfunction. J. Neurol. Sci. 187, 55–59.

Schapira, A.H.V., 1996. Neurotoxicity and the mechanisms of cell death in Parkinson's disease, in: Battistin, L., Scarlato, G., Carceni, T., Ruggieri, S. (Eds.), Advances in Neurology, Vol. 69. Lippincott-Raven, Philadelphia, pp. 161–165.

Schmidt, N., Ferger, B., 2001. Neurochemical findings in the MPTP model of Parkinson's disease. J. Neural. Transm. 108, 1263–1282.

Sokoloff, L., Reivich, M., Kennedy, C., Des Rosiers, M.H., Patlak, C.S., Pettigrew, K.D., et al., 1977. The (C-14) deoxy glucose method for the measurement of local cerebral glucose utilization: theory, procedure, the normal values in the conscious and anesthetized albino rat. Neurochemistry 28, 897–916.

Stoessl, A.J., de la Fuente-Fernandez, R., 2003. Dopamine receptor in Parkinson's disease: imaging studies, in: Gordin, A., Kaakkola, S., Teravainen, H. (Eds.), Parkinson's Disease: Advances in Neurology, Vol. 91. Lippincott-Raven, Philadelphia, pp. 65–71.

Subramanyam, R., Alpert, N.M., Hoop Jr., B., Brownell, G.L., Taveras, J.M., 1978. A model for regional cerebral oxygen distribution during continuous inhalation of 15O2, C15O, and C15O2. J. Nucl. Med. 19, 43–53.

van Dyck, C., Seibyl, J.P., Malison, R.T., Laruelle, M., Zoghbi, S.S., Baldwin, R.M., et al., 2002. Age-related decline in dopamine transporters: analysis of striatal subregions, nonlinear effects, and hemispeheric asymmetries. Am. J. Geriatr. Psychiatry 10, 36–43.

van Nguyen, T., Brownell, A.-L., Chen, Y.I., Livni, E., Coyle, J.T., Rosen, B.R., et al., 2000. Detection of the effects of dopamine receptor supersensitivity using pharmacological MRI and correlation with PET. Synapse 36, 57–65.

Wichman, T., DeLong, M.R., 1996. Functional and pathophysiological models of the basal ganglia [Review]. Curr. Opin. Neurobiol. 6, 751–758.

Wichman, T., DeLong, M.R., 2003. Functional neuroanatomy of the basal ganglia in Parkinson's disease, in: Gordon, A., Kaakkola, S., Teravainen, H. (Eds.), Parkinson's Disease: Advances in Neurology, Vol. 91. Lippincott Williams & Wilkins, Philadelphia, pp. 9–18.

Wullner, U., Pakzaban, P., Brownell, A.-L., Hantraye, P., Burns, L., Shoup, T., et al., 1994. Dopamine terminal loss and onset of motor symptoms in MPTP-treated monkeys: a positron emission tomography study with [^{11}C]-CFT. Exp. Neurol. 126, 305–309.

Radiolabeling and biodistribution of methyl 2-(methoxycarbonyl)-2-(methylamino) bicyclo [2.1.1] - hexane -5-carboxylate, a potential neuroprotective drug

Meixiang Yu[a,*], Kjell Någren[b], Y. Iris Chen[a], Elijahu Livni[a], David Elmaleh[a], Alan Kozikowski[c], Xukui Wang[a], Kimmo Jokivarsi[a], Anna-Liisa Brownell[a]

[a]*Department of Radiology, Massachusetts General Hospital and Harvard Medical School, Bartlett Hall 511R, Boston, MA 02114, USA*
[b]*Turku PET Center, Turku, Finland*
[c]*Georgetown University Medical Center, Washington DC, USA*

Abstract

Methyl 2-(methoxycarbonyl) -2-(methylamino) bicyclo[2.1.1] -hexane -5-carboxylate (MMMHC) is developed as a potential neuroprotective drug. It was labeled with C-11 from the desmethyl precursor methyl 2-(methoxycarbonyl)-2-amino bicyclo[2.1.1]-hexane-5-carboxylate with [^{11}C]methyl triflate in acetone solution at 60 °C with labeling yield of 69% and with radiochemical purity of >99%. Positron Emission Tomography (PET) studies in a normal rat showed that Methyl 2-(methoxycarbonyl)-2-([^{11}C]methylamino)bicyclo[2.1.1]-hexane-5-carboxylate ([^{11}C] MMMHC) accumulated mainly in the cortical brain areas after iv administration. Frontal cortex/cerebellum ratios in a rat brain were 8.0/6.0, 6.8/4.2, 6.3/4.3, 5.5/4.2 and 5.2/4.5 percent of the injected dose in 100 ml at 2 min, 5 min, 10 min, 20 min and 40 min respectively after i.v. injection. During 20–40 min, 2.9 ± 0.4% of the total activity stayed in the brain. These results showed that MMMHC could be labeled with C-11 with high yield, and it passed the brain-blood barrier and accumulated in several brain regions.

---

* Corresponding author. Tel.: +1-617-726-6756; fax: +1-617-726-5123.
E-mail address: ymeixiang@partners.org (M. Yu).

Introduction

L-Glutamate is the major excitatory neurotransmitter in the mammalian central neural system, acting through both ligand gated ion channels (ionotropic receptors) and G-protein coupled (metabotropic) receptors (Dhami et al., 2002; Bonvento et al., 2002; McFeeters and Oswald, 2002). Glutamate has a role in a variety of physiological processes including development of synaptic plasticity, motor control, respiration and cardiovascular regulation (Sigrist et al., 2002; Fendt and Schmid, 2002; Gordon and Sved, 2002). An excessive or inappropriate stimulation of glutamate receptors leads to neural cell damage or loss, by a mechanism known as excitotoxicity (Blondeau et al., 2002). Neurotoxicity and chronic neurodegenerative diseases (e.g. Parkinson's and Huntington's disease) are also associated with abnormal activation of metabotropic glutamate receptors (mGluRs) (Rouse et al., 2000; Difazio et al., 1992). Investigation of metabotropic receptor function has been hampered because of lack of specific receptor ligands. So far, no functional in vivo imaging studies were published using mGluR labeled ligands. However, several drug discovery projects targeting metabotropic receptors were published recently (Fundytus, 2001; Ossowska et al., 2000; Knopfel et al., 1995). Kozikowski et al (Kozikowski et al., 1998) developed a mGluR agonist, 2-aminobicyclo[2.1.1]hexane-2,5-dicarboxylic acid-I (ABHx D-I, compound A in Fig. 1). In preliminary in vitro studies ABHx D-I was found to protect against neural death in several neurotoxic models including neurotoxicity induced by NMDA, by oxygen and glucose deprivation in mouse cortical neuronal-glial cultures. The ABHx D-I has two carboxylic acid functions, it is unlikely that the compound ABHx D-I can pass the brain-blood barrier (BBB) because of its high polarity (Platts et al., 2001). To overcome the polarity issue and allow potential BBB penetration, we designed a new compound, methyl 2-(methoxycarbonyl) -2-(methylamino) bicyclo[2.1.1] -hexane -5-carboxylate (MMMHC, Compound B in Fig. 1). We postulated that this methyl ester analogue might act as a pro-drug if it is metabolized into ABHx D-I in the brain by enzymatic degradation. To study the in vivo behavior of this compound (MMMHC), we labeled it with C-11 and conducted positron emission tomography (PET) imaging studies of its dynamic biodistribution in a rat model. The vivo pharmaco-kinetic behavior of the compound is essential to determine if it will be used as a drug for therapeutic purposes (Torchilin, 2000).

Materials and Methods

Materials

The reference compound MMMHC and the precursor for labeling were provided by Dr. Kozikowski (Kozikowski et al., 1998). Silver triflate was purchased from Aldrich and Graphpac
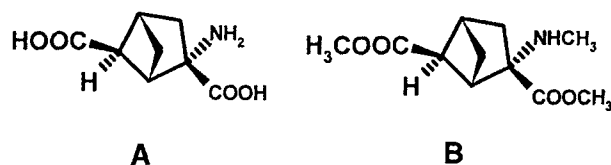

Fig. 1. Chemical structure of ABHx-D-I (A), MMMHC (B).

GC (80–100 mesh) from Alltech. Other chemicals were obtained from commercial sources and were of analytical grade.

Radiochemistry

Production of [^{11}C]carbon dioxide

[^{11}C]carbon dioxide was produced with the cyclotron using 16 MeV protons by the ^{14}N(p, α)^{11}C nuclear reaction on nitrogen. The [^{11}C]carbon dioxide was trapped in a stainless-steel coil cooled with liquid nitrogen before being transferred to the [^{11}C]methyl iodide/[^{11}C]methyl triflate system.

Preparation of [^{11}C]methyl triflate

[^{11}C]methyl iodide was prepared from cyclotron produced [^{11}C]carbon dioxide by standard methods (Någren and Halldin, 1998) and passed through a heated soda glass column (oven temperature 200 °C) containing silver triflate impregnated graphitized carbon (Jewett, 1992).

Preparation of methyl 2-(methoxycarbonyl) -2-([^{11}C]methylamino) bicyclo[2.1.1] -hexane -5-carbox-ylate ([^{11}C]MMMHC) from methyl 2-(methoxycarbonyl) -2-amino bicyclo[2.1.1] -hexane -5-carboxylate

0.3 mg precursor (Compound C in Fig. 2) in 300 μL acetone was used to trap [^{11}C]methyl triflate at 0 °C. After trapping, the reaction mixture was heated at 60 °C for 1 min. After addition of 200 μL HPLC solvent (0.01 M H$_3$PO$_4$/acetonitrile 9/1), the reaction mixture was purified by HPLC. The radioactive peak with a retention time (5 min) similar to a reference standard was collected. After evaporation, the residue was dissolved in saline buffer and sterilized by filtration through a 0.2-μm filter (Millex®-GV).

Preparative HPLC system

The radiotracer methyl 2-(methoxycarbonyl)-2-([^{11}C]methylamino) bicyclo[2.1.1] -hexane -5-carbox-ylate ([^{11}C]MMMHC) was purified by a HPLC system comprising a mobile phase, pump (Merck), an automatic sample injector (Merck, with 5 ml loop) and radioactivity detector (in-house construction). Separation was performed on a μ-Bondapak® C-18 column (7.8 × 300 mm, Waters) using acetonitrile and 0.01 M phosphoric acid (90/10) as the mobile phase with a flow of 6 ml/min.

Analytical HPLC system

The radioligand [^{11}C]MMMHC was analyzed by reversed-phase HPLC on a μ-Bondapak® C-18 column (3.9 × 300 mm, Waters) using a PC-controlled system with Merck HITACHI pump (type L-
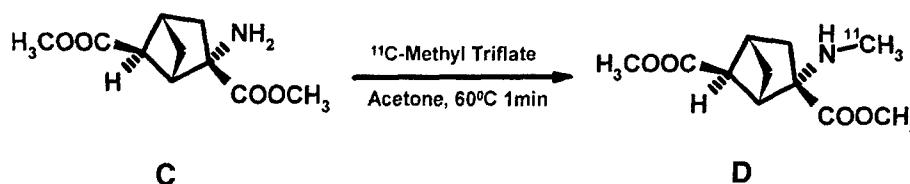

Fig. 2. The reactions of [^{11}C]Methyl triflate with desmethyl precursor C.

7100) and a UV absorbance detector (type L-7400) in series with radioactivity detector (model) (Yu et al., 1998). After injection of the purified product [^{11}C]MMMHC together with the unlabelled reference, the column was eluted with a gradient system starting from 90% of 0.01M H_3PO_4 and 10% of CH_3CN to 20% of 0.01M H_3PO_4 and 80% of CH_3CN at 8 min, then back to 90% of 0.01M H_3PO_4 and 10% of CH_3CN at 10 min with a flow rate of 2 ml/min, and UV absorbance was measured at 220 nm (the retention time R_t of the compound was 3.2 min).

Positron emission tomography studies

Positron emission tomography studies were carried out with in-house-built PET scanners PCR-I (Brownell et al., 1989) and super high-resolution rodent PET scanner (Correia et al., 1999). Both scanners are one-ring systems. The PCR-I (built 1983) has resolution of 4.5 mm and super high-resolution rodent PET scanner of 1.16 mm. However, the sensitivity in PCR-I is higher, which enables us to acquire whole body images of rats using "step and shoot" mode and a short acquisition time for each slice.

For PET imaging studies, animals were anaesthetized with halothane (1-1.5%) mixed to oxygen (3 L/min). Tail vein and artery were catheterized for infusion of the labeled ligand and drawing of blood samples needed for quantification at 2, 5, 10, 20 30 and 60 min after administration. The animal was placed in the imaging cradle and the head was adjusted into an in-house-built stereotactic head-holder. 0.5-1.0 mL volume was injected. For high resolution brain imaging with super high-resolution rodent PET scanner, sequential dynamic imaging data was acquired at one coronal midbrain level. For whole body imaging with PCR-I, data was acquired over the whole animal with 5 mm steps using a slice thickness of 5 mm. Calibration of the positron tomographs were performed in each study session using cylindrical plastic phantoms (diameters 2 or 6 cm) and ^{18}F solution. Imaging data was corrected for uniformity, sensitivity, attenuation, decay and acquisition time. PET images were reconstructed using Hanning-weighted convolution back projection with a cut-off value of 1.0. The coronal images of the whole body distribution were packed into a volume and reprocessed to transverse slices (Fig. 4). To determine the total accumulation in the brain, region of interest was drawn on all coronal slices, which cover the organ. Accumulation of radioactivity and number of pixels were determined of each slice to obtain the whole organ's specific values, which were related to the corresponding values of the whole animal. In addition, in the high resolution PET images (Fig. 5A), regions of interest, including the striatum, midbrain and cerebellum on both sides of the brain, were drawn and radioactivity per unit volume, percentage activity of injected dose and the ligand concentration were calculated (Fig. 5B).

Results

The desmethyl precursor reacted with [^{11}C]methyl triflate leading to the desired product [^{11}C]MMMHC (Fig. 2). The radiochemical yield of the labeling method was 69% (decay-corrected) within 40 min from EOB (end of bombardment), and the radiochemical purity of [^{11}C]MMMHC was higher than 99% as shown in Fig. 3. Using this method, the final product [^{11}C]MMMHC was prepared in batches containing more than 100 mCi, with high specific activity 800–1200 mCi/μmol. In the preparative HPLC purification system, the precursor was washed out earlier than the
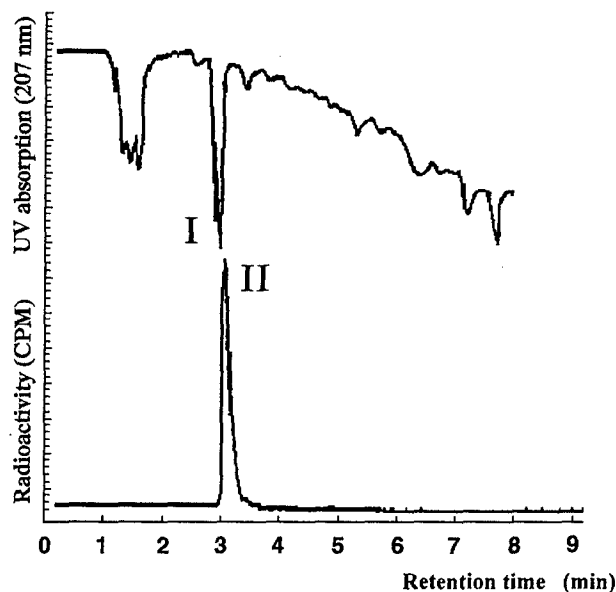
Fig. 3. Radiochemical purity analysis of the labeled compound [^{11}C]MMMHC by the HPLC chromatography (U.V. and radioactivity resus time). I (UV peak) and II (radioactivity peak) are product.

labeled compound, and the precursor cannot be detected by analytical HPLC system in the final product.

The whole body distribution of [^{11}C]MMMHC in a rat (Fig. 4) showed that after i.v. administration the radioactivity enters the brain, liver, kidneys and bladder. During 20–40 min, 2.9 $\pm$ 0.4% of the total activity stayed in the brain. The dynamic distribution of [^{11}C]MMMHC reached the peak around 2 minutes after i.v. injection as shown in Fig. 5B. After that, the radioactivity was partly washed out and the equilibrium was reached in several brain regions after 20 minutes. In the rat brain accumulation ratios of frontal cortex/cerebellum were 8.0/6.0, 6.8/4.2, 6.3/4.3, 5.5/4.2 and 5.2/4.5 percent of the injected dose in 100 ml (%ID/100mL) at 2 min, 5 min, 10 min, 20 min and 40 min respectively after i.v. injection. Furthermore, the high resolution imaging in the rat brain (Fig. 5A) showed that the [^{11}C]MMMHC accumulated especially in cortical areas.

Discussion

Three positions of the compound MMMHC (Compound B in Fig. 1) can be labeled with [^{11}C]methyl groups (two methyl ester positions, one methyl amine position). If a methyl ester position is chosen to label with [^{11}C]methyl triflate from the corresponding acid precursor, then the amine group in the precursor must be protected because of its high reactivity. After labeling, this protective group has to be selectively removed, which makes the labeling process more difficult. Alternatively, a better way to label the N-methyl function is to use [^{11}C]methyl triflate as we have done. C-11 methyl iodide is converted to C-11 methyl triflate before it is trapped in the reaction mixtures, because the C-11 methyl triflate was more reactive and the labeling yield was higher (Någren and Halldin, 1998).
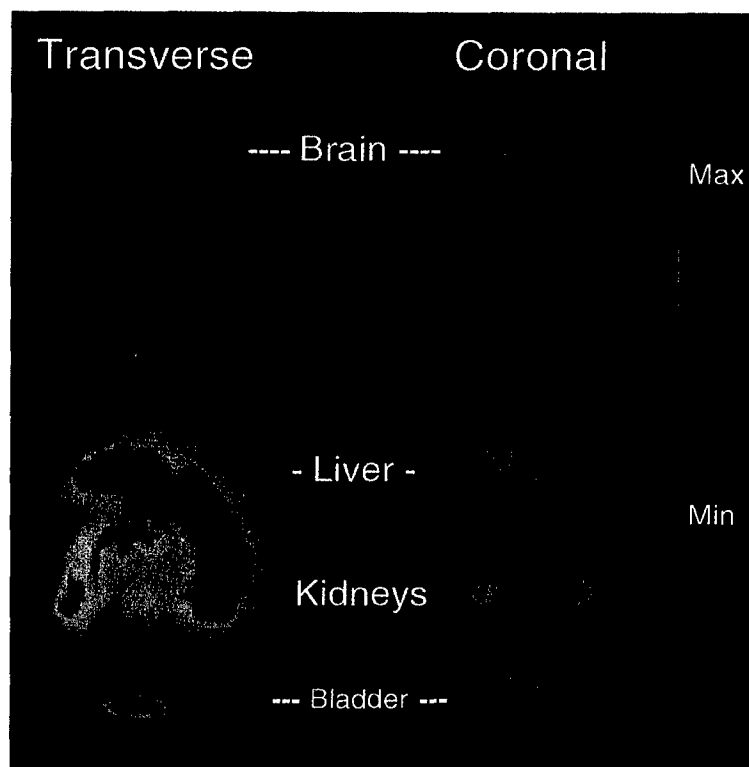
Fig. 4. Distribution of [^{11}C]MMMHC binding in a normal rat 20–40 min after administration of the labeled ligand.
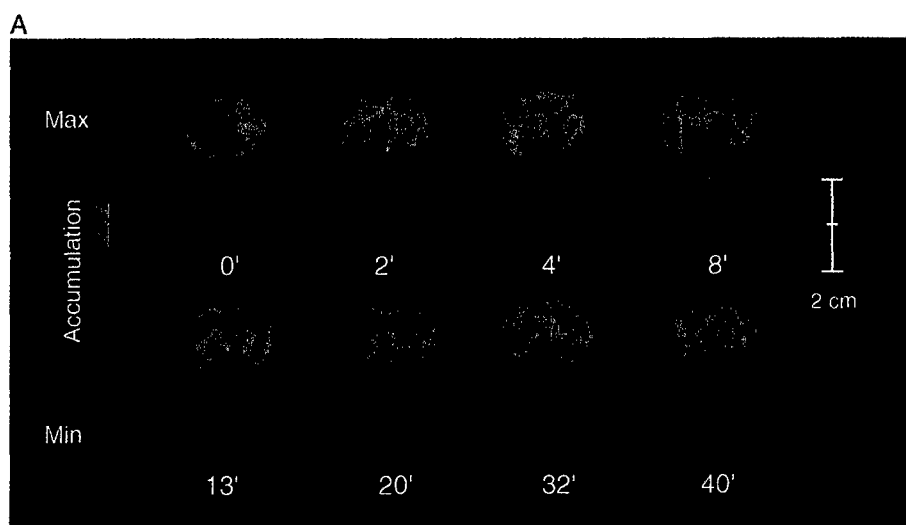

Fig. 5. A. Dynamic distribution of [^{11}C]MMMHC in a rat at the coronal midbrain level after iv injection. B. Time activity curves of [^{11}C]MMMHC binding in cerebellum and frontal cortex of a rat.
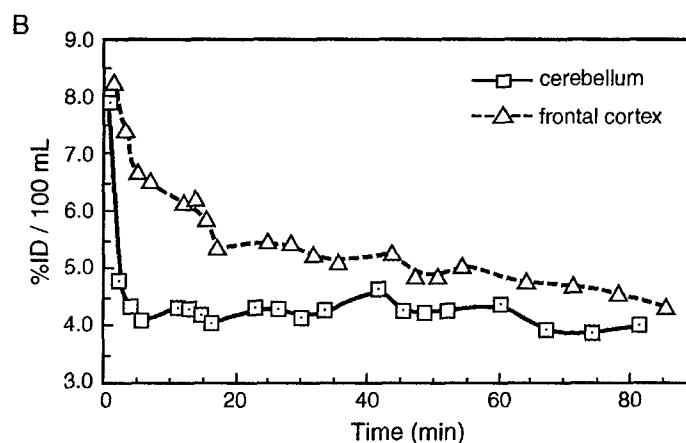
B

Fig. 5 (*continued*).

By using the N-desmethyl precursor, we got the C-11 labelled MMMHC in a good yield (69%) and high radiochemical purity (higher than 99%) as shown in Fig. 3. The byproduct with two [^{11}C]methyl groups on the amine nitrogen was not observed. The possible reason was that the amount of precursor was in high excess to [^{11}C]methyl triflate which had a high specific radioactivity (800–1200 mCi/μmol). It is useful to label one molecule in different positions in order to study its metabolites (Yu et al., 1999), however the selection of the position has to be done so that there will be no unwanted radiolabeled metabolites, which may interfere the imaging quality (Yu et al., 1997).

The distribution of [^{11}C]MMMHC in a normal rat showed that the radioactivity went into the brain (Fig. 5A and B) and the total brain accumulation between 20–40 min after i.v. administration was 2.9 ± 0.4% injected dose (ID). [^{11}C]MMMHC accumulates in the liver, and will be excluded through the kidneys into the bladder (Fig. 4). Most importantly, the [^{11}C]MMMHC kinetic distribution indicated reversible binding (Fig. 5B). The uptake reached the peak value in the brain (8–10% of the injected activity) at around 2 minutes after injection as shown in Fig. 5B, which was followed by a wash out that was a blood flow effect, and it reached equilibrium after 20 minutes. The high-resolution PET images show that the accumulation concentrated mainly in cortical structures (Fig. 5A).

The ABHx D-I (compound A in Fig. 1) is a physiologically active mGluR agonist (Kozikowski et al., 1998), it has two acid functions which make it quite polar and then difficult to pass the BBB. Schoepp et al have demonstrated that (2S)-2-Amino-2-(1S, 2S)-2-carboxycycloprop-1-yl)-3-(9-xan-thyl)propanoic acid, a mGlu II receptor antagonist also with two acid functions, has very low potential to pass the BBB. By using 10 mg/kg dose, they verified that the peak values of the compound in the brain were 243.4 ng/g (iv), 245.5ng/g (ip) at 30 min after administration (Ornstein et al., 1998). It is valuable to design a new lipophilic pro-drug (as compound B, MMMHC in Fig. 1) to pass the BBB which will be metabolized there to get an active metabolite. There are two ester and one N-methyl groups in the compound MMMHC, which make the MMMHC lipophilic and easy to pass the BBB as demonstrated in this experiment. Ester hydrolysis happens in the liver, meanwhile the ester hydrolase in the brain (in both myelin and microsomes) is also active for the ester metabolism (Shand and West, 1995; Ghosh and Grogan, 1990; Arnaud et al., 1981), and ester hydrolysis is a mechanism to carry

some drug into the brain (Walovitch et al., 1994). Meanwhile, N-demethylation happens in the liver and also in the brain. N-desmethyl metabolite is a degradation product for the drugs with N-methyl amine structure by N-demethylase in the brain microsomes (Ravindranath et al., 1989; Hahn and Fishman, 1980; Kawashima et al., 1996). The pro-drug MMMHC can go to the brain and might be metabolized there to active ABHx D-I. We will continue this project to study the MMMHC metabolism in future experiments.

Conclusion

The compound methyl 2-(methoxycarbonyl)-2-(methylamino) bicyclo[2.1.1] hexane-5-carboxylate could be labeled with carbon-11 from its free base desmethyl precursor in high yield and high radiochemical purity. In vivo studies showed that the [^{11}C]MMMHC passed the brain-blood barrier and illustrated reversible binding properties in the brain.

Acknowledgements

References

Arnaud, J., Nobili, O., Boyer, J., 1981. Effect of adrenocorticotrophic hormone on the activity of sterol ester hydrolase from rat brain. Biochemical and Biophysical Research Communications 100 (3), 1167–1172.

Bonvento, G., Sibson, N., Pellerin, L., 2002. Does glutamate image your thoughts? Trends in Neurosciences 25 (7), 359–364.

Blondeau, N., Lauritzen, I., Widmann, C., Lazdunski, M., Heurteaux, C., 2002. A potent protective role of lysophospholipids against global cerebral ischemia and glutamate excitotoxicity in neuronal cultures. Journal of Cerebral Blood Flow and Metabolism 22 (7), 821–834.

Brownell, G.L., Burnham, C.A., Stearns, C.W., Chesler, D.A., Brownell, A.-L., Palmer, M., 1989. Development in high-resolution positron emission tomography at MGH. Int. J Img Systems and Technol 1, 207–217.

Correia, J., Burnham, C., Kaufman, D., Fischman, A., 1999. Development of a small animal PET imaging device with resolution approaching 1 mm. IEEE Trans Nucl Sci 46 (3), 631–635.

Dhami, G.K., Anborgh, P.H., Dale, L.B., Sterne-Marr, R., Ferguson, S.S., 2002. Phosphorylation-independent regulation of metabotropic glutamate receptor signaling by G protein-coupled receptor kinase 2. Journal of Biological Chemistry 277 (28), 25266–25272.

Difazio, M.C., Hollingsworth, Z., Young, A.B., Penney Jr., J.B., 1992. Glutamate receptors in the substantia nigra of Parkinson's disease brains. Neurology 42 (2), 402–406.

Fendt, M., Schmid, S., 2002. Metabotropic glutamate receptors are involved in amygdaloid plasticity. European Journal of Neuroscience 15 (9), 1535–1541.

Fundytus, M.E., 2001. Glutamate receptors and nociception: implications for the drug treatment of pain. CNS Drugs 15 (1), 29–58.

Gordon, F.J., Sved, A.F., 2002. Neurotransmitters in central cardiovascular regulation: glutamate and GABA. Clinical and Experimental Pharmacology and Physiology 29 (5–6), 522–524.

Ghosh, S., Grogan, W.M., 1990. Activation of myelin-associated cholesteryl ester hydrolase in developing rat brain. Brain Research. Developmental Brain Research 54 (1), 147–149.

Hahn, E.F., Fishman, J., 1980. Changes in brain N-demethylation and opiate receptor content correlate with analgesic effectiveness of morphine. Research Communications in Chemical Pathology and Pharmacology 29 (1), 197–200.

Jewett, D.M., 1992. A simple synthesis of [^{11}C] methyl Triflate. Appl Radiat Isot 43, 1383–1385.

Kozikowski, A.P., Steensma, D., Araldi, G.L., Tuckmantel, W., Wang, S., Pshenichkin, S., Surina, E., Wroblewski, J.T., 1998. Synthesis and biology of the conformationally restricted ACPD analogue, 2-aminobicyclo[2.1.1]hexane-2,5-dicarboxylic acid-I, a potent mGluR agonist. Journal of Medicinal Chemistry 41 (10), 1641–1650.

Kawashima, H., Sequeira, D.J., Nelson, D.R., Strobel, H.W., 1996. Genomic cloning and protein expression of a novel rat brain cytochrome P-450 CYP2D18* catalyzing imipramine N-demethylation. Journal of Biological Chemistry 271 (45), 28176–28180.

Knopfel, T., Kuhn, R., Allgeier, H., 1995. Metabotropic glutamate receptors: novel targets for drug development. Journal of Medicinal Chemistry 38 (9), 1417–1426.

McFeeters, R.L., Oswald, R.E., 2002. Structural mobility of the extracellular ligand-binding core of an ionotropic glutamate receptor. Analysis of NMR relaxation dynamics. Biochemistry 41 (33), 10472–10481.

Någren, K., Halldin, C., 1998. Methylation of amide and thiol functions with [^{11}C]methyl triflate, as exemplified by [^{11}C]NMSP, [^{11}C]flumazenil and [^{11}C]Methionine. Journal of Labelled Compounds and Radiopharmaceuticals 41 (9), 831–841.

Ossowska, K., Pietraszek, M., Wardas, J., Nowak, G., Zajaczkowski, W., Wolfarth, S., Pilc, A., 2000. The role of glutamate receptors in antipsychotic drug action. Amino Acids 19 (1), 87–94.

Ornstein, P.L., Bleisch, T.J., Arnold, M.B., Kennedy, J.H., Wright, R.A., Johnson, B.G., Tizzano, J.P., Helton, D.R., Kallman, M.J., Schoepp, D.D., Herin, M., 1998. 2-substituted (2SR)-2-amino-2-((1SR,2SR)-2-carboxycycloprop-1-yl)glycines as potent and selective antagonists of group II metabotropic glutamate receptors. 2. Effects of aromatic substitution, pharmacological characterization, and bioavailability. Journal of Medicinal Chemistry 41 (3), 358–378.

Platts, J.A., Abraham, M.H., Zhao, Y.H., Hersey, A., Ijaz, L., Butina, D., 2001. Correlation and prediction of a large blood-brain distribution data set-an LFER study. European Journal of Medicinal Chemistry 36 (9), 719–730.

Rouse, S.T., Marino, M.J., Bradley, S.R., Awad, H., Wittmann, M., Conn, P.J., 2000. Distribution and roles of metabotropic glutamate receptors in the basal ganglia motor circuit: implications for treatment of Parkinson's disease and related disorders. Pharmacology and Therapeutics 88 (3), 427–435.

Ravindranath, V., Ananda Theertha Varada, H.K., 1989. High activity of cytochrome P-450-linked aminopyrine N-demethylase in mouse brain microsomes, and associated sex-related difference. Biochemical Journal 261 (3), 769–773.

Sigrist, S.J., Thiel, P.R., Reiff, D.F., Schuster, C.M., 2002. The postsynaptic glutamate receptor subunit DGluR-IIA mediates long-term plasticity in Drosophila. Journal of Neuroscience 22 (17), 7362–7372.

Shand, J.H., West, D.W., 1995. Inhibition of neutral cholesteryl ester hydrolase by the glycolytic enzyme enolase. Is this a secondary function of enolase? Lipids 30 (8), 763–770.

Torchilin, V.P., 2000. Drug targeting. European Journal of Pharmaceutical Sciences 11 (Suppl. 2), S81–S91.

Walovitch, R.C., Cheesman, E.H., Maheu, L.J., Hall, K.M., 1994. Studies of the retention mechanism of the brain perfusion imaging agent 99mTc-bicisate (99mTc-ECD). Journal of Cerebral Blood Flow and Metabolism 14 (Suppl. 1), S4–S11.

Yu, M., Någren, K., Halldin, C., Swahn, C.-G., Helfenbein, J., Guilloteau, D., 1999. Synthesis of [p-methyl-^{11}C]RTI-32: A New Tool for the In Vivo Evaluation of the metabolism of phenyltropane dopamine reuptake compounds. Labelled Compounds and Radiopharmaceuticals 42 (Suppl. 1), S469–S471.

Yu, M., Bergstrom, K.A., Kuikka, J.T., Yang, J., Vanninen, E., 1998. Comparison of HPLC, TLC and Minicolumn for measuring the radiochemical purity of [^{99}Tc^{m}]Q12. Nuclear Medicine Communication 19, 483–487.

Yu, M., Bergström, K.A., Halldin, C., Kuikka, J.T., Swahn, C.G., Åkerman, K., Hiltunen, J., Tiihonen, J., Lassen, N., Widebeck, C., Farde, L., 1997. Does The Lipophilic Labeled Metabolite of [^{123}I]Epidepride Obstruct Dopamine D2 Brain Imaging? European Journal of Nuclear Medicine 24, 880.

3-Nitropropionic acid-induced neurotoxicity – assessed by ultra high resolution positron emission tomography with comparison to magnetic resonance spectroscopy

Anna-Liisa Brownell,* Y. Iris Chen,* Meixiang Yu,* Xukui Wang,* Alpaslan Dedeoglu,†
Francesca Cicchetti,‡ Bruce G. Jenkins* and M. Flint Beal§

*Department of Radiology, Massachusetts General Hospital, Boston, Massachusetts, USA

†Veterans Administration Medical Center, Bedford, Massachusetts, USA

‡Unite de Neuroscience, CHUL, Quebec, Canada

§Department of Neurology and Neuroscience, Weill Medical College of Cornell University, New York Presbyterian Hospital, New York, USA

Abstract

To explore acute and long-term effects of 3-nitropropionic acid (3-NP)-induced neurotoxicity, longitudinal positron emission tomography (PET) studies of energy metabolism and magnetic resonance spectroscopic (MRS) studies of neurochemicals were conducted in a rat model. The first injection of 3-NP (20 mg/kg i.p.) was followed by MRS study of neurochemicals and PET study of glucose utilization using [^{18}F]2-fluorodeoxy- D-glucose (^{18}F-FDG). After that, 3-NP administration was done two times a day with a dose of 10 mg/kg i.p. until animals were symptomatic or for a maximum of 5 days combined with daily PET studies. Long-term effects were investigated 4 weeks and 4 months after cessation of 3-NP. These studies showed a significant inter-animal variation in response of 3-NP toxicity. Animals that developed large striatal lesions had decreased glucose utilization in the striatum and cortex 1 day after starting 3-NP injections. Similarly succinate and lactate/macromolecule levels were enhanced; these changes being, however, reversible. Progressive degeneration was observed by decreasing striatal glucose utilization and N-acetylaspartate (NAA) and increasing choline. These observations paralleled with weight loss and deficits in behavior. Animals that did not develop lesions showed reversible enhancement in cortical glucose utilization and no change in striatal glucose utilization or neurochemicals or locomotor activity.

Keywords: glucose utilization, Huntington's disease, magnetic resonance spectroscopy, neurodegeneration, 3-nitropropionic acid, positron emission tomography.

J. Neurochem. (2004) **89**, 1206–1214.

Neurotoxicity-related cell damage is often associated with mitochondrial energy impairment, which originates a chain of different pathophysiological processes finally ending in cell death (Brennan *et al.* 1985; Beal 1998). 3-Nitropropionic acid (3-NP), an inhibitor of mitochondrial oxidative metabolism, has been ingested as a component in moldy sugarcane resulting in selective neuronal death and symptoms similar to Huntington's disease (HD) (Ludolph *et al.* 1991). Subsequently, 3-NP has been widely used as an experimental model of HD as well as a model to study energy metabolism and cell death (Beal 1992) *in vivo* (Beal *et al.* 1993) and *in vitro* (Fink *et al.* 1996; Pang and Geddes 1997). Although HD is associated with a gene mutation (Huntington's Disease Collaborative Group 1993), the

etiology of the disorder is still unknown. Progression of the disease might be a result of energy impairment-induced slow excitotoxic neuronal death (Albin and Greenamyre 1992; Beal *et al.* 1993).

3-NP, an inhibitor of succinate dehydrogenase (Alston *et al.* 1977) creates mitochondrial inhibition and through inhibition of Complex II activity of the electron transport chain causes depletion of intracellular ATP synthesis, leading to striatal degeneration.

3-NP-induced pathophysiological changes are time-dependent and some are reversible. Lee *et al.* (2000) showed that after 3-NP toxication, succinate and lactate/macromolecules are increased immediately and remain enhanced for several days; this process is, however, reversible. In addition, Dautry *et al.* (2000) showed that the early decrease of *N*-acetylaspartate (NAA) induced by chronic 3-NP administration is reversible and consistent with mitochondrial dysfunction since NAA is synthesized within mitochondria. However, when toxicity continues, NAA will decrease again, which indicates the death of neurons.

Since glucose is the major energy source of the brain, changes in glucose utilization can serve as a sensitive indicator of energy requirements in brain (Di Chiro 1987; Palombo *et al.* 1990; Eberling *et al.* 1994; Eidelberg *et al.* 1996; Antonini *et al.* 1998; Dethy *et al.* 1998; Higashi *et al.* 2000). Glucose utilization can be investigated by positron emission tomography (PET) imaging using ^{18}F-labeled 2-fluorodeoxy-D-glucose (^{18}F-FDG) as a tracer. ^{18}F-FDG is transported from bloodstream into brain and to the metabolic cycle by hexokinase enzyme (Sokoloff *et al.* 1977). ^{18}F-FDG will not go through the whole metabolic cycle but remains in [^{18}F]glucose 6-phosphate in the brain for several hours and enables quantitative imaging studies. Since the hexokinase enzyme is activated in relation to the energy requirements of the tissue, the accumulation of ^{18}F-FDG reflects the metabolic rate of glucose (Phelps *et al.* 1979).

To investigate acute and prolonged effects of 3-NP-induced neurotoxicity, we conducted *in vivo* imaging studies in a rat model of striatal energy metabolism using ^{18}F-FDG by PET and neurochemicals by magnetic resonance spectroscopy (MRS) (Jenkins *et al.* 1996). These *in vivo* imaging techniques allowed us to perform longitudinal studies of different pathophysiological processes in the same animals. For PET imaging we used an in house built super-high resolution imaging device.

Methods

Neurotoxin

3-Nitropropionic acid (3-NP) (Sigma Aldrich Co., St Louis, MO, USA) solution was prepared by dissolving 3-NP powder in buffered 0.9% saline and pH was adjusted to 7.4 with concentrated sodium hydroxide.

Experimental procedures in rats

Animals used in this study were maintained according to the guidelines of the Committee on Research Animals of the Massachusetts

General Hospital and of the *Guide for Care and Use of Laboratory Animals* of the Institute of the Laboratory Animal Resources, National Research Council, Department of Health, Education and Welfare, Publication No. (NIH) 85–23.

An acute effect of the neurotoxin 3-NP was investigated in 12 rats (male Sprague–Dawley from Charles River Laboratories, weight of 300 g) using the following daily time schedule: The first injection of 3-NP (20 mg/kg i.p.) was followed by MRS study of neurochemicals and PET study of glucose utilization. After that, 3-NP administration was done two times a day with a dose of 10 mg/kg i.p. according the following time schedule: 10 a.m. PET imaging study; 12 p.m. 3-NP administration; and 8 p.m. 3-NP administration. This protocol was repeated until symptoms developed (gait observed) or for a maximum of 5 days treatment. During the treatment period, rats were individually housed in metabolic cages, and their diet and excretion were closely monitored. Motor deficits were evaluated using a quantitative neurological coding scale developed by Guyot *et al.* (1997) and Ouary *et al.* (2000).

Briefly, the observed deficits were scored as intermittent dystonia of one hindlimb, score = 1; intermittent dystonia of two hind limbs, score = 2; permanent dystonia of hind limbs, score = 3; gait abnormalities consisting mainly of an uncoordinated and wobbling gait (score = 4); recumbence lying on one side but showing uncoordinated movements when stimulated, score = 5; near death by almost complete paralysis, score = 6; in addition, capability to grasp with their forepaws (able = 0, unable = 1) and capability to stay on small platform for 10 s (able = 0, unable = 1). Weight progression was followed by daily measurements up to 80 days (Fig. 1).

To investigate long-term degeneration, imaging studies of glucose utilization by PET were repeated at 4 weeks and 4 months after the cessation of 3-NP administrations (Table 1). Correspondingly, studies of neurochemicals by MRS were repeated in two animals at 4 weeks after 3-NP administrations.

For imaging studies rats were anesthetized with halothane (1.0–1.5% with oxygen flow rate of 3 L/min). For PET studies, catheters were introduced into the tail vein for administration of radiolabeled ligands and into the tail artery for drawing of blood samples, which
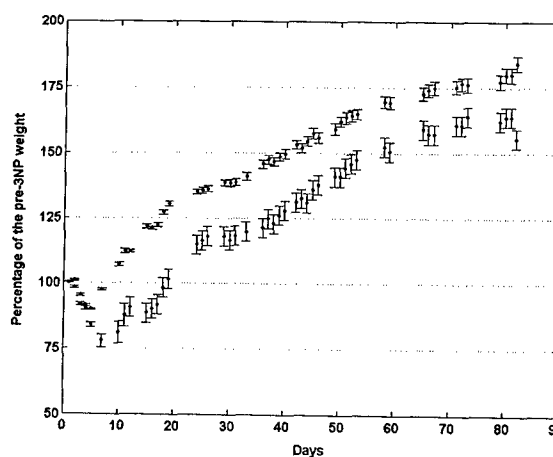

Fig. 1 Weight progression during and after 3-NP administrations. The curves represent maximum (highly symptomatic, behavioral score 2–6) and minimum (no symptoms, behavioral score 0–1) changes of 12 animals investigated.

Table 1 Glucose utilization in four areas of rat brain before, during and after 3-NP neurotoxicity

Procedure	Time	n	Striatum	Cingular	S1/S2 cortex	Cerebellum
Before 3-NP Behavioral score 0–1		12	55.2 ± 7.4	64.0 ± 7.4	65.2 ± 12.0	55.4 ± 5.8
During 3-NP administrations	1 day	6	56.4 ± 20.8	71.8 ± 24.2	72.6 ± 23.2	58.4 ± 12.8
	2 days	6	54.0 ± 14.8	69.6 ± 18.4	76.8 ± 21.2	60.4 ± 12.4
	3 days	5	55.8 ± 10.8	76.2 ± 19.6	80.8 ± 19.2	55.6 ± 9.8
	4 days	4	56.6 ± 7.8	71.6 ± 16.8	75.6 ± 16.2	54.4 ± 6.7
After cessation of 3-NP Behavioral score 2–6	2 days	3	54.8 ± 10.2	67.8 ± 12.4	70.4 ± 12.8	56.2 ± 6.6
During 3-NP administrations	1 day	6	49.8 ± 30.8	56.4 ± 30.6	60.8 ± 35.8	54.4 ± 33.8
	2 days	6	47.2 ± 11.0	66.4 ± 10.8	65.8 ± 17.4	53.8 ± 9.2
	3 days	6	40.4 ± 5.0*	56.8 ± 6.4*	51.4 ± 16.2	54.2 ± 16.6
	4 days	4	35.8 ± 11.6*	35.8 ± 19.8*	49.8 ± 13.8*	42.2 ± 23.8
After cessation of 3-NP	2 days	3	26.2 ± 10.4*	35.0 ± 19.6*	35.2 ± 14.0*	45.4 ± 18.2
	4 weeks	3	40.4 ± 12.8*	40.6 ± 13.6*	46.8 ± 16.6*	51.4 ± 14.2
	16 weeks	2	29.4 ± 6.4*	37.4 ± 12.6*	37.4 ± 13.2*	45.8 ± 24.8

Rats were divided into two groups based on behavioral response to 3-NP. In group I motor score was between 0 and 1 according the scale of Guyot *et al.* (1997) and Ouary *et al.* (2000) and no striatal lesion was observed by PET studies of glucose utilization. In the group II the motor score was between 2 and 6 and large striatal lesions were developed. Glucose metabolic rate was calculated using Sokoloff (Sokoloff *et al.* 1977) model based on *in vivo* PET imaging studies using [^{18}F]2-fluorodeoxy-D-glucose as a tracer. A value of 0.5 was used for the lump constant. Data are presented as mean ± SD in units of μmol/100 mL min. Statistical comparison was done using Student's *t*-test.
*Comparisons were considered statistically significant at $p \leq 0.05$.

were needed to determine glucose level and blood input function for quantification of glucose metabolic rate. A heated waterbed was used to maintain body temperature for all imaging sessions (PET, MRS). Anesthetized animals were mounted onto a stereotactic headholder to allow accurate repositioning of the animal in longitudinal studies.

To verify the information obtained by the imaging studies, histological evaluation of brains was performed. Rats were deeply anesthetized by ketamine/xylaxine (100 mg/10 mg/kg i.m.) and then transcardially perfused with 4% buffered formaldehyde. The brains were removed, post-fixed with the perfusant for 2 h, cryoprotected in a graded series of 10% and 20% glycerol in 2% dimethylsulfoxide solution, subsequently serially frozen, sectioned at 50 μm, stored in 6-well tissue collection clusters, and stained for Nissl substance (cresyl violet).

PET imaging techniques with a super-high resolution tomograph

PET imaging studies of glucose metabolism were conducted using a super high resolution in-house built (Correia *et al.* 1999) PET imaging device (Fig. 2). The spatial resolution of the system is at the center of the field $1.16 \times 1.16 \times 1.3$ mm^3. This enables to investigate metabolic changes in tiny elements (~2 μL) inside the rat brain. However, since the signals originate from such tiny elements, high radioactivity levels were required to produce statistically meaningful signals and images.

A computer controlled imaging 'table' has been developed for the super high-resolution scanner. The diameter of the bore in the PET system is 6 cm and the imaging 'table' moves through it in a 'step and shoot' mode (Fig. 2). The length of the axial steps can be selected by the acquisition program with the smallest step size of 12.5 μm. The stereotactic headholder with earbars and mouth (teeth) bar can be

Fig. 2 Rat experiment in a super high resolution PET scanner. Side view shows a rat secured into the stereotactic headholder in the imaging 'table' sliding into the tomograph. Front view shows the head inside the collimator ring and some electronics of the tomograph.

mounted onto the 'table' to ensure the standard positioning of the animals. For the experimental procedure, the animal is secured onto the 'table' through the stereotactic headholder, which is equipped with a gas inhalation system. The 'table' is then screwed onto a cradle attached to the control motor in the imaging device (Fig. 2).

Software was developed to control the movement of the imaging 'table' to allow scanning of the whole brain, slice by slice. PET signals were corrected for uniformity and attenuation using a mathematical attenuation correction with an attenuation coefficient of 0.096. Image reconstruction was done using Hanning filtered convolution backprojection with a cut-off value of 1.0. Cross-calibration of the tomograph was done with a gammacounter (Packard Cobra Auto-gamma, Downers, IL, USA) using ^{18}F-labeled water. Cross-calibration is needed to quantify the blood samples drawn during the imaging acquisition.

PET imaging studies of glucose utilization
For imaging studies, 3–4 mCi of ^{18}F-FDG was administered into the tail vein. Ten arterial blood samples (50 μL) were drawn from the
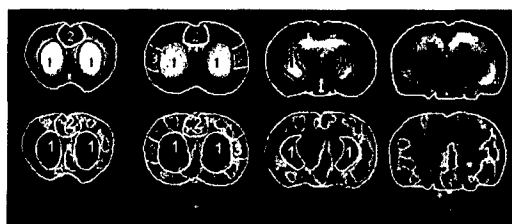
Fig. 3 Regions of the interest were drawn on the coronal MR images (striatum = 1; cingulate = 2; S1/S2 cortex = 3) and then overlaid with PET images. The PET data used for quantification was averaged from the areas on the left and right side.

tail artery starting 30 s after administration of radioactivity with an increasing time interval for total of 20 min. Glucose level was determined before the administration of radioactivity. Dynamic accumulation of radioactivity into the brain was acquired by PET for 25 min at one brain level (10 mm anterior to the earbar). By that time a steady-state level of radioactivity was achieved and sequential imaging of distribution of radioactivity was done by 'step and shoot' mode over the whole brain using 1.25 or 2.5 mm steps with slice thickness of 1.3 mm.

After image reconstruction, PET images were overlaid with anatomical MR images for drawing regions of interest from striatum, cingulate, S1/S2 cortex and cerebellum (Fig. 3). Glucose utilization was calculated using a Sokoloff model (Sokoloff *et al.* 1977) extended by Phelps *et al.* (1979) using a value of 0.5 for the lumped constant (Brownell *et al.* 1991). Data fitting to the model was done using SAAM II software package (Foster 1994) with convergence criterion of 1.0e-6.

Imaging studies of neurochemicals and anatomy

MRI and MRS studies were conducted with a commercial GE Omega 4.7 T system with a home-built, transmit/receive bird-cage design proton coil tuned to 200.17 MHz. At first, anatomical imaging was done to outline the region of interest, of which single voxel spectra were acquired. T2 weighted images (TR : TE = 3000 : 40 or 80) were acquired of the rat brain to obtain 1.2 mm thick slices with in plane resolution of 0.16 mm. These anatomical images were also used as base maps to overlay with PET images for selection of region of interest for data analyses. For single voxel spectra, voxels were located symmetrically over the basal ganglia ($6 \times 3.5 \times 3$ mm^3) and the motor cortex ($6 \times 2 \times 3$ mm^3). Water suppression was provided for by CHESS pulses and localization by a standard PRESS-type sequence (TR 2000 ms; TE 68, 136 and 272 ms). Spectra were processed using the NMR1 program (NMRI, Syracuse, NY, USA), by curve fitting the entire spectrum and integrating the areas of the major metabolites. Integrals were then normalized to the creatine/phosphocreatine peak at 3.03 p.p.m. (Cr) as a standard.

Results

Weight loss and behavior deficit

We found a significant inter-animal variation in acute response of 3-NP toxication on locomotor activity. The motor deficit score (Guyot *et al.* 1997; Ouary *et al.* 2000) varied

from 0 to 6. Six of the 12 rats showed significant hypokinesia. Three of the six had hindlimb paralyses and the motor score was between 4 and 6. The other three rats had motor scores of 2–3. In the remaining group of rats, three did not show any observable changes in locomotor activity (scored 0), whereas the three others showed a slight slowness and occasional uncoordinated gait (scored 1). The observations in motor activity are similar to those published by Borlongan *et al.* 1997) and Guyot *et al.* 1997). All the animals lost weight after 3-NP administrations. The animals with the strongest response to 3-NP (behavioral score between 2 and 6) lost $24 \pm 4\%$ of their weight and the weight loss extended 4 days after the cessation of neurotoxicity. The maximum weight loss in the other group was $12 \pm 2\%$, and the weight loss stopped the day after the cessation of 3-NP administrations. The maximum weight loss between these two groups was significant ($p < 0.005$, Student's t-test). Weight progression in both groups was linear after the cessation of 3-NP; weight $(t) = (1.08 \pm 0.04)t + 105 \pm 2$ $(r = 0.981)$ in the non-defected group and weight $(t) = (1.14 \pm 0.04)t + 78 \pm 2$ $(r = 0.972)$ in the defected group. Even the rate of weight progression was higher in the defected group; the average weight never reached the weight level of the group with scores 0–1 during the 80 days of follow-up (Fig. 1).

Glucose utilization

The daily ^{18}F-FDG imaging studies during 3-NP administration period showed significant inter-animal variation of glucose utilization in response to the acute toxin; similar to motor activity. The rats that did not show any motor symptoms developed enhanced glucose utilization in cortical areas with a maximum enhancement of 19–24% on the third day after starting the 3-NP administration. At the cessation of 3-NP administration, the glucose utilization was still enhanced by 12–16% and 2 days later by 6–8%. No significant changes in striatal glucose utilization were observed during that time (Fig. 4). The animals with hindlimb paralyses developed extensive striatal lesions. Table 1 shows the changes of glucose metabolism in four different brain areas (striatum, cingulate, S1/S2 cortex, and cerebellum; Fig. 5) during and after 3-NP toxication in the animals whose motor score was between 2 and 6. The striatum was the most affected brain area and the cerebellum was the least affected one. The average decrease of glucose utilization in the striatum at the end of 3-NP injections was 35% and the development of the progressive decrease started 1 day after the first 3-NP injection (Fig. 5). On day 3, large lesions were clearly observable in several slices, which cover the whole striatum. Interestingly, glucose utilization continued to decrease until at least 2 days after the cessation of 3-NP, after which a short period of recovery was observed, followed by a long-term degeneration. As an early response to 3-NP toxicity, cingulate and S1/S2 cortical areas showed minimal change
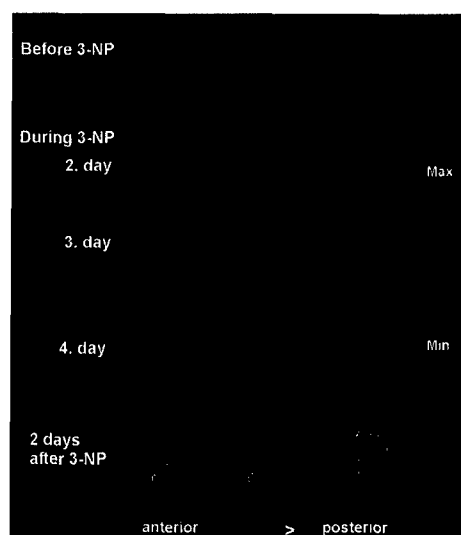
Fig. 4 Coronal PET images of glucose utilization in a rat brain before 3-NP; 2nd, 3rd, and 4th day during 3-NP administration; and 2 days after the cessation of 3-NP. The images show enhanced cortical accumulation of ^{18}F-FDG during the 3-NP administration and this rat did not develop striatal lesions or motor symptoms. The slice thickness is 1.3 mm and slice to slice distance 3.75 mm.
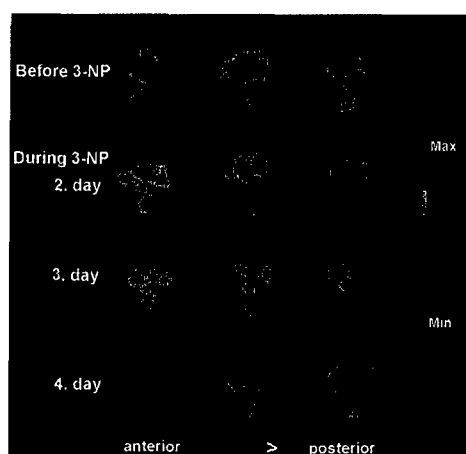

Fig. 5 An acute response of 3-NP toxicity in a rat that developed striatal lesions. Coronal slices of ^{18}F-FDG accumulation before 3-NP and 2nd, 3rd and 4th day during 3-NP administrations show time-scale of the development of lesions. This rat had significant behavioral deficit (score 5). The slice thickness and slice to slice distance is the same as above.
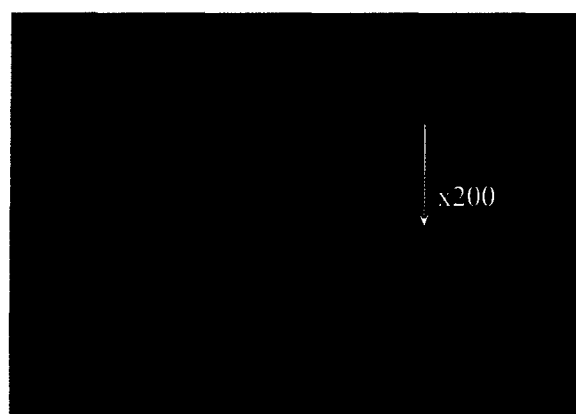

Fig. 6 Postmortem histology conducted 2 days after the cessation of 3-NP administrations verifies the striatal lesion detected by decreased glucose utilization using PET. Nissl stained whole brain coronal section through the striatum at the level of the anterior commisure shows extension of the neuronal damage. The magnification (× 200) shows the level of damage.

MRS studies of neurochemicals

Two hours after 3-NP toxicity, MRS showed elevated levels of succinate, lactate and macromolecules (Figs 7 and 8). During the following 150 min the increase rate of lactate/macromolecules was 31 ± 9%/min; succinate 5.3 ± 0.5%/min and choline 0.06 ± 0.01%/min (Fig. 7). These elevated values, however, diminished within 4 weeks (Fig. 8), indicating a reversible process. At this time, elevated striatal choline and decreased NAA levels were observed, indicating
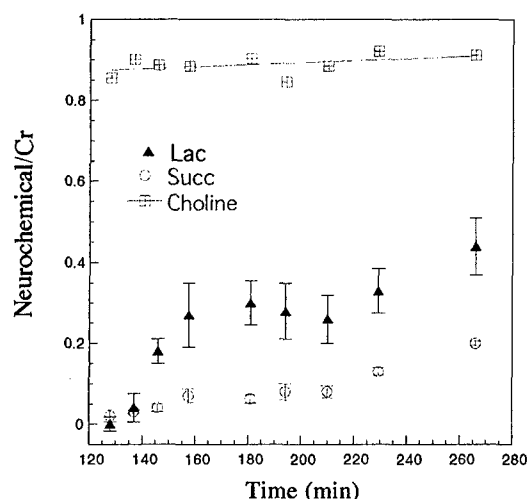
Fig. 7 Acute changes of neurochemicals in the striatum observed immediately after the first injection of 3-NP (20 mg/kg i.p.). Increased lactate and succinate can be observed 2 h after 3-NP injection accompanied with a slow increase in choline. The fast increased succinate (5.3 ± 0.5%/min) and lactate/macromolecule (31 ± 9%/min) levels might be an indication of 3-NP-induced necrosis in the striatum. These fast processes were reversible, as shown in Fig. 8.

or even small increase in glucose utilization (Table 1). However, as a long-term response these areas also showed decreased glucose utilization. Figure 6 shows the histological validation of the neural loss, which correlates well with the decreased glucose utilization in the striatum 2 days after the cessation of 3-NP.

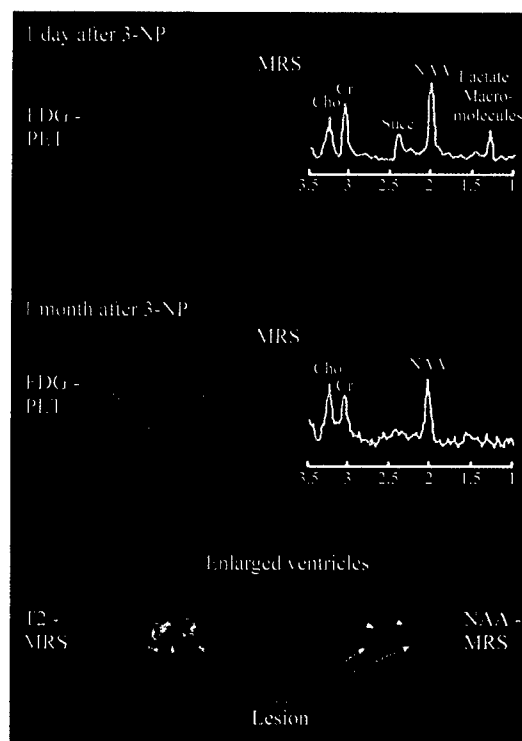**Fig. 8** Comparison of glucose utilization using PET, single voxel MRS and T2 weighted MR and NAA-MRS images. One day after 3-NP, PET studies showed decreased glucose utilization as large striatal lesions and MRS showed enhanced succinate and lactate/macromolecules peaks in striatum. At this time no changes were observable in NAA or choline peaks. However, 4 weeks later succinate and lactate/macromolecyle peaks disappeared, indicating that these peaks are related to acute neurotoxicity and reversible processes. At this time, decreased NAA and increased choline peaks were observed and T2 weighted MR image showed similar lesions and enlarged ventricles, observed by PET study of glucose utilization. Decreased NAA was also observed as a lesion in NAA-MRS image. This animal had a motor score of 5.

damage and a loss of neurons. These data represent animals with motor score = 4.

Discussion

3-Nitropropionic acid is an irreversible inhibitor of succinate dehydrogenase thereby resulting in cellular ATP depletion and an impairment of energy metabolism (Beal et al. 1993; Guyot et al. 1997; Storgaard et al. 2000; Garcia et al. 2002). 3-NP can induce time-dependent two-way biological processes (Lee et al. 2000; Dautry et al. 2000). Mapping these different components may provide a means to examine the overall regulatory process involved in neurotoxicity. Newly developed high resolution in vivo imaging techniques enable one to investigate multimodality processes simultaneously in the natural biological environment.

Longitudinal imaging studies in the same subjects allowed us to correlate parameters of in vivo physiological functions

and the progression of deficits measured by behavioral or weight changes. Basic research in neuroscience typically relies on in vitro experiments. The limitation of in vitro studies is that they provide information at only the end point when biological interactions created by surrounding tissues and elements are no longer present. In vitro studies provide, however, brief analyses of the isolated biological processes with large amounts of data and high statistical accuracy (Fink et al. 1996).

We divided animals into two groups depending on their behavioral responses, weight loss and changes in glucose utilization resulted of 3-NP toxicity. The animals with the strongest response to 3-NP (behavioral score between 2 and 6) lost about 24% of their weight and the weight loss extended 4 days after the cessation of neurotoxicity. The maximum weight loss in the other group was 12%, and the weight loss stopped the day after the cessation of 3-NP administrations. The observations on motor activity were scored according to the method developed by Guyot et al. (1997) and Ouary et al. (2000) and the observations were similar to those published by Borlongan et al. (1997) and Guyot et al. (1997).

We and others (Guyot et al. 1997; Brouillet et al. 1998; Ouary et al. 2000; El Massioui et al. 2001) have observed significant inter-animal variation in 3-NP-induced changes in motor activity (Borlongan et al. 1997; Guyot et al. 1997), energy metabolism, as well as in the severity of lesions (Beal 1992, 1998; Beal et al. 1993).

A recent study by Guo et al. (2000) showed that dietary restriction could inhibit the effect of 3-NP neurotoxicity. However, a low glucose level alone, which could inhibit 3-NP neurotoxicity, is not enough to explain the inter-animal variation observed in these studies. During 3-NP administration, our animals were housed separately in metabolic cages, fed in the same way and fasted from the night till the following morning for imaging studies of glucose metabolism, which were conducted 2 h before 3-NP administration. Every other 3-NP administration was done in a fasted condition, whereas the 3-NP administration in the evening was done after feeding. This should minimize the possible inter-animal difference induced by dietary patterns. It has been also proposed that strain-dependent genetic aspects might be part of these inter-animal variations of 3-NP-induced neurotoxicity (Ouary et al. 2000). Blum et al. (2001) reported that 3-NP-induced effects are highly variable in the Spraque Dawley rat strain, but continuous subcutaneous administration of 3-NP produces in the Lewis rat strain homogeneous clinical impairment and highly reproducible striatal lesions. Interestingly, rotenone toxicity shows similar inter-animal variation between strains (Betarbet et al. 2000).

Based on in vivo imaging studies, we propose that the variation of 3-NP-induced pathophysiological changes might depend on the metabolic status of the mitochondrion and the tolerance level of the neuron for neurotoxicity. The rats that did not develop any behavioral symptoms or striatal lesions

may have a high tolerance level for 3-NP neurotoxicity. Interestingly, these animals developed enhanced cortical glucose utilization as an early response to 3-NP and this change was reversible.

In vitro studies have demonstrated that 3-NP-induced cell killing may have two different mechanisms: toxicity-induced necrosis and apoptosis (Pang and Geddes 1997). The relationship of these two mechanisms is dependent on the level of toxicity and ATP depletion (Pang and Geddes 1997). These biological degenerative processes are different: necrosis is characterized as the rapid swelling of cells and cell lyses (Wyllie *et al.* 1980; Cepeda *et al.* 1998), whereas in apoptosis, cells are shrunken and cytoplasm and nucleus are fragmented in a slow long-lasting process requiring ATP (Wyllie *et al.* 1984; Kim and Chan 2001). In addition to intracellular energy metabolism, 3-NP-induced neurotoxicity is also dependent on glutamate (Fink *et al.* 1996) and dopamine concentration (Cepeda *et al.* 1998; Reynolds *et al.* 1998).

Our studies show that 3-NP launched development of neurotoxicity is a rapid process and happens in hours. It is possible to record this in real time with MRS of neurochemicals (Fig. 7) and PET imaging studies of glucose utilization (Fig. 5). We observed a $31 \pm 9\%$/min increase rate of lactate/macromolecule level during 150 min follow-up time 2 h after injection of the first dose of 3-NP. Similarly we observed a $5.3 \pm 0.5\%$/min increase rate in succinate level. Thus our results agree with the data reported by Lee *et al.* (2000) that succinate was rapidly observable in MRS, minutes after the injection of 3-NP. In addition, the early increases of succinate and lactate/macromolecule levels were indicative for the development of large striatal lesions. On the third day of 3-NP injections a significant decrease in striatal glucose utilization was observable with similar decrease in cortical areas. Already in the first day after 3-NP administration it was possible to separate animals that developed lesions based on changes in glucose utilization. The animals that develop lesions had decreased levels of glucose utilization in striatum (9.8%) and cortex (6.7%), and the animals that did not develop lesions had enhanced cortical values with no change in striatal values. After this period of neurotoxicity-induced necrosis and fast cell killing, we observed a period of partial recovery followed by slowly progressive degeneration detected by decreases in glucose utilization and NAA and increases of choline.

Based on our results, we hypothesize that in addition to rapidly induced necrosis, 3-NP may have induced a slower form of cell death in less severely affected cells. These cells start to degenerate gradually and the cell death may be caused by apoptotic processes over a long period of time. This slow progression may be more important in studying HD-type neurodegeneration. Vis *et al.* (1999) published that a mild response to 3-NP most closely resembles the characteristics of HD neuropathology and similar observations were initially made by Beal *et al.*

(1993). The striatum is the most vulnerable brain region to systemic intoxication of 3-NP (Brouillet *et al.* 1998). This may be due to the cumulative impairment in energy metabolism caused partially by 3-NP and dopamine toxicity (Reynolds *et al.* 1998; Johnson *et al.* 2000). However, because of the limited number of experimental animals, we cannot conclude from the animal survival based on the behavioral score or severity of the lesion. Daily injections and imaging studies with anesthesia are stressful for the animals and may cause unexpected fatal recovery from the anesthesia.

MRS studies of striatal neurochemicals correlate well with those of glucose utilization. MRS studies showed reversible changes in succinate and lactate/macromolecules in affected animals and progressively increasing choline and decreasing NAA indicating progressive degeneration. These animals developed large lesions and progressively decreasing glucose utilization. The animals that did not develop lesions did not show succinate or lactate peaks.

To enhance the accuracy in the data analyses, the regions of interest were drawn based on the anatomical MR images overlaid with PET images, and the same areas of interest were used in longitudinal studies to partially eliminate the effects of partial volume. In addition, the size of the selected regions of interest was larger than 2.3 mm, which significantly minimizes partial volume effects, since the size of the object should be at least two times the resolution element (Brownell *et al.* 1991), which in our instrument is 1.16 mm.

These multimodality longitudinal imaging techniques provide a powerful tool to investigate the progression of pathophysiological processes and assess therapeutic approaches in small animal models.

Acknowledgements

References

Albin L. and Greenamyre J. T. (1992) Alternative excitotoxic hypothesis. *Neurology* **42**, 733–738.

Alston T. A., Mela L. and Bright H. J. (1977) 3-Nitropropionate, the toxic substance of Indiofera, is a suicide inactivator of succinate dehydrogenase. *Proc. Natl Acad. Sci. USA* **74**, 3767–3771.

Antonini A., Kazumata K., Feigin A., Mandel F., Dhawan V., Margouleff C. and Eidelberg D. (1998) Differential diagnosis of parkinsonism with [18F]fluorodeoxyglucose and PET. *Mov. Disord.* **13**, 268–274.

Beal M. F. (1992) Does impairment of energy metabolism result in exitotoxic neural death in neurodegenerative illness. *Ann. Neurol.* **31**, 119–130.

Beal M. F. (1998) Mitochondrial dysfunction in neurodegenerative diseases. *Biochim. Biophys. Acta* **1366**, 211–223.

Beal M. F., Brouillet E., Jenkins B. G., Ferrante R. J., Kowall N. W., Miller J. M., Storey E., Srivastava R., Rosen B. R. and Hyman B. T. (1993) Neurochemical and histologic characterization of striatal excitotoxic lesions produced by the mitochondrial toxin 3-nitropropionic acid. *J. Neurochem.* **13**, 4181–4192.

Betarbet R., Sherer T. B., MacKenzie G., Garcia-Osuna M., Panov A. V. and Greenamyre J. T. (2000) Chronic systemic pesticide exposure reproduces features of Parkinson's disease. *Nat. Neurosci.* **3**, 1301–1306.

Blum D., Gall D., Cuvelier L. and Schiffmann S. N. (2001) Topological analysis of striatal lesions induced by 3-nitropropionic acid in the Lewis rat. *Neuroreport* **12**, 1769–1772.

Borlongan C., Koutouzis T. K., Freeman T. B., Hauser R. A., Cahill D. W. and Sanberg P. R. (1997) Hyperactivity and hypoactivity in a rat model of Huntington's disease: the systemic 3-nitropropionic acid model. *Brain Res. Protoc.* **1**, 253–257.

Brennan W. A. J., Bird E. D. and Aprille J. R. (1985) Regional mitochondrial respiratory activity in Huntington's disease brain. *J. Neurochem.* **44**, 1948–1950.

Brouillet E., Guyot M. C., Mittoux V., Altaire S., Conde F., Palfi S. and Hantraye P. (1998) Partial inhibition of brain succinate dehydrogenase by 3-nitropropionic acid is sufficient to initiate striatal degeneration in rat. *J. Neurochem.* **70**, 794–805.

Brownell A.-L., Kano M., McKinstry R. C., Moskowitz M. A., Rosen B. R. and Brownell G. L. (1991) PET and MR studies of experimental focal stroke. *J. Comput. Assist. Tomogr.* **15**, 376–380.

Cepeda C., Colwell C. S., Itri J. N., Gruen E. and Levine M. S. (1998) Dopaminergic modulation of early signs of excitotoxicity in visualized rat neostriatal neurons. *Eur. J. Neurosci.* **10**, 4391–4397.

Correia J., Burnham C., Kaufman D. and Fischman A. (1999) Development of a small animal PET imaging device with resolution approaching 1mm. *IEEE Trans. Nucl. Sci.* **46**, 631–635.

Dautry C., Vaufrey F., Brouillet E., Bizat N., Henry P. G., Conde F., Bloch G. and Hantraye P. (2000) Early *N*-acetylaspartate depletion is a marker of neuronal dysfunction in rats and primates chronically treated with the mitochondrial toxin 3-nitropropionic acid. *J. Cereb. Blood Flow Metab.* **20**, 789–799.

Dethy S., van Blercom N., Damhaut P., Wikler D., Hildebrand J. and Goldman S. (1998) Asymmetry of basal ganglia glucose metabolism and dopa responsiveness in parkinsonism. *Mov. Disord.* **13**, 275–280.

Di Chiro G. (1987) Positron emission tomography using [18F]fluorodeoxyglucose in brain tumors. A powerful diagnostic and prognostic tool. *Invest. Radiol.* **22**, 360–371.

Eberling J., Richardson B. C., Reed B. R., Wolfe N. and Jagust W. J. (1994) Cortical glucose metabolism in Parkinson's disease without dementia. *Neurobiol. Aging* **15**, 329–335.

Eidelberg D., Moeller J. R., Ishikawa T. *et al.* (1996) Regional metabolic correlates of surgical outcome following unilateral pallidotomy for Parkinson's disease. *Ann. Neurol.* **39**, 452–459.

El Massioui N., Ouary S., Cheruel F., Hantraye P. and Brouillet E. (2001) Perseverative behavior underlying attentional set-shifting deficit in rats chronically treated with the neurotoxin 3-nitropropionic acid. *Exp. Neurol.* **172**, 172–181.

Fink S. L., Ho D. Y. and Sapolsky R. M. (1996) Energy and glutamate dependency of 3-nitropropionic acid neurotoxicity in culture. *Exp. Neurol.* **138**, 298–304.

Foster D. M. (1994) SAAM II: simulation, analysis and modeling software. *BMES Bull.* **18**, 19–21.

Garcia M., Vanhoutte P., Pages C., Besson M. J., Brouillet E. and Caboche J. (2002) The mitochondrial toxin 3-nitropropionic acid induces striatal neurodegeneration via a c-Jun N-terminal kinase/c-Jun module. *J. Neurosci.* **22**, 2174–2184.

Guo Z., Ersoz A., Butterfield D. A. and Mattson M. P. (2000) Beneficial effects of dietary restriction on cerebral cortical synaptic terminals: preservation of glucose and glutamate transport and mitochondrial function after exposure to amyloid beta-peptide, iron, and 3-nitropropionic acid. *J. Neurochem.* **75**, 314–320.

Guyot M.-C., Hantraye P., Dolan R., Palfi S., Maziere M. and Brouillet E. (1997) Quantifiable bradykinesia, gait abnormalities and Huntington's disease-like striatal lesions in rats chronically treated with 3-nitropropionic acid. *Neuroscience* **79**, 45–56.

Higashi K., Ueda Y., Yagishita M., Arisaka Y., Sakurai A., Ogushi M., Seki H., Nambu Y., Tonami H. and Yamamoto I. (2000) FDG PET measurement of the proliferative potential of non-small cell lung cancer. *J. Nucl. Med.* **41**, 85–92.

Huntington's Disease Collaborative Group (1993) A novel gene containing a trinucleotide repeat is expanded and unstable on Huntington's disease chromosomes. *Cell* **72**, 971–983.

Jenkins B. G., Brouillet E., Chen Y. C., Storey E., Schultz J. B., Kirschner P., Beal M. F. and Rosen B. R. (1996) Non-invasive neurochemical analysis of focal excitotoxic lesions in models of neurodegenerative illness using spectroscopic imaging. *J. Cereb. Blood Flow Metab.* **16**, 450–461.

Johnson J., Robinson B. L., Ali S. F. and Binienda Z. (2000) Dopamine toxicity following long term exposure to low doses of 3-nitropropionic acid (3-NP) in rats. *Toxicol. Lett.* **116**, 113–118.

Kim G. W. and Chan P. H. (2001) Oxidative stress and neuronal DNA fragmentation mediate age-dependent vulnerability to the mitochondrial toxin, 3-nitropropionic acid, in the mouse striatum. *Neurobiol. Dis.* **8** (1 Part B), 114–126.

Lee W.-T., Lee C.-S., Pan Y.-L. and Chang C. (2000) Temporal changes of cerebral metabolites and striatal lesions in acute 3-nitropropionic acid intoxication in the rat. *Magn. Reson. Med.* **44**, 29–34.

Ludolph A. C., He F., Spencer P. S., Hammerstad J. and Sabri M. (1991) 3-nitropropionic acid – Exogenous animal neurotoxin and possible human striatal toxin. *Can. J. Neurol. Sci.* **18**, 492–498.

Ouary S., Bizat N., Altairac S., Menetrat H., Mittoux V., Conde F., Hantraye P. and Brouillet E. (2000) Major strain differences in response to chronic systemic administration of the mitochondrial toxin 3-nitropropionic acid in rats: implications for neuroprotection studies. *Neuroscience* **97**, 521–530.

Palombo E., Porrino L. J., Bankiewicz K. S., Crane A. M., Sokoloff L. and Kopin I. J. (1990) Local cerebral glucose utilization in monkeys with hemiparkinsonism induced by intracarotid infusion of the neurotoxin MPTP. *J. Neurosci.* **10**, 860–869.

Pang Z. and Geddes J. W. (1997) Mechanisms of cell death induced by the mitochondrial toxin 3-nitropropionic acid: acute excitotoxic necrosis and delayed apoptosis. *J. Neurosci.* **17**, 3064–3073.

Phelps M. E., Huang S. C., Hoffman E. J., Selin C., Sokoloff L. and Kuhl D. (1979) Tomographic measurement of local cerebral glucose metabolic rate in humans with (F-18)2-fluoro-2-deoxy-D-glucose: Validation of method. *Ann. Neurol.* **6**, 371–388.

Reynolds D. S., Carter R. J. and Morton J. (1998) Dopamine modulates the susceptibility of striatal neurons to 3-nitropropionic acid in the rat model of Huntington's disease. *J. Neurosci.* **18**, 10116–10127.

Sokoloff L., Reivich M., Kennedy C., Des Rosiers M. H., Patlak C. S., Pettigrew K. D., Sakurada D. and Shinohara M. (1977) The (C-14) deoxy glucose method for the measurement of local cerebral glucose utilization: Theory, procedure, the normal values in the conscious and anesthetized albino rat. *J. Neurochem.* **28**, 897–916.

Storgaard J., Kornblit B. T., Zimmer J., Bert J. and Gramsbergen P. (2000) 3-nitropropionic acid in organotypic striatal and corticostriatal slice cultures is dependent on glucose and glutamate. *Exp. Neurol.* **164**, 227–235.

Vis J. C., Verbeek M. M., De Waal R. M., Ten Donkelaar H. J. and Kremer H. P. (1999) 3-Nitropropionic acid induces a spectrum of

Huntington's disease-like neuropathology in rat striatum. *Neuropathol. Appl. Neurobiol.* **25**, 513–521.

Wyllie A. H., Kerr J. F. and Currie A. R. (1980) Cell death: the significance of apoptosis. *Int. Rev. Cytol.* **68**, 251–306.

Wyllie A. H., Morris R. G., Smith A. L. and Dunlop D. (1984) Chromatin cleavage in apoptosis: association with condensed chromatin morphology and dependence on macromolecular synthesis. *J. Pathol.* **142**, 67–77.

Neurotoxicity-Induced Changes in Striatal Dopamine Receptor Function

ANNA-LIISA BROWNELL, IRIS Y. CHEN, XUKUI WANG, MEIXIANG YU, AND BRUCE G. JENKINS

Department of Radiology, Massachusetts General Hospital, Boston, Massachusetts 02114, USA

KEYWORDS: dopamine receptor; dopamine transporter; striatum

Impairment of dopaminergic neurotransmission can be primary, as in Parkinson's disease or secondary, as in Huntington's disease (HD). The secondary dopamine dysfunction is related to the progressive loss of the striatal neurons bearing the postsynaptic dopamine D1 and D2 receptors. PET studies have shown a significant decrease, at an annual rate of 2–6.5%[2], in striatal glucose metabolism[1] and in dopamine D1 and D2 receptor binding in both asymptomatic and symptomatic HD patients.

Huntington's disease can be modeled by 3-nitropropionic acid (3-NP), which is an inhibitor of succinate dehydrogenase.[3] It causes mitochondrial inhibition and striatal degeneration. We used *in vivo* PET studies to investigate 3-NP–induced acute and prolonged neurotoxic effects on striatal dopamine receptors and transporters in a rat model. 3-NP was administered twice a day at a dose of 10 mg/kg i.p. to eight rats (male Sprague-Dawley rats from Charles River Laboratories, average weight 300 g) until symptomatic gait was observed or for a maximum of 5 days. Imaging studies of dopamine D1 and D2 receptors and transporters were conducted before 3-NP administration and 2 and 7 days and 4 and 16 weeks after 3-NP administration. To validate the striatal deficit, an additional PET study of glucose metabolism was done two days after the cessation of 3-NP using ^{18}F-2-fluorodeoxy-D-glucose (^{18}F-FDG). Studies of dopamine D1 receptors were done using ^{11}C-SCH (Schoering 23660) as a tracer. Dopamine D2 receptors were imaged by ^{11}C-raclopride, and dopamine transporters using 2β-carbomethoxy-3β-4-fluorophenyl tropane (^{11}C-CFT). All the PET imaging studies were conducted using an in-house built tomographic instrument.[4]

FIGURE 1 shows PET studies conducted 2 days after 3-NP administration. The glucose study revealed large striatal lesions. At that time a moderate decrease of dopamine D1 and D2 receptor binding and an increase in dopamine transporter binding were observed. After that, progressive decrease was observed in pre and post-synaptic dopamine receptor function (TABLE 1, FIG. 1).

Address for correspondence: Anna-Liisa Brownell, Department of Radiology, Massachusetts General Hospital, 55 Fruit St., Boston, MA 02114.
abrownell@partners.org

TABLE 1. 3-NP-induced degeneration of the binding of striatal dopamine D1 and D2 receptors and transporters

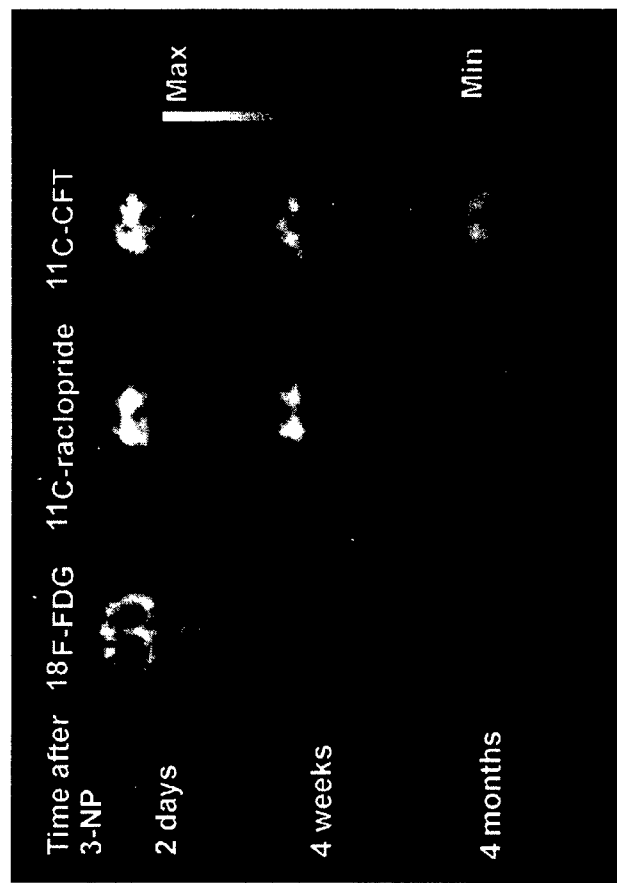| Time after 3-NP	Percent change in the binding of dopamine		
	D1 receptors	D2 receptors	Transporters
2 days	-4 ± 2	-5 ± 2	$+6 \pm 3$
4 weeks	-24 ± 8	-23 ± 7	-10 ± 3
4 months	-36 ± 9	-33 ± 8	-12 ± 4

FIGURE 1. Longitudinal follow-up studies of dopamine D2 receptors (^{11}C-raclopride) and dopamine transporters (^{11}C-CFT) after 3-NP toxicity. Coronal slices show the binding distribution at the midstriatal level. Study of glucose utilization with ^{18}F-FDG shows large striatal lesions 2 days after 3-NP.

Even though HD is associated mainly with the impairment of postsynaptic dopamine receptors as a result of neural loss,[1,2] dopamine transporter binding might have a significant role in predicting the time course of dopaminergic degeneration. We found temporal variation in dopamine transporter binding in the 3-NP rat model. A similar observation has been published in a quinolinic acid rat model.[5] The reports of dopamine transporter function in HD patients include increased, unchanged, or decreased dopamine transporter binding.[6,7] Altogether, these observations might present degeneration at different time points and might well support our observation of the transient mechanism.

ACKNOWLEDGMENT

REFERENCES

1. ANDREWS, T.C., *et al.* 1998. Advances in the understanding of early Huntington's disease using the functional imaging techniques of PET and SPECT. Mol. Med. Today **4**(12): 532–539.

2. ANDREWS, T.C., *et al.* 1999. Huntington's disease progression, PET and clinical observations. Brain **122**(Pt. 12): 2353–2363.

3. ALSTON, T.A., *et al.* 1977. 3-Nitropropionate, the toxic substance of Indigofera, is a suicide inactivator of succinate dehydrogenase. Proc. Natl. Acad. Sci. USA **74:** 3767–3771.

4. BROWNELL, G.L., *et al.* 1985. High resolution tomograph using analog coding. *In* The Metabolism of the Human Brain. Studies with Positron Emssion Tomography. T. Greitz *et al.*, Eds.: 13–19. Raven Press. New York.

5. ARAUJO, M.D. *et al.* 2000. Deficits in striatal dopamine D2 receptors and energy metabolism detected by in vivo mirco PET imaging in a rat model of Huntington's disease. Exp. Neurol. **166:** 287–297.

6. SUZUKI, M. *et al.* 2001. Vesicular neurotransmitter transporters in Huntington's disease: initial observations and comparison with traditional synaptic markers. Synapse **41**(4): 329–336.

7. GINOVART, N. *et al.* 1997. PET study of pre- and post-synaptic dopaminergic markers for neurodegenerative process in Huntington's disease. Brain **120:** 503–514.